Dissertation

System Level Modeling and Optimization of the LTE Downlink

ausgeführt zum Zwecke der Erlangung des akademischen Grades
eines Doktors der technischen Wissenschaften

eingereicht an der Technischen Universität Wien
Fakultät für Elektrotechnik und Informationstechnik

von

Josep Colom Ikuno

geboren am 27. Februar 1984 in Barcelona
Matrikelnummer: 0627675

Wien, im März 2012

Begutachter:

Univ. Prof. Dr.-Ing. Markus Rupp
Institut of Telecommunications
Technische Universität Wien
Österreich

Univ. Prof. Dr.-Ing. Thomas Kürner
Institute for Communications Technology
Technische Universität Braunschweig
Deutschland

I hereby certify that the work reported in this thesis is my own,
and the work done by other authors is appropriately cited.

Josep Colom Ikuno
Vienna, March 1, 2013

Abstract

This thesis presents the design and application of a Link-to-System (L2S) model capable of predicting the downlink throughput performance of cellular mobile networks based on the 3GPP Long Term Evolution (LTE) standard. The aim of a L2S model is to accurately abstract the physical layer at a fraction of the complexity of detailed link level simulations. Thus, it dramatically reduces the necessary simulation run time and by extension enables the simulation of much more complex scenarios.

The thesis is divided in four main parts. First, the basics of the LTE standard are presented, with the link abstraction model being presented afterwards. Extensions for the L2S model for the cases of Hybrid Automatic Repeat reQuest (HARQ) and imperfect channel state information are presented in the third section. In the last chapter, the performance of the application of Fractional Frequency Reuse (FFR) to LTE is evaluated by means of the developed model.

The presented LTE link abstraction model employs a zero-forcing receiver and is based on the calculation of the post-equalization Signal to Interference and Noise Ratio (SINR), which for the Closed Loop Spatial Multiplexing (CLSM) MIMO transmit mode employs a high-Signal to Noise Ratio (SNR) precoder approximation. The designed model is capable of accurately predicting the throughput performance of the following LTE-defined transmit modes and antenna configurations, as validated against link level simulations: Single transmit antenna with MRC combining; 2×2 Transmit Diversity (TxD); 2×2, 4×2, and 4×4 Open Loop Spatial Multiplexing (OLSM); and 2×2, 4×2, and 4×4 CLSM.

The results presented in this thesis have been obtained by the MATLAB implementation of the L2S model, which is released including its source code as the Vienna LTE System Level Simulator. Reproducibility scripts for each of the previous works on which this thesis is based are also available for download, which enables the presented results to be independently replicated. As of March 2013, the simulator has already been downloaded more than 22 000 times and is being used both by universities and industry.

Kurzfassung

Die vorliegende Arbeit präsentiert den Entwurf und die Anwendung eines Link-zu-System Modells (L2S), das es erlaubt, die Durchsatzleistung in der Abwärtsstrecke von zellularen Funknetzen basierend auf den 3GPP Standards vorauszusagen. Ziel des L2S Modells ist es die physikalische Übertragungsebene mit geringerer Komplexität als im Link-Level Fall genauestens zu abstrahieren, somit also die Simulationszeiten dramatisch zu reduzieren. Die Arbeit ist in vier Teile gegliedert. Zunächst werden die benötigten Grundlagen des Long Term Evolution (LTE) Standards vorgestellt, gefolgt vom Link-Abstaktionsmodell. Erweiterungen für das L2S Modell für Hybrid Automatic Repeat reQuest (HARQ) und ungenauer Kanalinformation werden im dritten Teil erläutert. Im letzten Kapitel wird das Leistungsvermögen bei Fractional Frequency Reuse (FFR) mithilfe des vorgeschlagenen Modells ermittelt.

Das vorgeschlagene Link-Abstraktionsmodell verwendet einen Zero-Forcing Empfänger und basiert auf der Berechnung des Signal zu Interferenz- und Rauschverhaltens (SINR) hinter dem Entzerrer. Im Falle von Closed Loop Spatial Multiplexing (CLSM) Multiple-Input Multiple-Output (MIMO) Vorkodierung wird ein hohes SNR angenommen. Die Anwendung des präsentierten Modells erlaubt die Simulation von Szenarien, die wesentlich komplexer sind, als jene die durch Link-Level Modelle berechenbar sind und dies zu einem Bruchteil der Komplexität. Das entworfene Modell kann die Duchsatzleistung der folgenden LTE Übertragungsmodi und Antennenkonfigurationen exakt schätzen und wurde gegenüber einer Link-Level Smulation validiert: Single Transmit Antenne mit MRC Empfänger, 2×2 Transmit Diversität, 2×2,4×2 und 4×4 Open Loop Spatial Multiplexing (OLSM), sowie 2×2, 4×2 und 4×4 CLSM.

Die MATLAB Implementierung des präsentierten Modells wurde in der vorliegenden Arbeit durchgängig verwendet und wurde als Vienna LTE System Level Simulator mit dem gesamten Code freigegeben, um vollständige Reproduzierbarkeit zu gewährleisten. Bis März 2013 wurde der Simulator mehr als 22 000 mal heruntergeladen und wird sowohl von Universitäten als auch Industrie verwendet.

Acknowledgments

This thesis would not have been possible, would Prof. Markus Rupp not have given me the chance to do a PhD at the Vienna University of Technology, and of course without his continuous support. For this, I would like him to be the first one to whom I extend my gratitude.

I would like to thank many for their direct contribution to the thesis as well as those who influenced me at a personal level. Those two are one, as during the course of my PhD much has changed, and this thesis reflects also this evolution.

Thanks for introducing me to LTE goes to Christian Mehlfürer and Martin Wrulich, who started the LTE simulator project and with it, the so-called LTE group. Thanks to Michal Šimko, Qi Wang and Sebastian Caban, with whom I had the pleasure to share office space in the MIMO lab during most of my PhD. Not only from what I learned from you but also for making the office a place I was looking forward to go every day. Thanks also to Stefan Schwarz, Martin Taranetz, and Philipp Svoboda. I had the tremendous luck to be able to learn a lot from you. The more I learned, the better I knew that I do not know much. That enough is a reason to continue moving forward.

I would also like to thank the members of the (by some people) so-called "spanish mafia". Specially Javier Moreno, who also very well understands the sometimes long days needed during a PhD, as well as the need for some beers after them, and also for support during some bad times. Also, without Raúl Ramos and Thomas Herbst, my life in Vienna would not have been as enjoyable and fun as it has been.

Although I left my home city of Barcelona quite some years ago, I would like to thank David Reynés, Daniel Belascoain, Joan Amell, and Davi Ariño for reaffirming through their actions my conviction that if you are motivated, persevere, and have talent, you will achieve your objectives in life, whichever those are.

I would also want to extend my gratitude to Prof. Thomas Kürner, from the TU Braunschweig for accepting my invitation to be my second examiner.

Thank you, Katharina Meidinger, for having given me the best moments in the last two years. Even when you are angry (most of the times, it was very probably me who made you angry, though), you still put a smile in my face :)

Finally, I would like to thank my parents, Hifuya Ikuno and Juan Colom, without whose support over all of these years I would not be where I am now.

Contents

1. Motivation and Scope of Work

Internet traffic has, since 1997, been more than doubling yearly, with an estimated 1.3 exabyte[1]/month of Internet traffic as of Dec. 2012 [1]. As users increasingly turn to mobile broadband, wireless cellular networks have been steadily evolving from being voice-traffic-driven to the actual situation, where mobile traffic represents more than four times that of voice traffic, as seen in Figure 1.1 (left). Although not growing at the same pace as overall traffic, mobile traffic is expected to grow tenfold by 2017, compared to 2012 results [2]. Comparing the growth in mobile traffic to the number of reported active sites, shown in Figure 1.1 (right) [3], it is clear that most of the growth has not been achieved by an increased number of sites but by a continuous improvement of the standards in use.

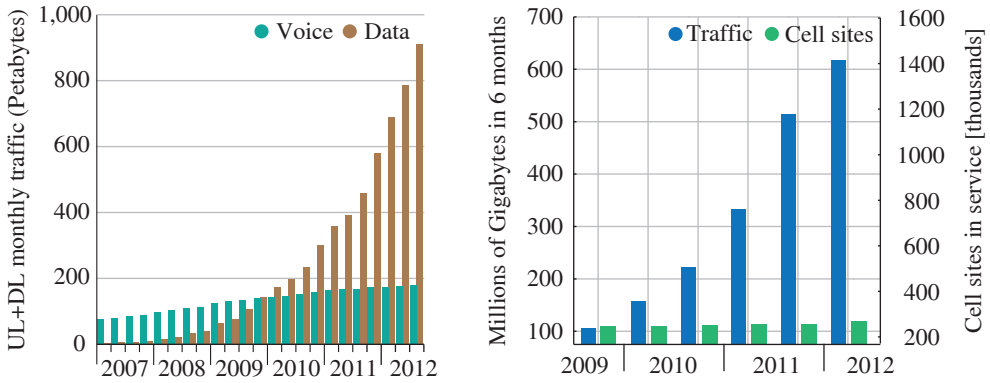

Figure 1.1: Left: Global total traffic in mobile networks, 2007-2012 [2]. Right: Total Wireless data traffic and cell site count, Used with the permission of CTIA-The Wireless Association® [3].

[1] 1 exabyte = 10^{18} byte

As shown in Table 1.1, wireless standards have been steadily evolving, improving the achievable throughput, improving latency [4], and utilizing larger spetra more efficiently with each evolutionary step.

Table 1.1.: Evolution of the maximum download throughput and latency for several 3GPP standards, as defined by their respective maximum mobile equipment capabilities (2000-2010)

		Year	Max. DL speed	Latency	Spectrum
UMTS		2000	0.384 Mbit/s	∼70 ms	5 MHz
HSDPA	Rel'5	2002	14 Mbit/s		
	Rel'7	2007	28 Mbit/s	∼25 ms	
	Rel'8	2009	42.2 Mbit/s		10 MHz
	Rel'9	2010	84.4 Mbit/s		
LTE	Rel'8	2009	300 Mbit/s	15 ms-20 ms	20 MHz

With the addition of Adaptive Modulation and Coding (AMC) and Multiple-Input Multiple-Output (MIMO) spatial multiplexing [5], the last iteration of 3GPP cellular wireless systems, named Long Term Evolution (LTE), is capable of reaching a spectral efficiency of up to 15 bit/s/Hz.

This thesis is motivated by the need of modeling the performance of LTE networks, which feature a new Physical (PHY) layer based on Orthogonal Frequency-Division Multiplexing (OFDM) [6], as opposed to the Wideband Code Division Multiple Access (W-CDMA) PHY of UMTS-based systems [7].

The new PHY offers a higher number of degrees of freedom that can be exploited, which albeit offering a more flexible system, increase the complexity of feedback and resource allocation. Scheduling is performed over time and frequency, and dynamically adjusts the per-user allocated physical resources according to the received channel quality (CQI) and MIMO feedback (PMI and RI). All in order to further increase the spectral efficiency improvements of the PHY with a more efficient exploitation of multi-user gain.

In order to evaluate the opportunities offered by the combination of the LTE PHY and Medium Access Control (MAC) layers, complex scenarios consisting of multiple eNodeBs and users need to be simulated, which unless proper modeling of the PHY layer is applied, is computationally very costly or very inaccurate if over-simplified scenarios are employed.

The main objective of this thesis is to describe a *link abstraction model*, also alternatively referred to as Link-to-System (L2S) model or L2S interface, for LTE Release 8, with particular focus on the MIMO capabilities of the PHY. It aims at accurately modeling link performance without the need to simulate all of the involved PHY

layer procedures, thus significantly decreasing simulation complexity and enabling the simulation of more complex scenarios and the evaluation of Multi-User (MU) gain at the network level.

The proposed model serves as basis for a MATLAB-implemented LTE system level simulation tool [8], openly available for free for academic, non-commercial use, which enables the reproducibility of the results in this thesis, as well as the prior work on which it is based upon.

1.1. Outline

The main sections of this thesis, which span Chapters 2 to 5, comprise a description of the relevant aspects of LTE necessary for L2S modeling, a description and validation of the proposed model, extensions for imperfect channel knowledge and HARQ, and finally an application of the L2S model to evaluate the performance of Fractional Frequency Reuse (FFR) jointly with scheduling in LTE networks.

A short summary of each of the core sections of this thesis, as well as its relation to the publications listed in Section 1.2, can be found in the subsections below.

Chapter 2: 3GPP Long Term Evolution

In the first chapter, heavily based on the contribution in [1], a very brief overview of the reasons behind the creation of the LTE standard is given, as well as an overview of the network structure LTE defines. The bulk of the chapter is devoted to the description of the PHY and MAC layers, with special attention to the following topics, relevant for L2S modeling:

- Structure of the OFDM-based PHY layer.
- Defined MIMO transmit modes, as well as the feedback required for each of them.
- Channel coding and Hybrid Automatic Repeat reQuest (HARQ) procedures.
- Degrees of freedom at the scheduler level to exploit multi-user diversity and adapt to the channel conditions: frequency, time, AMC, as well as spatial multiplexing.

Chapter 3: Physical Layer Modeling and LTE System Level Simulation

In this section, the importance of system level simulations is highlighted, as it allows for simulation of scenarios where rather than that of a single link, the performance of a complex network layout can be evaluated. It begins by, based on the Bit-Interleaved Coded Modulation (BICM) model, modeling a single LTE TX-RX link with the structure presented in Chapter 2. The link model is progressively developed

into a combination of a link quality model and a link performance model, based on the calculation of the post-equalization Signal to Interference and Noise Ratio (SINR) and Additive White Gaussian Noise (AWGN) Block Error Ratio (BLER) curves obtained from link level simulations.

This chapter describes the functional separation of the L2S model into its two components: the link quality and the link performance model, which perform the following functions:

- The link quality model encompasses the calculation of the post-equalization SINR based on a Zero Forcing (ZF) receiver model on a per-subcarrier basis, thus incorporating the OFDM-based PHY and MIMO processing of LTE into its design. It is in this stage of the modeling that a MIMO channel model and the network layout is incorporated, the latter of which based on pathloss maps, space-correlated shadow fading, antenna radiation patterns and the radiated transmit power.
- The link performance model, which takes as input the output of the link quality model, compresses the subcarrier SINRs into a single value by means of Mutual Information Effective SINR Mapping (MIESM), thus quantifying the quality of the OFDM frequency-selective signal with a single AWGN-equivalent SINR value. This allows for the usage of a single set of link-level-obtained performance curves, independent of the channel. The link performance model finally outputs the link throughput and BLER.

To further reduce run time complexity, part of the most computationally-intensive processing necessary during system level simulations can be performed off-line once and then reused in subsequent simulations:

- Link level AWGN BLER curves for each Modulation and Coding Scheme (MCS) need be produced once and are reused at every simulation. As MIESM enables the link performance model to be fading-insensitive, the same BLER curves can employed independently of the channel type.
- As MU-MIMO is not in the scope of this model, it is possible with negligible loss of precision to precalculate the optimum precoder choice (shown in Appendix A) and store it as fading parameters in a pregenerated channel trace. This offloads the computationally-intensive complex-valued matrix multiplications and inversions required by the MIMO processing and SINR calculations and substitutes them with simple scalar products at run-time.
- Network layouts as well as user spatial distributions can be cached and stored, thus reducing the need to re-generate commonly-employed simulation scenarios and enabling the reproduction of specific scenarios in a reproducible manner.

However well-elaborated and sophisticated, any such link abstraction models needs to be compared to link level results, as the validity of performance evaluations

performed via abstraction models is only as accurate as the abstraction model itself is. In the second part of this chapter, the results of the link abstraction model are compared to link level simulations, both at the simplest level (single-cell, single user), as well as in multi-cell setups.

The following scenarios are considered for the link-to-system validation:

- A single-cell, single-user scenario, analogous to link level simulations over a Signal to Noise Ratio (SNR) range validates whether (i) with the only link level input of AWGN BLER curves, the throughput of time-and-frequency selective channels can be accurately modeled, (ii) the accuracy of the MIMO precoder precalculation, and (iii) the accuracy of the system level feedback calculation.
- A multi-user scenario, comparing the multi-user gain observed at link level and at system level.

Additionally, a brief complexity analysis is also provided, comparing the simulation run-time of system level simulations compared to that of link level simulations, thus highlighting the advantages of employing a L2S model for more complex simulation scenarios.

Related work

This chapter represents the basis of the LTE L2S model. Published work on which this chapter is based include [2], where the LTE MIMO link abstraction was presented. The creation of the model would not have been possible without the prior work on LTE link level simulation, which was presented on [3]. A first validation of link-to-system simulation results was first presented on [4], although for this thesis a more complex multi-cell scenario with different penetration losses has been additionally considered. Additionally linked to this chapter are the contents of appendices A, B and D. While the contents of the multi-user gain analysis of the LTE downlink in Appendix D are contained in [5], the contents of appendices A and D are, as of the finishing date of this thesis, not contained in any peer-reviewed publication.

Chapter 4: Extensions to the L2S Model

In addition to the LTE L2S model presented in Chapter 3, this chapter presents further enhancements to the link quality and link performance models that enable the L2S model to take into account imperfect channel knowledge and HARQ combining.

In the first part of the chapter, an extension to the link performance model is introduced. This extended model takes into account the gain introduced by the HARQ MAC layer retransmission scheme of LTE and is based on a separation of the HARQ gain into a coding gain and a repetition gain. A metric based on

Mutual Information (MI) is employed to quantify the amount of information in after N retransmissions, while an effective SINR of the received combined packet is calculated and combined with link-level-generated BLER to curves to calculate the final BLER. Results are shown to be accurate for all of the retransmissions realistically used by the eNodeBs in an LTE deployment.

In the second part of the chapter, an extension to the post-equalization SINR calculation is presented. This extension, based on a Taylor expansion of the post-equalization SINR expression for the ZF receiver, introduces channel estimation errors in the calculation of the SINR and thus, enables the L2S model to add it to network performance evaluations.

Related work

The extension of the link quality model to HARQ was presented in [6], but would not have been possible without the analysis of LTE rate matching procedures necessary for [7]. The extension of the link quality model for imperfect channel state information in this chapter and Appendix C contains the work presented in [8], and employs the modeling of the channel estimation noise developed in [9].

Chapter 5: Performance Evaluation of Fractional Frequency Reuse in LTE

In the last chapter, system level simulations are employed to evaluate the performance of FFR applied to LTE networks. The application of the developed L2S model enables FFR performance to be evaluated in terms of throughput, as opposite to the capacity-based metrics commonly employed in literature. The considered scenario is that of a fully-loaded hexagonal cell setup and a 4×4 Closed Loop Spatial Multiplexing (CLSM) transmission, combined with round robin and proportional fair scheduling.

Initial results showed that the usual mean/peak/edge throughput performance metrics to be insufficient, thus a new metric additionally taking fairness into consideration is also introduced.

After the introduction of a fairness measure, it is shown that, if a suboptimal scheduler such as round robin is employed, throughput and fairness gains can be extracted by means of FFR. However, such gains are shown to disappear if proportional fair scheduling is employed.

Related work

This performance evaluation of FFR applied to LTE is based on the previous work presented on [10], in which the potential of FFR for throughput increase was shown.

The combined throughput-and-fairness metric, as well as the subsequent simulation-based analysis is performed, are contained in [11], where the LTE L2S model is applied to the performance evaluation of FFR.

1.2. List of Related Publications

[1] J. C. Ikuno, **UMTS Long-Term Evolution**. in *Evaluation of HSDPA and LTE: From Testbed Measurements to System Level Performance*, S. Caban, C. Mehlführer, M. Rupp, and M. Wrulich, Eds. John Wiley & Sons, Ltd, 2012.

[2] J. C. Ikuno, M. Wrulich, and M. Rupp, "**System level simulation of LTE networks**," in *71st Vehicular Technology Conference (VTC2010-Spring)*, Taipei, Taiwan, May 2010.

[3] C. Mehlführer, M. Wrulich, J. C. Ikuno, D. Bosanska, and M. Rupp, "**Simulating the Long Term Evolution physical layer**," in *European Signal Processing Conference (EUSIPCO2009)*, Glasgow, Scotland, Aug. 2009.

[4] C. Mehlführer, J. C. Ikuno, M. Šimko, S. Schwarz, M. Wrulich, and M. Rupp, "**The Vienna LTE simulators - enabling reproducibility in wireless communications research**," *EURASIP Journal on Advances in Signal Processing*, 2011.

[5] S. Schwarz, J. Colom Ikuno, M. Šimko, M. Taranetz, Q. Wang, and M. Rupp, "**Pushing the Limits of LTE: A Survey on Research Enhancing the Standard**," *arXiv e-prints*, Dec. 2012.

[6] J. C. Ikuno, C. Mehlführer, and M.Rupp, "**A novel LEP model for OFDM systems with HARQ**," in *IEEE International Conference on Communications (ICC2011)*, Kyoto, Japan, June 2011.

[7] J. C. Ikuno, S. Schwarz, and M. Šimko, "**LTE rate matching performance with code block balancing**," in *17th European Wireless Conference (EW2011)*, Vienna, Austria, Apr. 2011.

[8] J. C. Ikuno, S. Pendl, M. Simko, and M. Rupp, "**Accurate SINR estimation model for system level simulation of LTE networks**," in *IEEE International conference on Communications 2011 (ICC2012)*, Ottawa, Canada, June 2012.

[9] M. Šimko, S. Pendl, S. Schwarz, Q. Wang, J. C. Ikuno, and M. Rupp, "**Optimal pilot symbol power allocation in LTE**," in *IEEE 74th Vehicular Technology Conference (VTC2011-Fall)*, San Francisco, California, Sept. 2011.

[10] M. Taranetz and J. C. Ikuno, "**Capacity density optimization by fractional frequency partitioning**," in *45th Annual Asilomar Conference on Signals, Systems, and Computers (ASILOMAR2011)*, Pacific Grove, California, Nov. 2011.

[11] J. C. Ikuno, M. Taranetz, and M. Rupp, "**A fairness-based performance evaluation of fractional frequency reuse in LTE**," in *17th International ITG Workshop on Smart Antennas (WSA2013)*, Stuttgart, Germany, Mar. 2013.

2. 3GPP Long Term Evolution

In its Release 8, Long Term Evolution (LTE) was standardized by the 3rd Generation Partnership Project (3GPP) as the successor of the Universal Mobile Telecommunications System (UMTS) standard. LTE was designed from the start with the assumption that all of the services would be packet-switched rather than circuit switched, thus continuing the trend set from the evolution of Global System for Mobile communications (GSM), to General Packet Radio Service (GPRS), Enhanced Data Rates for GSM Evolution (EDGE), UMTS, and High-Speed Packet Access (HSPA). During this evolution, it has been seen how the focus has been moving towards providing ubiquitous availability of broadband communications, as well as the classical voice/text communication capabilities. From the early mobile packet services, not only has throughput been dramatically increased, but also latency greatly decreased [4, 9, 10]. Early 2G-based systems such as GPRS were able to offer data transfer rates in the order of 10 kbit/s, while in its latest current iteration, HSPA can theoretically reach peak speeds of 80 Mbit/s by combining multiple 5 MHz carriers and Multiple-Input Multiple-Output (MIMO) techniques [11–13]. The combination of higher throughput requirements, lower latency, as well as affordability, given the needed non-linear evolution between traffic volume and cost [14], contributed to the requirements specified for LTE by 3GPP, which are summarized in the following points [15–17]:

- Increased peak data rates of 100 Mbit/s in the Downlink (DL) and 50 Mbit/s in the Uplink (UL), as well as improvements in cell edge and spectrum efficiency.
- Scalable bandwidth
- Easy interworking with existing 3GPP systems and cost-effective migration to LTE, resulting in a reduced CAPital EXpenditure (CAPEX).
- Simplified network architecture allowing for a lower OPerational EXpenditure

Table 2.1.: 3GPP requirements for E-UTRAN [15].

			Requirements	Configurations
DL	UE throughput	peak data rate	100 Mbit/s	2 TX×2 RX antennas, 20 MHz DL
		5% point of cdf	3x-4x Rel'6 HSDPA	
		avg. throughput	3x-4x Rel'6 HSDPA	
	spectral efficiency		3x-4x Rel'6 HSDPA	
UL	UE throughput	peak data rate	50 Mbit/s	1 TX×2 RX antennas, 20 MHz UL
		5% point of cdf	2x-3x Rel'6 HSDPA	
		avg. throughput	2x-3x Rel'6 HSDPA	
	spectral efficiency		2x-3x Rel'6 HSDPA	
spectrum allocation			1.4, 3, 5, 10, 15, 20 MHz possible	

(OPEX) and support for high user mobility.

Table 2.1 lists the 3GPP requirements for the LTE Radio Access Network (RAN), termed Evolved UMTS Terrestrial Radio Access Network (E-UTRAN). The final capabilities of LTE, however go beyond those of the defined target requirements. For instance, although, the targets for DL and UL peak data rate were set to 100 Mbit/s and 50 Mbit/s respectively [18], LTE users, termed User Equipments (UEs), support up to 300 Mbit/s DL and 75 Mbit/s UL peak data rates.

Diverging from the previous UMTS standard, which is based on Wideband Code Division Multiple Access (W-CDMA), the LTE PHY is based on Orthogonal Frequency-Division Multiple Access (OFDMA) [19] in the DL, and Single-carrier FDMA (SC-FDMA) [20] in the UL [21–24], which both convert the wide-band frequency selective channel into a set of flat fading subchannels by means of a Cyclic Prefix (CP) [25]. The flat fading subchannels have the advantage that even in the case of MIMO transmission, optimum receivers can be implemented with reasonable complexity, as opposed to W-CDMA systems, where time-domain equalization is needed [26]. OFDMA additionally allows for frequency domain scheduling, making it possible to assign PHY resources to users with optimum channel conditions. This offers large potential throughput gains in the DL due to multi-user diversity [27, 28]. LTE also includes an interface for communication between base stations (eNodeBs in LTE nomenclature), named X2-interface, which can be used for interference management and eNodeB coordination, aiming at decreasing inter-cell interference.

Regardless of the network capabilities, the system is nevertheless constrained by the actual capabilities of the receiver mobile equipment. That is, the UE capabilities. LTE defines five UE radio capability categories, to which a given UE has to conform to [29]. These range from a UE not capable of MIMO transmission with a maximum throughput of 10 Mbit/s DL and 5 Mbit/s UL to a 4×4-capable MIMO terminal with

up to 300 Mbit/s DL and 70 Mbit/s UL. Table 2.2 details the maximum throughput for both DL and UL, as well as their MIMO Spatial Multiplexing (SM) capabilities.

Table 2.2.: LTE UE categories [29]. Each UE category constrains the maximum throughput and SM capabilities supported in DL and UL.

		UE Category				
		1	2	3	4	5
DL	peak throughput [Mbit/s]	10.3	51	102	150.8	302.8
	max. number of supported layers for SM	1	2	2	2	4
	max. number of supported streams for SM	1	2	2	2	2
UL	peak throughput [Mbit/s]	5.2	25.5	51	51	75.4
	support for 64-QAM	No	No	No	No	Yes

2.1. Network Architecture

The basic network architecture of LTE remains comprised of three parts: (i) the mobile terminal, termed UE, which is connected, the (ii) E-UTRAN radio access network, and (iii) the core network, termed System Architecture Evolution (SAE), the main component of which is the Evolved Packet Core (EPC). Figure 2.1 depicts both the elements comprising each of the parts from the network and its interconnection to 2G/3G network elements.

In the now-all-IP SAE architecture the core network provides access to external packet networks based on IP and performs a number of functions for idle and active terminals. Connected to the core network, the RAN performs all radio interface-related functions for terminals in active mode [30].

In contrast to prior architectures, the LTE RAN is a meshed network where the functions previously fulfilled by the Radio Network Controller (RNC) in UMTS and/or the Base Station Controller (BSC) in GSM are integrated into the eNodeB. In order to enable a meshed RAN topology, the eNodeBs are now not only hierarchically connected to the core network but are also able to communicate with each other, which makes it potentially possible to employ eNodeB cooperation schemes to increase network performance. eNodeBs implements the following RAN functionalities, which are shown in Figure 2.2:

- All PHY and MAC layer procedures, including link adaptation, Hybrid Automatic Repeat reQuest (HARQ), and cell search.
- Radio Link Control (RLC): Segmentation and Automatic Repeat reQuest (ARQ) control of the radio bearers.

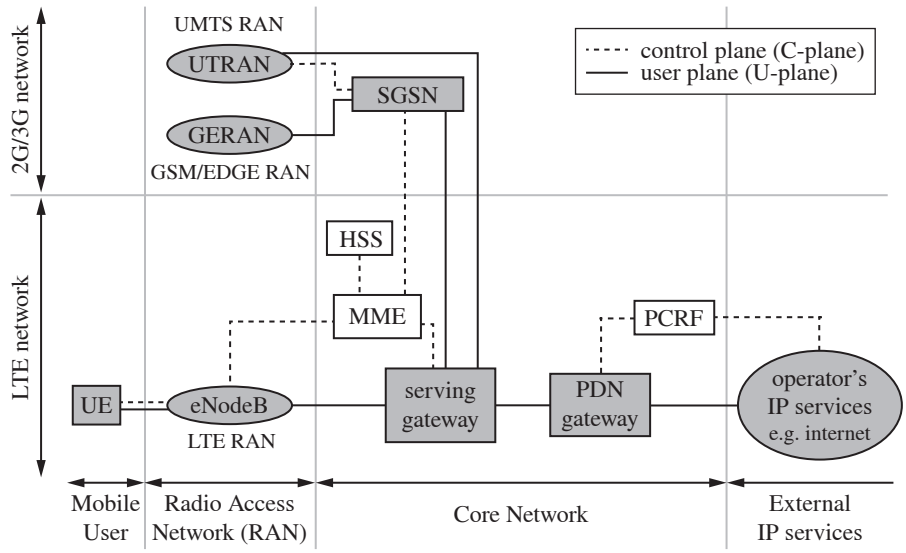

Figure 2.1: Overall LTE architecture [31–33]. The solid lines interconnecting LTE and 2G/3G network elements denote U-Plane traffic, while the dotted lines C-Plane traffic.

- Packet Data Convergence Protocol (PDCP): IP header compression by means of RObust Header Compression (ROHC) [34] and encryption of the user data streams.
- Radio Resource Control (RRC): at the C-Plane level, it controls the handover, manages Quality of Service (QoS), establishes and maintains radio bearers, manages keys (security), and controls/reports UE measurements.
- Radio Resource Management (RRM): ensures that radio resources are assigned efficiently and meeting the QoS constraints imposed by the core network. The RRM layer achieves it by means of controlling radio admission and bearers, connection mobility, and UL/DL scheduling.
- Selection of a Mobility Management Entity (MME) at UE attachment.
- Routing of the U-Plane data towards the Serving Gateway (S-GW).

The SAE core network is responsible of Non-Access Stratum (NAS) procedures [36], which include UE mobility, IP session management, and security to those. Also provided by the SAE are packet routing, and network management. The most important elements of the EPC are the MME, S-GW, and PDN Gateway (P-GW) [32, 37], which perform the following functions:

The MME supports subscriber and session management at the C-Plane level:

- S-GW and P-GW selection, as well as idle state mobility control and roaming.
- Ciphering and integrity protection of NAS signalling.
- Distribution of paging messages to the Evolved Node Bs (eNodeBs).

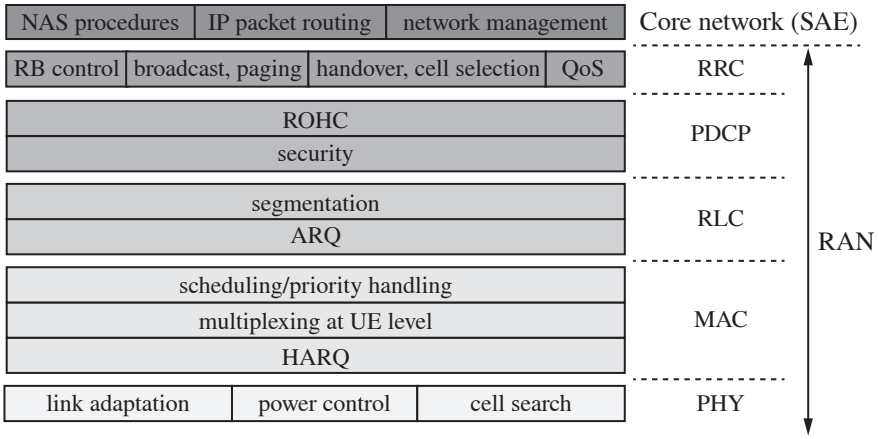

Figure 2.2: Layer structure for LTE [31, 35].

- Signaling between nodes of different core networks for mobility between 3GPP access networks including Serving-General packet radio service Support Node (SGSN) selection for handovers to 2G or 3G 3GPP networks.
- Security control together with the Home Subscriber Server (HSS), which supports the database containing the user subscription information.

The Serving Gateway (S-GW) is the termination point towards the RAN. It supports the termination of U-Plane packets and its switching when UE mobility requires it, as well as packet routing and forwarding. For UTRAN (3G) mobility, the U-Plane connection is done directly with the UMTS RAN, while the signaling goes through the SGSN. For GSM EDGE Radio Access Network (GERAN) (2G) mobility, both C-Plane and U-Plane are routed through the SGSN, as shown in Figure 2.1.

Lastly, the PDN Gateway (P-GW) serves as an anchor point for sessions towards external Packet Data Networks (PDNs). It supports:

- Packet filtering and/or marking and DHCP functionality (IP address allocation).
- Service level charging and rate enforcing, together with the Policy and Charging Rules Function (PCRF).

This functional split of the SAE elements allows for a more specialized implementation of the MME, S-GW, and P-GW. Thus, the MME is optimized for C-Plane processing, while the S-GW is optimized to process high-throughput U-Plane data. The P-GW performs functions analogous to those of an exit edge router in the commonly-used IP DiffServ architecture [38] for the LTE core network.

2.2. LTE Physical Layer

The LTE PHY layer substitutes the Code-Division Multiple Access (CDMA) access technology employed in 3G standards with a new Orthogonal Frequency-Division Multiplexing (OFDM) PHY layer, which implies that the PHY resources no longer span in the code and time domain, but rather the frequency and time domain (in both cases additionally the spatial domain if MIMO is applied).

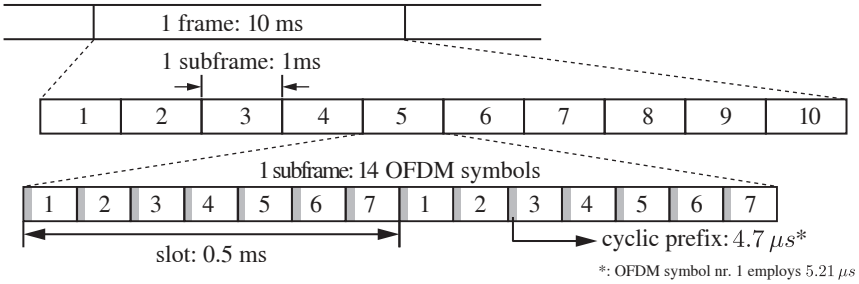

Figure 2.3: LTE frame structure (FDD mode).

In LTE, DL transmissions are organized into radio frames with a duration of 10 ms, both for the Time Division Duplex (TDD) and Frequency Division Duplex (FDD) modes. Focusing just on the FDD case, each radio frame is subdivided into ten subframes of 1 ms each, subsequently divided into two slots and seven OFDM symbols each. In order to avoid inter-symbol interference, a CP is added to the beginning of each symbol, with a length of 5.21 μs for the first symbol or 4.7 μs for the remaining six symbols (Figure 2.3). A longer CP configuration is also standardized, but is not considered in this work [39].

Table 2.3.: Available LTE system bandwidths and available resource blocks [40].

Channel bandwidth (B_{channel}) [MHz]	1.4	3	5	10	15	20
Number of RBs ($N_{\text{RB}}^{\text{DL}}$)	6	15	25	50	75	100
Number of data subcarriers	72	180	300	600	900	1200
Transmission bandwidth (B_{TX}) [MHz]	1.08	2.7	4.5	9	13.5	18
Bandguard size [% of B_{channel}]	23%	10%	10%	10%	10%	10%

In the frequency domain, the available bandwidth is divided into equally-spaced orthogonal subcarriers. The typical subcarrier spacing, which is employed in this thesis, is 15 kHz, although a smaller 7.5 kHz spacing is also possible. Subcarriers are organized in groups of $N_{\text{sc}}^{\text{RB}}$ consecutive subcarriers, which is 12 for the normal-length CP and 24 when employing a 7.5 kHz subcarrier spacing. Each of the subcarrier groups, spanning 180 kHz, is referred to as a Resource Block (RB), as depicted in Figure 2.4. The LTE standard defines a set of possible bandwidths [40], which

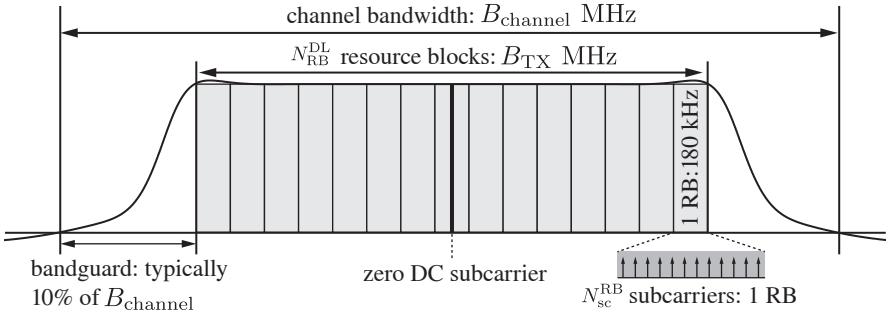

Figure 2.4: LTE frequency spectrum distribution for a channel bandwidth (B_{channel}) of 3 MHz and a 15 kHz subcarrier spacing: $N_{\text{RB}}^{\text{DL}} = 15$ and $N_{\text{sc}}^{\text{RB}} = 12$.

determine the number of RBs, data subcarriers and bandguard size, as listed in Table 2.3.

Combining the time and frequency partitioning, a time-frequency grid such as the one shown in Figure 2.5 is obtained. Each element resulting from this time-frequency separation is termed a Resource Element (RE), and defines the positions in which the transmitted data, be it reference symbols or data/control channels are placed in the DL frame.

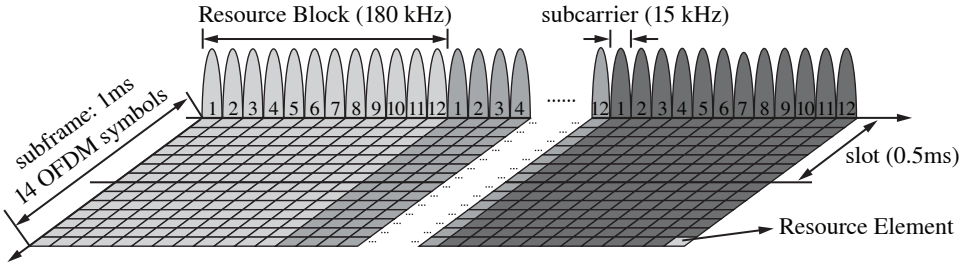

Figure 2.5: LTE time-frequency grid: allocation of the resource elements in an LTE subframe over time (14 OFDM symbols) and frequency ($N_{\text{sc}}^{\text{RB}} \times N_{\text{RB}}^{\text{DL}}$ subcarriers).

2.2.1. MIMO Transmission

MIMO techniques are one of the main enablers to achieve the throughput requirements for E-UTRAN listed in Table 2.1. The LTE standard defines support for one, two, and four transmit antennas. The supported multi-antenna transmit modes employ either a Transmit Diversity (TxD) or SM transmission scheme in order to increase diversity, data rate, or both. These are described in detail for the two transmit antenna case to illustrate the concepts behind them, considering the four transmit antenna case as an extension of this case. SM can be operated in two modes: Open Loop Spatial Multiplexing (OLSM) and Closed Loop Spatial Multiplexing (CLSM). While both require feedback regarding the number of spatial layers employed, in OLSM no precoding matrix feedback is employed (hence the

"open loop" terming), while in CLSM, the optimum precoding matrix information is additionally fed back to the eNodeB by the UE.

2.2.1.1. Transmit Diversity

The TxD mode provides transmit diversity by means of an Alamouti Space-Time Block Code (STBC) [41]. For the two transmit antenna case, the transmit vector $\mathbf{x} = [x_0, x_1]^{\mathrm{T}}$, is mapped to the output from each antenna $\mathbf{y}$, which is sent over two time slots (column-wise), as $\mathbf{y} = \begin{bmatrix} x_0 & -x_1^* \\ x_1 & x_0^* \end{bmatrix}$ [39].

2.2.1.2. Open Loop Spatial Multiplexing

In a SM scheme, the transmit vector $\mathbf{x}$ containing the modulated data symbols is multiplied by a precoding matrix $\mathbf{W}$, generating the output vector $\mathbf{y}$ to be sent over the antennas. Thus, $\mathbf{y} = \mathbf{W}\mathbf{x}$.

In LTE, the length of the vector $\mathbf{x}$ is referred to as the number of layers (denoted as ν), and is the number of symbols simultaneously transmitted over the available N_{T} transmit antennas. Thus, the precoding matrix $\mathbf{W}$ generates ν spatial beams that are sent $\mathbf{x}$ over the N_{T} transmit antennas.

OLSM employs a fixed precoder (or a cyclical set of precoders in the case with four transmit antennas) and allows for the number of layers ν to be configured. To compensate for the suboptimal precoder choice, OLSM additionally applies Cyclic Delay Diversity (CDD) to the transmit symbol vector [42]. CDD shifts the transmit signal in the time direction and transmits these modified signal copies over separate transmit antennas. The time shifts are inserted in cyclically (hence the name), thus not affecting Inter-Symbol Interference (ISI). This results in increasing the number of resolvable channel propagation paths, and thus increased diversity with no additional receiver complexity [43].

For the two transmit antenna case, and at a time instant k, the transmission of a symbol vector $\mathbf{x}_k$ of length ν symbols, can be formulated as

$$\mathbf{y}_k = \mathbf{W}\mathbf{D}_k\mathbf{U}\mathbf{x}_k, \tag{2.1}$$

where $\mathbf{D}_k$ cyclically shifts the delay depending on the time index k, and $\mathbf{W}$, $\mathbf{U}$ and $\mathbf{D}_k$ are defined as [39]:

$$\mathbf{W} = \frac{1}{\sqrt{2}}\begin{bmatrix} 1 & 0 \\ 0 & 1 \end{bmatrix}, \qquad \mathbf{U} = \frac{1}{\sqrt{2}}\begin{bmatrix} 1 & 1 \\ 1 & e^{-\mathrm{i}2\pi/2} \end{bmatrix}, \qquad \mathbf{D}_k = \begin{bmatrix} 1 & 0 \\ 0 & e^{-\mathrm{i}2\pi k/2} \end{bmatrix}. \tag{2.2}$$

Since the CDD matrix cycles with a period of two, $\mathbf{D}_k$ can be expressed as $\mathbf{D}_{k \bmod 2}$ for the two transmit antenna case. For $\nu = 1$, OLSM is not defined.

In the case of four transmit antennas, instead of a fixed $\mathbf{W}$ matrix, a different precoder is applied after ν vectors, as well as $\mathbf{D}_{k \bmod 2}$ instead of $\mathbf{D}_{k \bmod 2}$. Appropriate $\mathbf{U}$, $\mathbf{D}_k$, and $\mathbf{W}$ matrices are defined for $\nu = 3, 4$ in [39].

2.2.1.3. Closed Loop Spatial Multiplexing

Unless the feedback is invalidated by a rapidly changing channel, gains can be obtained in comparison to OLSM by signaling the eNodeB an optimum precoding matrix $\mathbf{W}$ in combination with the number of desired layers ν instead of employing CDD. Thus, expressing the output symbol vector $\mathbf{y}$ as $\mathbf{y} = \mathbf{W}\mathbf{x}$.

In order to simplify signaling, instead of feedbacking the actual optimum precoder matrix [44], a precoder is chosen from a predefined codebook, the index of which is sent to the eNodeB as feedback. For $N_{\mathrm{TX}} = 2$, the LTE codebook is comprised of four ($\nu = 1$) and two ($\nu = 2$) precoders, which are listed in Table 2.6. For four transmit antennas, the codebook spans 15 precoding choices for $\nu \in \{1, 2, 3, 4\}$.

2.2.2. Layer-to-Codeword Mapping

The LTE standard allows for up to two parallel data streams, termed codewords, to be simultaneously transmitted. As seen in Section 2.2.1, up to four symbols can be simultaneously transmitted when using either OLSM or CLSM. While the precoding-related procedures work on a per-layer basis, the channel coding and channel quality reporting procedures work on a per-codeword basis.

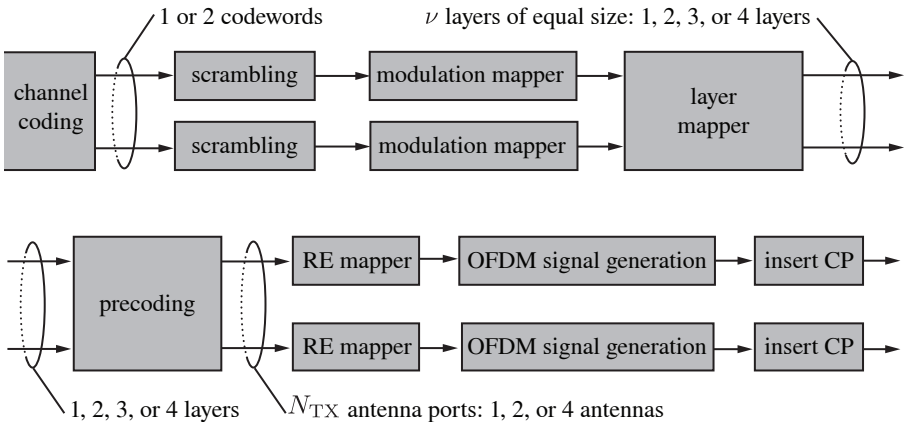

Figure 2.6: Modulation and layer mapping procedures [39]. The one or two codewords output by the channel coding procedures are scrambled, mapped to complex symbols, distributed in ν layers (layer mapping), mapped to N_{TX} transmit antenna ports and converted to the time domain.

As shown in Figure 2.6, the one or two codewords of coded data bits output by the channel coding procedures are mapped to ν spatial layers via a layer mapping and then to the N_{T} transmit antenna ports via the precoding (when applicable) [39].

Table 2.4 describes the LTE codeword-to-layer mapping employed by the OLSM and CLSM modes for the allowed combinations of number of codewords and number of layers ν. No layer mapping is required in non-SM modes.

Table 2.4.: Layer mapping for spatial multiplexing [39]

layers → codewords	codeword-to-layer mapping
1 → 1	codeword 1 → layer 1
2 → 2	codeword 1 → layer 1 codeword 2 → layer 2
2 → 1	codeword 1 → layers 1,2
3 → 2	codeword 1 → layer 1 codeword 2 → layers 2, 3
4 → 2	codeword 1 → layers 1,2 codeword 2 → layer 3, 4

2.2.3. Channel Coding

LTE, as well as HSPA, relies on Adaptive Modulation and Coding (AMC) in order to provide adaptability to the channel conditions. In order to match the radio channel capacity and Block Error Ratio (BLER) requirements for each UE, the eNodeB dynamically adjusts both the applied code rate and modulation.

The LTE channel coding procedures [45, 46] specify a per-user and per-codeword coding and modulation chain, which according to the signaling passed down from the MAC layer (see Section 2.2.4), applies an appropriate coding rate and modulation alphabet to the data bits.

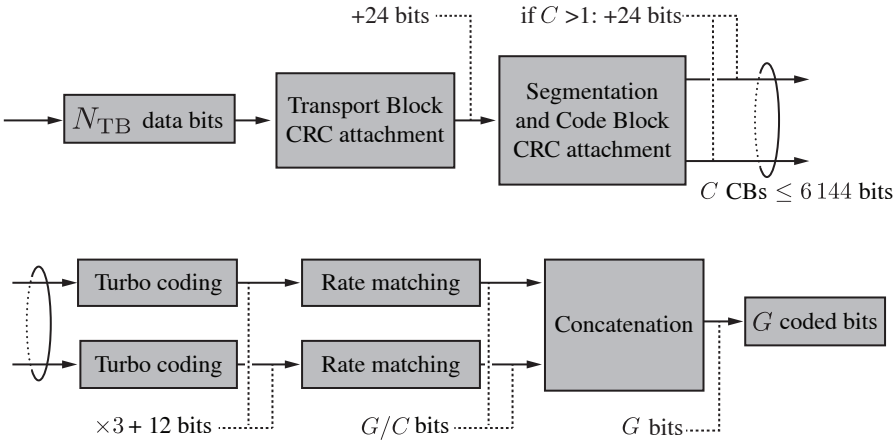

Figure 2.7: LTE channel coding procedures for the DLSCH for one codeword [45]. For the N_{TB} bits, error detection is provided by means of one or more 24-bit CRCs , while error correction is provided by a rate-matched turbo code with variable bit rate.

The channel coding procedures are depicted in Figure 2.7, and describe for each codeword, the encoding of N_{TB} bits into a Transport Block (TB) of size G bits[45]. The channel coding procedures implement error-detecting capabilities by means of one or several 24-bit CRCs and error correction with a turbo code [47]. Since the turbo coder interleaver has a maximum size of $Z = 6\,144$ bits, the N_{TB} bits are segmented into C Code Blocks (CBs) of up to Z bits, each with an additional CB CRC. Each CB is coded by means of a rate one-third turbo encoder with two 8-state constituent encoders with generator polynomial $G(D) = \left[1, \ \frac{1+D+D^3}{1+D^2+D^3}\right]$, identical to the one used in W-CDMA [48]. Per-CB rate matching is then applied to adapt the overall resulting bits to the TB size of G bits. The rate matching block is also tasked with generating different redundancy versions of the CB bits needed for HARQ retransmission operation [49, 50] (see Section 4.1 for a more detailed description of the HARQ-related procedures).

2.2.4. Channel Adaptive Feedback

LTE implements AMC, as well as closed-loop MIMO in order to adapt the transmission rate to the instantaneous channel conditions reported by the feedback. Depending on the transmission mode, LTE requires the calculation of up to three different feedback values at the receiver, which are explained in the subsections below.

2.2.4.1. Channel Quality Indicator Feedback

The Channel Quality Indicator (CQI) signals on a per-codeword basis the highest of the 15 Modulation and Coding Schemes (MCSs) specified in Table 2.5 that ensures, given measured actual channel conditions, a BLER lower or equal to 10 % [51, 52].

Table 2.5.: Modulation scheme, Effective Code Rate (ECR) of the channel encoder, and data (coded) bits per modulated symbol for each of the LTE-defined CQIs.

CQI	Modulation	ECR	bits/symb	CQI	Modulation	ECR	bits/symb
0	out of range			8	16-QAM	0.48	1.91
1	4-QAM	0.08	0.15	9	16-QAM	0.60	2.41
2	4-QAM	0.12	0.23	10	64-QAM	0.46	2.73
3	4-QAM	0.19	0.38	11	64-QAM	0.55	3.32
4	4-QAM	0.30	0.60	12	64-QAM	0.65	3.90
5	4-QAM	0.44	0.88	13	64-QAM	0.75	4.52
6	4-QAM	0.59	1.18	14	64-QAM	0.85	5.12
7	16-QAM	0.37	1.48	15	64-QAM	0.93	5.55

The CQIs specify code rates between 0.08 and 0.92, and employ 4-QAM, 16-QAM, or 64-QAM modulation alphabets. This is translated into an effective number of data bits per modulated symbol ranging from 0.15 to 5.55, as listed in Table 2.5. As

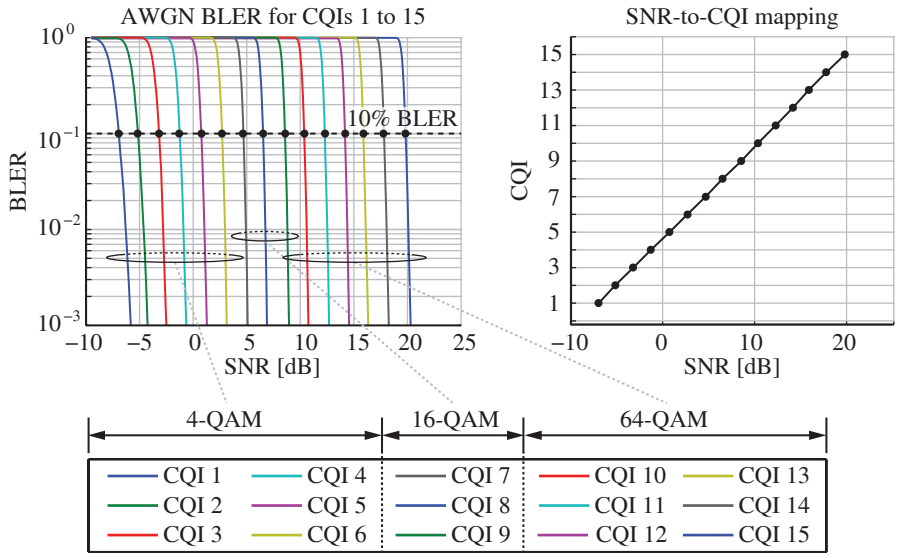

Figure 2.8: SNR-to-CQI mapping. Left: CQI BLER curves. Right: CQI mapping obtained from the 10 % BLER points.

such, for the MCS defined by each CQI, a mapping between the 10% BLER point the BLER curve of the corresponding MCS and each CQI value can be utilized, which is depicted in Figure 2.8. It should be noted, however, that such a Signal to Interference and Noise Ratio (SINR)-to-CQI mapping depends on the type of receiver. In the same channel conditions, a better receiver (for example a receiver implementing interference cancellation) would be able to report a higher CQI than a simpler or poorly-implemented one.

2.2.4.2. Precoding Matrix and Rank Feedback

The MIMO spatial multiplexing modes of LTE, which comprise the OLSM and CLSM transmit modes, require of additional feedback compared to the single transmit antenna of TxD cases. Rank Indicator (RI) feedback is required by both OLSM and CLSM, while Precoding Matrix Indicator (PMI) feedback is employed just by the CLSM mode [53] (see Section 2.2.1).

The feedback strategy is designed to calculate the PMI and RI combination that maximizes the number of receivable bits by the UE, which can be obtained by maximizing the sum Mutual Information (MI) for all possible PMI and RI combinations and, due to the constraint of a wideband RI, choosing that with the rank choice with the highest sum MI over all RBs [51, 54].

Since in OLSM the precoder choice is predetermined, the feedback calculation can, in this case, be shortened to the search of the RI that maximizes the sum MI over all RBs.

Table 2.6.: LTE codebook for CLSM mode and two transmit antennas for each of the possible number of layers (ν) [39].

Layers (ν)	Precoder codebook
1	$\frac{1}{\sqrt{2}}\begin{bmatrix}1\\1\end{bmatrix}$, $\frac{1}{\sqrt{2}}\begin{bmatrix}1\\-1\end{bmatrix}$, $\frac{1}{\sqrt{2}}\begin{bmatrix}1\\\mathrm{i}\end{bmatrix}$, $\frac{1}{\sqrt{2}}\begin{bmatrix}1\\-\mathrm{i}\end{bmatrix}$
2	$\frac{1}{2}\begin{bmatrix}1&1\\1&-1\end{bmatrix}$, $\frac{1}{2}\begin{bmatrix}1&1\\\mathrm{i}&-\mathrm{i}\end{bmatrix}$

Although desirably the PMI and RI feedback combination would be sent for each subcarrier, one PMI value is sent per RB (12 subcarriers), while for the RI, just a single wide-band value for the whole bandwidth is transmitted. These reductions were imposed by the need of reducing signaling traffic.

Table 2.6 lists the available precoders for the two-transmit-antenna case. For the four-antenna case, the codebook size increases to sixteen precoders, supporting up to four layers.

2.3. MAC Layer

The Medium Access Control (MAC) layer controls the access to the transmission medium. It provides data transfer and radio resource allocation services to upper layers, while the physical layer provides it with lower level data transfer services, signaling (HARQ feedback and scheduling requests), as well as channel measurements such as PMI, RI, and CQI reports [55]. Implementation-wise, the MAC layer is realized by a scheduler, which discretionally decides the PHY resource allocation for each UE according to its applied scheduling algorithm and the channel state information received from the PHY layer, as shown in Figure 2.9.

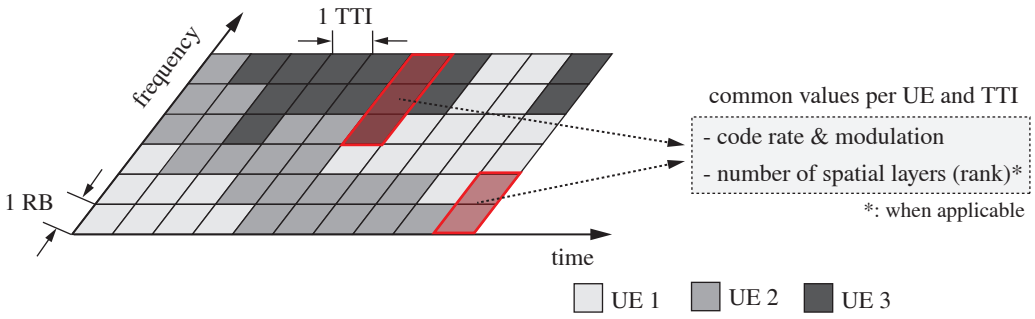

Figure 2.9: Example time-and-frequency domain scheduling in LTE. On a given TTI, each UE can be assigned a set of RBs, which is coded employing a common single MCS. If SM is employed, while the precoder choice can be frequency-selective, a common rank (number of layers) is employed over the whole set of RBs scheduled to the UE.

In LTE, multi-user diversity is exploited in both the time and frequency domains. UEs are assigned a set of RBs over time, thus exploiting both degrees of freedom (individual subcarrier allocation would require an excessive amount of signaling). While the exact RB allocation mechanism can vary between different modes [53], the procedure comprises the allocation of frequency resources to one or more UEs, as well the number of spatial layers, precoding, and MCS [56]. In the time domain, a scheduling granularity of one millisecond, corresponding to the subframe duration, is applied.

According to the feedback received from the UEs, a scheduler must appropriately assign transmit mode, MCS, PHY resource allocation, and, if applicable, a suitable number of spatial layers and precoding matrix. Exploiting these degrees of freedom, the goal of a scheduler is typically to try to achieve maximum throughput while maintaining a certain degree of fairness [56–59].

3. Physical Layer Modeling and LTE System Level Simulation

In order to evaluate the system level performance of a wireless network, complex simulations encompassing a high number of network elements and its interconnecting links are employed. By upscaling the number of simulated links and network elements, it is not only possible to assert if link level improvements do also improve network performance, but also to test and evaluate the algorithms controlling the PHY and MAC layers. Most commonly, system level simulations are employed to evaluate the performance of scheduling and PHY resource allocation [59–61], the impact of traffic models [62], or multi-user gain [63].

A straightforward and conceptually simple approach to system level performance evaluation would be to, for each link, perform all of the PHY and MAC layer procedures. Despite being simple, this approach does not scale well and results in impractical simulation times due to the high computational complexity of the channel coding/decoding procedures and specially the MIMO receiver [64–66].

Link level simulations are normally evaluated for a range of Signal to Noise Ratios (SNRs) or similar measures such as E_b/N_0 [67], for which link performance is evaluated in terms of throughput. For the smallest defined LTE system bandwidth of 1.4 MHz, which results in smallest possible simulation run time, a typical link level simulation lasts in the order of hours, depending on the employed MCSs employed, MIMO configuration and receiver [68].

In order to generate an interference-limited scenario analogous to a network deployment, typically a tri-sectorized hexagonal cell layout with no less than two rings of sites, each with three sectors is employed [69], such as the setup depicted in Figure 3.1. However, in order to correctly capture the effects of Multi-User (MU) gain

both due to the OFDMA resource allocation the spatial UE distribution, simulations with a higher bandwidth (LTE supports a transmission bandwidth of up to 20 MHz) and a high per-cell UE count are necessary, further increasing the potential computational complexity of system level simulations relative to a single-link simulation.

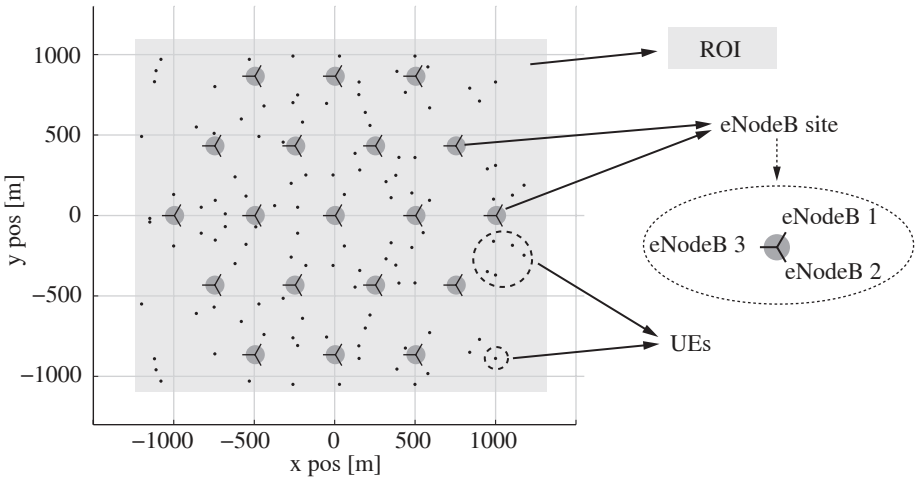

Figure 3.1: Typical system level simulation setup consisting of an hexagonal grid of 19 sites, each containing three eNodeBs (sectors). Users are placed randomly over the Region Of Interest (ROI), covering in this case a rectangle of roughly 2 500×2 200 meters. In this example, two UEs are placed per eNodeB.

Without taking into account extra complexity overhead, a simple simulation employing the aforementioned cell layout with two UEs per cell and a 20 MHz bandwidth would have a complexity 950 times higher than a 1.4 MHz single-user link level simulation due to the increase of the number of RBs from 6 to 100 and the number of eNodeBs from one to 57 (19 sites, 3 eNodeBs/site)[1]. If implemented via link level simulations, such a typical LTE system level simulation would require a simulation time in the order of months, which is clearly not practical.

3.1. System Model

As in other contemporary communication systems, such as W-CDMA or IEEE 802.11n, LTE employs Bit-Interleaved Coded Modulation (BICM), which has been shown to improve performance compared to systems employing symbol-wise interleaving [70]. Conceptually, the PHY layer procedures described in Chapter 2 can be

[1] Although the feedback would still need to be computed for the whole bandwidth by each UE, it has here been assumed that overall complexity is determined by the MIMO receiver complexity. As the cell PHY resources are shared by all attached UEs, the UE count is thus ignored in the calculation.

described as a BICM system comprised of the elements listed below [71, 72], which are also shown in Figure 3.2:

- A transmitter, comprised of a channel coder, a bit interleaver (Π), and a modulator ($\mathcal{M}$). It maps the input bit stream $\mathbf{b}$ to the transmit vector $\mathbf{x}$.
- A channel, which outputs the symbol vector $\mathbf{y}$ and defines a transition probability density function (pdf) $p_\theta(\mathbf{y}|\mathbf{x})$ depending on the channel state, which is denoted as θ.
- A receiver, which outputs the received bit stream $\hat{\mathbf{b}}$. It is comprised of an equalizer and demodulator $\left(\mathcal{M}^{-1}\right)$, de-interleaver $\left(\Pi^{-1}\right)$, and channel decoder.

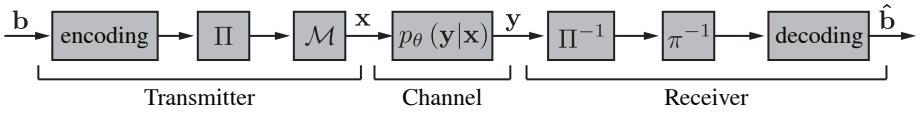

Figure 3.2: BICM transmission model. The model comprises bit coding/decoding, bit interleaving/deinterleaving, and symbol mapping/demapping, as well as a channel, modeled as a transition probability density function.

As shown in Chapter 2, bit coding and interleaving in provided by a turbo coder combined with rate matching. The symbol mapping $\mathcal{M}$ is implemented by means of a 4, 16, or 64-QAM constellation with Gray mapping [39].

The channel over which the symbol vector $\mathbf{x}$ is transmitted is modeled as a combination of a channel impulse response and Additive White Gaussian Noise (AWGN). Assuming an LTE system with N_{TX} transmit antennas and N_{RX} receive antennas, the signal received at the r-th antenna, denoted as y_r, can be expressed in the time domain as the sum of the signal received from each of the N_{TX} transmit antennas with a later addition of AWGN noise:

$$y_r = \sum_{t=1}^{N_{\mathrm{TX}}} (h_{t,r} * x_t) + n_r, \tag{3.1}$$

where the signal from the t-th transmit antenna, denoted as x_t is convolved ($*$) with the channel impulse response of length τ between the t-th transmit to the r-th receive antenna, denoted as $h_{t,r}$.

Assuming a CP at least as long as the length of the channel (τ), the CP introduced in the OFDM signal generation (see Figure 2.6 in Section 2.2) eliminates inter-symbol interference and allows for the channel impulse response $h_{t,r}$ for each OFDM symbol to be expressed as a complex-valued scalar. Stacking the $h_{t,r}$ values into a $N_{\mathrm{RX}} \times N_{\mathrm{TX}}$ matrix $\mathbf{H}$, the received symbol vector $\mathbf{y}$ of length N_{RX} can be expressed as

$$\mathbf{y} = \mathbf{H}\mathbf{x} + \mathbf{n}, \tag{3.2}$$

where $\mathbf{H}$ is the effective channel matrix mapping the transmitted data symbols to the received data symbols (i.e., it includes, if present, the precoding, as shown in Section 2.2.1). The vector of length N_{TX} containing the modulated data symbols is denoted as $\mathbf{x}$, while the vector of length N_{RX} containing the per-receive-antenna AWGN noise is denoted as $\mathbf{n}$.

Thus, and in a very simplified way, the equivalent BICM transmission-reception chain from Figure 3.2 can be rewritten for the LTE case as shown in Figure 3.3.

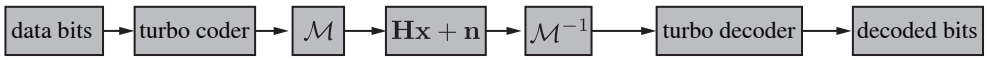

Figure 3.3: Equivalent LTE BICM transmitter-receiver chain.

The objective of the Link-to-System (L2S) model is, given a parametrization of the inputs, to predict the performance of the link; in this case, the achieved throughput over the link.

In order to simplify this problem, it can be divided in two parts, which jointly model the performance of the link [73, 74]: a *link quality model* (alternatively referred to in literature as link measurement model) and a *link performance model*.

The link quality model, as its name implies, outputs a metric quantifying the quality of the received signal after reception and equalization. Since this metric has to reflect the quality of the input to the turbo decoder, a straightforward choice is the post-equalization SINR [75]. With the post-equalization SINR, the link performance model maps this received signal quality measure into BLER and throughput based on the code rate and the MCS employed for the transmission.

Figure 3.4 illustrates the separation of the link into a link quality and a link performance model, as well as the inputs necessary to perform each step. Since the actual output of the demapper are Log-Likelihood Ratios (LLRs) and not post-equalization SINRs, the $\mathcal{M}^{-1}$ block is separated into an equalization block, denoted as $\mathbf{H}^{-1}$, and a demapping block, denoted as $\mathcal{D}$, pertaining to the link quality and link performance models, respectively.

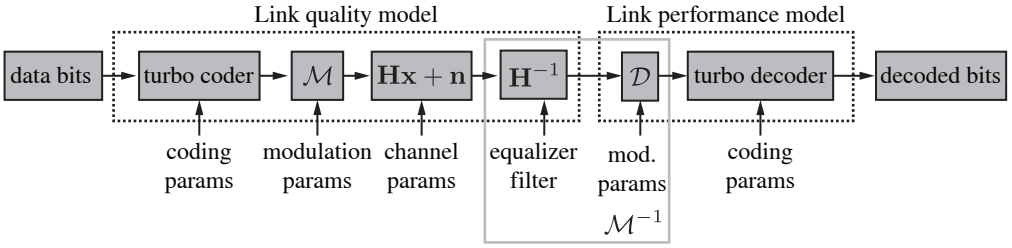

Figure 3.4: Separation of the LTE link into link quality and link performance model. The inputs parametrize the modeled PHY procedures of each of the steps.

The model depicted in Figure 3.4 is, however, a simplification of the actual L2S model. While Equation (3.2) does depict a single link, it does not take into account multiple interfering eNodeBs. To include multiple base stations, we can express $\mathbf{y}_0$ as

$$\mathbf{y}_0 = \mathbf{H}_0\mathbf{x}_0 + \mathbf{n} + \sum_{i=1}^{N_{\text{int}}} \mathbf{H}_i\mathbf{x}_i, \tag{3.3}$$

where the subindex i denotes for $i = 0$ the desired signal and for $i = 1 \dots N_{\text{int}}$ the signal from each of the N_{int} eNodeBs. For system level simulation, a set of eNodeBs are spatially distributed over an area, each of them communicating to their attached UEs via a link, which is modeled after the steps shown in Figure 3.4.

Thus, expanding the model depicted in Figure 3.3 to the whole network and adding the PHY layer procedures described in Chapter 2, we can identify the following components of the L2S model, as well as its connections to the link quality model (post-equalization SINR) and the link performance model (BLER and throughput):

- Network layout: The network layout describes where all of the transmitting eNodeBs are located relative to the receiver, as well as how they are configured. This includes not only the position, but also the azimuth and antenna type/tilt. Due to the decomposition of the fading experienced on the link into spatially-dependent and time-dependent parts (see Section 3.1.1), the network layout determines the macroscopic fading factors, which scale the received power. The network layout is incorporated into the link quality model and is separated into a pathloss, shadow fading, and antenna gain components.
- Small scale fading: Assumed independent of the position, small-scale fading represents fast, frequency-selective channel variations over time and is incorporated into the link quality model.
- Scheduling: The scheduler implements the MAC resource allocation procedures detailed in Section 2.3. For link modeling purposes, the PHY resource allocation and precoder choice applied to each of the links alter the set of subcarriers which are to be taken into account by the link measurement model, as well as the effective channel matrix $\mathbf{H}$ employed in the equalizer filter, and thus are part of the link-measurement model. On the link performance side, the MCS required to map the post-equalization SINR value to the appropriate modulation-and-coderate-dependent performance curves, as well as the RBs where the assigned TB is allocated. On the link quality model side, knowledge of the applied precoding is required to calculate the post-equalization SINR.

Figure 3.5 describes the aforementioned inputs to the link quality and link performance models, which are described in detail in Sections 3.1.1 and 3.1.2, respectively.

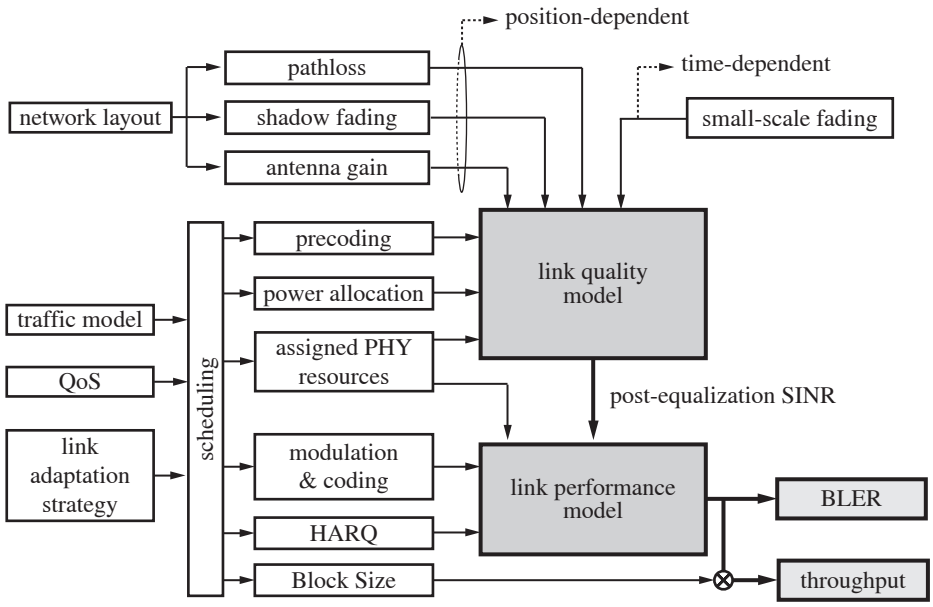

Figure 3.5: LTE Link-to-System model.

3.1.1. Link Quality Model

The formal definition of the link quality model is that it models the measurements used for link adaptation and resource allocation [73]. It can be interpreted as a measure of the quality of the signal being received, for which the post-equalization SINR of the data symbols is employed as metric in this L2S model with a block fading assumption (i.e., the channel is assumed constant over the duration of each 1 ms-long subframe). With the block fading assumption, the per-subcarrier-and-subframe post-equalization SINR requirements are 12 000 SINR points/TTI for the 20 MHz LTE bandwidth case (100 RBs, 12 subcarriers/RB). However, complexity can be further reduced by only considering a subset of the subcarriers [76].

In order for the necessary assumption of a flat channel per subcarrier, the maximum channel length, denoted as $\tau_{\max}$, cannot exceed that of the Cyclic Prefix (CP). For the normal CP configuration and subcarrier spacing of 15 kHz, the maximum CP length is of 4.7 μs (5.2 μs for the first symbol, 4.7 μs for the other symbols, but the worst-case scenario is considered). The minimum possible LTE coherence bandwidth employing the normal-length CP is thus

$$B_{\mathrm{LTE}} = 1/\tau_{\max} \approx 212\,\mathrm{kHz} \approx 1.2\,B_{\mathrm{RB}}, \tag{3.4}$$

which is rounded to one RB (180 kHz) due to the need to have at least one feedback value per RB for CQI reporting. In terms of L2S modeling, one subcarrier per RB would be enough, but planning for future extensions of the L2S modeling that could model the degradation when employing longer channels, it was decided to employ

a decimation factor of six, which results in $2 \cdot N_{\mathrm{RB}}$ SINR values for the whole LTE system bandwidth shown in Table 3.1. Additionally, due to the averaging nature of the rank and precoding feedback algorithms [51, 54], at least two subcarrier SINR values per RB are desirable.

Table 3.1.: Number of calculated SINR samples for the different LTE bandwidths.

Channel bandwidth (B_{channel}) [MHz]	1.4	3	5	10	15	20
Number of SINR samples ($2 \cdot N_{\mathrm{RB}}$)	12	30	50	100	150	200

3.1.1.1. Post-equalization SINR and Trace Generation

As aforementioned, the complexity of the link quality model can be reduced by considering only a subset of the total post-equalization SINRs. For the calculation of the SINR itself, a simple linear receiver, the Zero Forcing (ZF) receiver, is considered. Since system level simulations are to be used where Multi-User (MU) diversity is also expected to be exploited (for single-link simulations one would rather employ link level simulations), it can be argued that for a large number of users, the ZF receiver approaches the average performance of the optimal receiver, since MU diversity effect can compensate for poorly conditioned channel matrices [77].

Assuming perfect channel knowledge, where the accent mark [ˆ] denotes a receiver estimate, the estimated received symbol vector $\hat{\mathbf{x}}$ can be expressed as

$$\hat{\mathbf{x}} = \mathbf{G}\mathbf{y} = \mathbf{G}\left(\mathbf{H}_0\mathbf{x}_0 + \mathbf{n} + \sum_{i=1}^{N_{\mathrm{int}}} \mathbf{H}_i\mathbf{x}_i\right), \tag{3.5}$$

where $\mathbf{G}$ is the receive filter, which for the ZF receiver is calculated as the pseudoinverse of $\mathbf{H}$ and expressed as

$$\mathbf{H}^{+} = \left(\mathbf{H}^{\mathrm{H}}\mathbf{H}\right)^{-1}\mathbf{H}^{\mathrm{H}}, \tag{3.6}$$

where $\mathbf{H}^{\mathrm{H}}$ denotes the Hermitian transpose of $\mathbf{H}$.

For the cases where a spatial multiplexing (OLSM or CLSM) or TxD (based on the Alamouti STBC [41]) mode is employed, $\mathbf{H}$ denotes the effective channel matrix. For the SM cases, it can be calculated as the combination of the actual channel matrix and the linear precoder $\mathbf{W}$ that maps the ν transmitted symbols[2] to the N_{TX} transmit antennas. For TxD, the precoding-equivalent operation is shown for

[2] In the LTE standard, the number of simultaneously transmitted symbols is referred to as the number of layers, and is denoted as ν (see Chapter 2 and Section 2.2.2).

the $N_{\mathrm{TX}} = 2$ example and is expressed as

$$\underbrace{\begin{bmatrix} y_0 \\ y_1^* \end{bmatrix}}_{\tilde{\mathbf{y}}} = \underbrace{\begin{bmatrix} \mathbf{h}^{(0)} & \mathbf{h}^{(1)} \\ \mathbf{h}^{(1)*} & -\mathbf{h}^{(0)*} \end{bmatrix}}_{\tilde{\mathbf{H}}} \cdot \underbrace{\begin{bmatrix} x_0 \\ x_1 \end{bmatrix}}_{\tilde{\mathbf{x}}} + \underbrace{\begin{bmatrix} n_0 \\ n_1 \end{bmatrix}}_{\tilde{\mathbf{n}}}, \tag{3.7}$$

where $\mathbf{h}^{(0)}$ and $\mathbf{h}^{(1)}$ contain the channel coefficients from the first and second transmit antennas to the N_{RX} receive antennas.

Denoting as γ_i the post-equalization SINR of the i-th layer (ν symbols are simultaneously transmitted), $\mathbf{A} = \mathbf{H}_0^+ \mathbf{H}_0$, $\mathbf{B}_0 = \mathbf{H}^+$ and $\mathbf{C}_l = \mathbf{H}_0^+ \mathbf{H}_l$ (l-th interferer), and denoting the matrix elements as $a_{ij} \triangleq \mathbf{A}[i,j]$, we can alternatively express the post-equalization SINR of the i-th layer (γ_i) [78] as:

$$\gamma_i = \frac{|a_{ii}|^2 P_{i,0}}{\sum_{j \neq i} |a_{ij}|^2 P_{j,0} + \sigma_n^2 \sum_{k=1}^{\nu} |b_{ik}|^2 + \sum_{l=1}^{N_{\mathrm{int}}} \sum_{m=1}^{\nu} |c_{l,i,m}|^2 P_{l,m}}, \tag{3.8}$$

where $P_{i,m}$ is the average received power at layer i from the m-th eNodeB ($m = 0$ is the eNodeB from which the data transmission is received, while $m = 1, \ldots, N_{\mathrm{int}}$ correspond to interfering eNodeBs) and σ_n^2 the receiver noise, assumed uncorrelated and after scaling with the receiver noise figure. Assuming a homogeneous per-layer power distribution $P_{\mathrm{L}} = P_{\mathrm{TX}}/\nu$, which is the case in the LTE standard, we define the ζ_i, ξ_i, ψ_i, and θ_i fading parameters for the i-th layer as

$$\zeta_i = |a_{ii}|^2, \qquad \xi_i = \sum_{j \neq i} |a_{ij}|^2, \qquad \psi_i = \sum_{k=1}^{\nu} |b_{ik}|^2, \qquad \theta_{i,l} = \sum_{m=1}^{\nu} |c_{l,i,m}|^2, \tag{3.9}$$

where for each layer i, ζ_i represents the fraction of P_{L} going to the signal part of the SINR, ξ_i the inter-layer interference, ψ_i the noise enhancement, and $\theta_{i,l}$ the interference from the l-th interfering eNodeBs.

To further ease the L2S modeling, the fading experienced by the transmitted signal is decomposed into a macro-scale loss and a small-scale loss. The average receive signal power between the t-th transmit antenna and the r-th receive antenna ($P_{r,t}$) is thus expressed by the following link budget:

$$\underbrace{P_{r,t}}_{\substack{\text{received} \\ \text{power}}} = \underbrace{|h_{r,t}|^2}_{\substack{\text{small-scale} \\ \text{fading}}} \cdot \underbrace{L_{\mathrm{shadow}} \cdot L_{\mathrm{pathloss}} \cdot G_{\mathrm{antenna}}}_{\substack{\text{macro-scale} \\ \text{fading}}} \cdot \underbrace{P_{\mathrm{TX}}/N_{\mathrm{TX}}}_{\substack{\text{per-antenna} \\ \text{transmit power}}}. \tag{3.10}$$

In Equation (3.10), the transmit power P_t is scaled by the following factors:

- G_{antenna}: Antenna directivity. An analytical or measured radiation pattern that

can be either a 2D or a 3D pattern. In the last case, it combines a horizontal and vertical component with an optional mechanical/electrical tilt [79].

- L_{pathloss}: A distance-dependent pathloss between the transmitter and the receiver.
- L_{shadow}: Shadow fading, which models slow-changing deviations from the average pathloss values that model irregularities such as geographical features. Modeled as a zero-mean space-correlated lognormal distribution.
- $|h_{r,t}|^2$: Assumed to be a χ^2 distribution with a number of degrees of freedom N of two, as the underlying distribution of h is assumed to be circular symmetric complex normal with an average power of one.

As the macro-scale parameters are scalars applied to all of the entries of the MIMO channel matrix, it can be trivially decomposed into a normalized[3] channel matrix $\mathbf{H}$ multiplied by the factors L_{pathloss}, L_{shadow}, and G_{antenna}. Applying the link budget of Equation (3.10) to Equation (3.9) we can rewrite Equation (3.9), expressing the subcarrier post-equalization SINR for layer i as

$$\gamma_i = \frac{\zeta_i \, P'_{\text{L},0}}{\xi_i P'_{\text{L},0} + \psi_i \sigma_n^2 + \sum_{m=1}^{N_{\text{int}}} \theta_{i,m} \, P'_{\text{L},m}}, \tag{3.11}$$

where $P'_{\text{L},m} = P_{\text{L},m} \cdot G_{\text{antenna},m} \cdot L_{\text{pathloss},m} \cdot L_{\text{shadown},m}$, and the index m denotes the transmitting eNodeB ($m = 0$ for the target transmitter and $m = 1, \ldots, N_{\text{int}}$ for the interferers).

Decomposing the combined fading experienced over the link into a slowly-changing position-dependent macro-scale component and a faster-changing small-scale [80] enables to model the fading as two separate offline-computable components: one position-dependent and one time-dependent.

3.1.1.2. On the Modeling of OLSM and the Block Fading Assumption

Over the course of this chapter, it has been stressed that block fading is assumed, i.e., unchanging channel conditions for the duration of a TTI, and this assumption is applied to the calculation of the post-equalization SINR in Section 3.1.1.1.

However, it is clearly mentioned in Section 2.2.1.2 that the OLSM transmit mode is based on cyclically applying a set of precoders, as well as a shift of the signal, to each modulated symbol during one TTI. Thus, even if a constant channel is considered, the *effective channel*, i.e., the combination of the channel and the precoder is not constant during a TTI due to the applied CDD and cyclical precoding.

[3] Through the course of this thesis, a normalized channel matrix refers to one in which all of its entries have a mean power of one.

For the two transmit antenna case, the precoder set consists of a single precoder, and only two possible values for $\mathbf{D}$ are possible. For the L2S model, and for the sake of simplicity, the time-variability of $\mathbf{D}$ has been discarded, thus effectively obtaining a block fading scenario.

However, for the case of four transmit antennas, the precoder set consists of four precoders, with the added three or four (for three and four layers, respectively) possibilities for $\mathbf{D}$. To take into account the use of multiple precoders, for each subcarrier sample, a different precoder is assigned, such that the employed precoder $\mathbf{W}$ is the i-th one in the precoder set, where $i = \mathrm{mod}\,(\text{subcarrier index}, 4)$. As in the prior case, $\mathbf{D}$ is is treated as constant.

The impact of these simplifications in the accuracy of the link abstraction model compared to link level results is shown in Section 3.2.1. Results show that, although as expected model accuracy for the OLSM mode with four transmit antennas is worse than that obtained with the other modes/antenna configurations, significant throughput degradation is limited to the high-SNR 4×2 case.

3.1.1.3. Channel Trace Generation

From the decomposition of the channel in a small-scale fading component $\mathbf{H}$ and a macro-scale component, it becomes possible to precompute the fading parameters ζ, ξ, ψ, and θ offline from a normalized channel matrix $\mathbf{H}$, a task of high computational cost due to the involved complex-valued matrix multiplications and inversions. At run time, only simple scalar multiplications will then be needed, significantly reducing complexity compared to link level simulations.

Further decreasing complexity, individual traces for each of the links can be obtained by choosing independent random starting points from a single trace. As long as the original trace is of sufficient length, the individual sub-traces can be assumed to be independent [74].

As noted in Section 3.1.1.1, $\mathbf{H}$ refers to the effective channel matrix. While for the TxD mode this represents no change in terms of additional complexity[4], for the OLSM and CLSM modes, further complexity due to the rank (OLSM and CLSM) and precoder selection (CLSM) is present.

The trace generation for CLSM is detailed below. As OLSM can be considered a simplified case of CLSM with no PMI feedback (although with the addition of CDD), the CLSM trace generation procedure applies also for the OLSM case.

[4] As all of the layers will experience the same fading due to the STBC, only a one-layer trace needs to be stored.

As detailed in Section 2.2.1.3, a UE reporting feedback in the CLSM mode will report the PMI-RI combination that maximizes its throughput, and will employ for the feedback calculation the estimated channel matrix calculated from the pilot symbols transmitted by the eNodeB.

For each RI choice, and as shown in Appendix A, the optimum PMI and RI can be calculated offline indepenently of the SNR. However, as the RI is wideband and not RB-wise, it needs to be calculated at run-time to optimize the sum capacity over the whole bandwidth or part of it. The latter setup allows the model to deal with cases where the total bandwidth is partitioned, such as in Fractional Frequency Reuse (FFR).

The channel trace memory requirements are as follow: the fading parameters are stored for each TTI (block fading), thus resulting in four scalars per TTI, layer option, and subcarrier sample. As the parameters ζ and ξ are known to be one and zero, respectively, due to the ZF receiver and perfect channel knowledge assumption, they can be omitted from the trace, effectively halving the trace size.

Assuming single-precision floating-point scalars, the memory requirements per TTI and RB, denoted as $B_{\mathrm{TTI,RB}}$, are

$$B_{\mathrm{TTI,RB}} = \sum_{\nu=1}^{\nu_{\max}} \left(\nu \cdot \underbrace{32}_{32 \text{ bits/scalar}} \cdot \underbrace{2}_{\not{\zeta},\not{\xi},\psi,\theta} \cdot \underbrace{2}_{2 \text{ samples/RB}} \right), \tag{3.12}$$

where ν are all of the possible rank choices, from one to $\nu_{\max} = \min(N_{\mathrm{TX}}, N_{\mathrm{RX}})$. For each of the two required parameters ψ and θ, two values/RB are stored, each requiring 32 bits of memory are required in single-precision floating point, reflected on the parameters in Equation (3.12). Although the optimum precoder choice is pre-calculated, at run time the rank choice has still to be performed. Thus, the channel trace includes values for each of the $\nu_{\max}$ rank possibilites. For the calculation of the optimum precoder, a mutual-information-maximizing algorithm is employed [51, 54]. Table 3.2 lists the channel trace memory requirements per second of stored trace for the bandwidths defined in the LTE standard.

Table 3.2.: Channel trace memory requirements in MByte per second of stored trace [MByte/s] for several LTE antenna and channel bandwidth configurations.

		Channel bandwidth [MHz]					
		1.4	3	5	10	15	20
$\min(N_{\mathrm{TX}}, N_{\mathrm{RX}})$	1	0.73	1.83	3.05	6.10	9.16	12.21
	2	2.20	5.49	9.16	18.31	27.47	36.62
	4	7.32	18.31	30.52	61.04	91.55	122.07

3.1.1.4. Macro-scale Fading

The distance-dependent macro-scale fading parameters can be precomputed offline and stored on a pixel map with a given resolution of p m/pixel, thus each pixel representing a square of $p \times p$ meters in the simulated ROI. The stored pathloss values are then applied at run time accordingly depending on the positions of the transmitter, receiver, and interferers. As listed in Section 3.1.1.1, the time-invariant and position-dependent macro-scale parameters are the pathloss, antenna gain, and shadow fading.

For the pathloss and antenna gain, typical scenarios and models are already well known and applied in standardized simulation scenarios for LTE [69].

The standard 2D radiation pattern G, dependent on the azimuth angle θ is

$$G(\theta) = -\min\left[12\left(\frac{\theta}{65°}, 20\,\text{dB}\right)\right], \text{ where } -180° \leq \theta \leq 180°, \tag{3.13}$$

with an antenna gain of 15 dB. Although the radiation pattern of any real antenna, such as the pattern shown in Figure 3.6 (right) can also alternatively be employed.

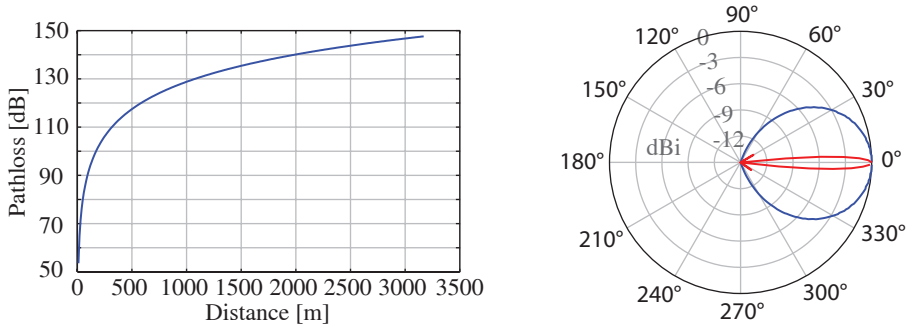

Figure 3.6: Left: Urban pathloss (2 000 MHz, 15 m base station antenna height over rooftop), as of [69]. Right: measured horizontal/vertical antenna radiation pattern from a KATHREIN 742212 antenna with no electrical tilt.

For the pathloss, known models already exist, such as [69, 81–83]. The following formula models the pathloss, denoted as L, for an urban or suburban area outside of the high-rise core [69], and is commonly employed in literature for system level simulations:

$$L = 40 \cdot \left(1 - 4 \cdot 10^{-3} \cdot M_{\text{TX}}\right) \cdot \log_{10}(R) - 18 \cdot \log_{10}(M_{\text{TX}}) + 21 \cdot \log_{10}(f) + 80\,\text{dB}, \tag{3.14}$$

where M_{TX} is the antenna pole height in meters, as measured from the average rooftop level, R is the base station-UE separation in kilometers, and f is the carrier frequency in MHz.

For an example case considering a carrier frequency of 2 000 MHz and a base station antenna height of 15 m above average rooftop level, the propagation model formula is simplified to the well known formula [69]

$$L = 128.1 + 37.6 \cdot \log_{10}(R), \tag{3.15}$$

which is shown in Figure 3.6 (left).

Combining the pathloss, antenna gain, and Minimum Coupling Loss (MCL)[5], a position-dependant macro-scale fading map depicting the losses from a given transmitter such as that in Figure 3.7 (left) can be obtained. The cell partitioning can be visualized by plotting the wideband SINR of the strongest signal on each point, denoted as Γ and not to be confused with the post-equalization SINR. The wideband SINR, depicted in Figure 3.6 (right), is calculated as

$$\Gamma = \frac{G_{\text{antenna}}\, L_{\text{macro},0}\, P_{\text{TX}_0}}{\sigma_n^2 + \sum_{m=1}^{N_{\text{int}}} L_{\text{macro},l}\, P_{\text{TX}_m}}. \tag{3.16}$$

The wideband SINR, also when applicable including shadow fading, can be employed as a measure of how close a UE is to the transmit antenna relative to the interferers, and is employed as such over the course of this thesis, especially in Chapter 5.

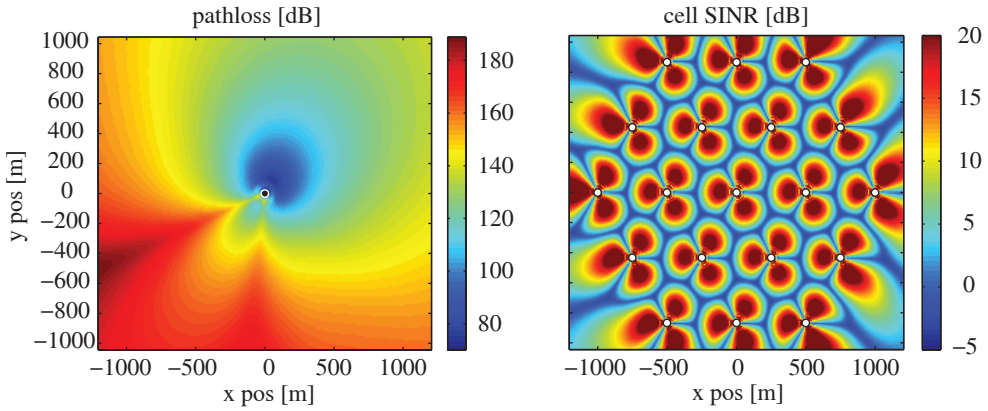

Figure 3.7: Left: pathloss and antenna gain map in dB. Pathloss and antenna gain as in Equation (3.15) and Figure 3.6. Antenna gain of 15 dBi. Right: resulting cell wideband SINR in dB.

[5] The MCL describes the minimum loss in signal between eNodeB and UE or UE and UE in the worst case and is defined as the minimum distance loss including antenna gains measured between antenna connectors. [69] defines it as 70 dB for urban cell deployments and 80 dB for rural cell deployments.

3.1.1.5. Shadow Fading

Shadow fading is modeled to represent the deviations from the average pathloss values due to geographical features such as terrain changes or buildings. It is generally modeled as a log-normal distribution with zero mean, which although could also be treated as a time-dependent process, is preferable to treat as position-dependent due to the convenience of storing it in map form.

A typical standardized cell layout sets a log-normal distribution with a standard deviation of 10 dB, as well as an inter-site correlation of 0.5 [69]. Since the shadow fading is interpreted as geographical variations, as sectors share the same site (i.e., geographical location), an inter-sector correlation factor of one is assumed.

In order to introduce spatial correlation to the points on each map, a method based on the Cholesky decomposition of the correlation matrix $\mathbf{R}$ is employed. This methods allows us to introduce spatial correlation to an uncorrelated log-normally-distributed vector.

Given an initial vector $\mathbf{a}$ of length K with a correlation matrix $\mathbf{R}_a = \mathbb{E}\{\mathbf{a}\mathbf{a}^{\mathrm{H}}\}$ equal to the identity matrix of size K ($\mathbf{I}_K$), a correlated vector $\mathbf{s}$ with a predefined correlation matrix $\mathbf{R}_s$ can be obtained by performing

$$\mathbf{s} = \mathbf{L}_s\mathbf{a}, \tag{3.17}$$

where $\mathbf{L}_s$ is the lower-triangular Cholesky decomposition of $\mathbf{R}_s$ and the correlation matrix of $\mathbf{s}$ is $\mathbb{E}\{\mathbf{s}\mathbf{s}^{\mathrm{H}}\} = \mathbf{L}_s\mathbf{L}_s^{\mathrm{H}} = \mathbf{R}_s$.

The values of the correlation coefficients in $\mathbf{R}_s$ follow an exponential model where correlation diminishes with distance, expressed as $r(x) = e^{-\alpha x}$ [84, 85], with the distance x in meters, and a typical value for α of $1/20$ [86].

As with the pathloss map, the shadow fading map is stored as pixels, with each pixel representing a square of $p \times p$ meters. Thus, for a map of size $M \times N$ pixels, a correlation matrix of size $M \cdot N \times M \cdot N$ is required. As an example, the pathloss map in Figure 3.7 encompasses an area of $2\,080 \times 2\,402$ m, with a resolution of 5 m/pixel, resulting in a 416×481 matrix. The resulting correlation matrix would be $200\,096 \times 200\,096$, requiring around 300 GB of memory for the correlation matrix $\mathbf{R}_s$ alone assuming double-precision storage (8 bytes/value).

In order to reduce complexity, an extension of the method proposed in [87] is employed. In order to calculate the value of the space-correlated value s_n, just a set of neighboring pixels is taken into account. Since the correlated pixels have to be generated following a certain order, only the previously processed pixels are taken into account for the calculation of s_n. For a neighbor count of 12 and a row-wise processing order, the set of neighboring pixels $s_{n-1} \dots s_{n-12}$ is depicted in Figure 3.8

for the case of $n = 13$. Starting from an uncorrelated set $\mathbf{a}$, a correlated set $\mathbf{s}$ with a correlation matrix close to $\mathbf{R}_s$ can be obtained, with the correlation difference being due to taking into account the closest pixels instead of the whole map.

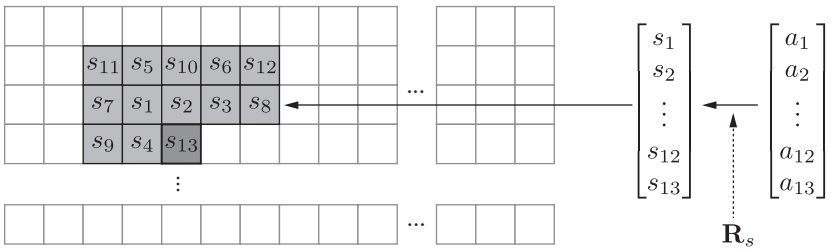

Figure 3.8: Generation of the space-correlated shadow fading map values ($\mathbf{s}$) from uncorrelated values ($\mathbf{a}$) for $n = 13$. Based on the previously-calculated correlated values s_1-s_{12}, a value s_{13} that satisfies the correlation matrix $\mathbf{R}_s$ is obtained.

As in [87], we define the vector $\tilde{\mathbf{s}}$ containing the already-processed neighbor positions $s_1 \dots s_{12}$, which have a correlation matrix $\tilde{\mathbf{R}}$. For $\mathbf{s} = \mathbf{L}_s\mathbf{a}$ to be satisfied,

$$\mathbf{s} = \mathbf{L}_s \begin{bmatrix} \tilde{\mathbf{L}}_s^{-1}\tilde{\mathbf{s}} \\ a_n \end{bmatrix}. \tag{3.18}$$

As the value we are interested in is s_n ($s_{n-1} \dots s_{n-12}$ have already been obtained), just the last row of $\mathbf{L}$ is needed. Denoting it as λ_n, s_n can be expressed as

$$s_n = \lambda_n^{\mathrm{T}} \begin{bmatrix} \tilde{\mathbf{L}}_s^{-1}\tilde{\mathbf{s}} \\ a_n \end{bmatrix}, \tag{3.19}$$

followed by an additional re-normalization step of $\mathbf{s}$ with a factor σ_a/σ_s in order to re-scale the power of the distribution.

The actual values of the correlation matrix $\mathbf{R}_s$ can be found in Appendix B.

In order to additionally introduce inter-site correlation, for the K sites, $\mathbf{a}'_1 \dots \mathbf{a}'_K$ initial log-normal uncorrelated maps are generated, plus an extra set $\mathbf{a}'_0$.

Given a fixed inter-site correlation factor r_{site}, the inter-correlated but spatially-uncorrelated maps $\mathbf{a}_i$ can be obtained as

$$\mathbf{a}_i = \sqrt{r_{\text{site}}}\,\mathbf{a}'_0 + (1 - \sqrt{r_{\text{site}}})\,\mathbf{a}'_i. \tag{3.20}$$

A resulting shadow fading map is depicted in Figure 3.9, as well as the resulting cell wideband SINR after combination with the pathloss and antenna gain macro-scale fading parameters. A standard deviation of $\sigma = 10\,\text{dB}$ is employed.

The depicted shadow fading map in Figure 3.9 (left) is one of the 19 maps (1 map/site) generated for a system level simulation scenario. They are generated

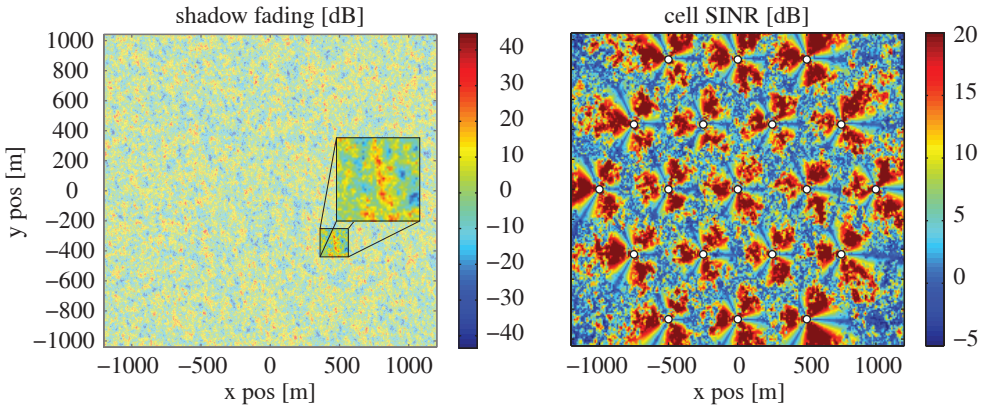

Figure 3.9: Left: shadow fading map in dB ($\mu = 0\,\text{dB}$, $\sigma = 10\,\text{dB}$). Zommed: detail of the introduced spatial correlation. Right: resulting cell wideband SINR in dB.

employing the 12-neighbor correlation matrix in Appendix B and an inter-site correlation of 0.5. Despite the introduced spatial correlation, the overall log-hormal distribution of each map is not altered. Figure 3.10 depicts the overlapped pdfs of each of the 19 shadow fading maps (in black), compared to the analytical pdf. The right plot depicts the inter-site correlation matrix, with (excluding the diagonal) a mean value of 0.5009 dB and a standard deviation of the mean values of 0.0042 dB.

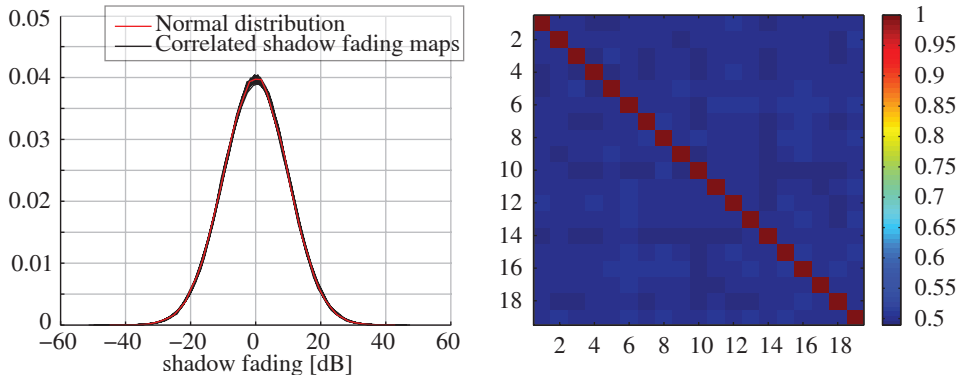

Figure 3.10: Left: comparison of the pdf of the obtained shadow fading maps in dB with a normal distribution with $\mu = 0\,\text{dB}$, $\sigma = 10\,\text{dB}$. Right: inter-site correlation matrix.

3.1.2. Link Performance Model

The channel quality measure output by the link quality model serves as input to the link performance model. As detailed in Section 3.1.1 and depicted in Figure 3.5, a subset of the subcarrier post-equalization SINRs parametrize the channel conditions on a per-spatial-layer basis.

For the RB set in which the UE is scheduled (if scheduled), the link performance

model combines the output of the link quality model with that of the applied modulation order and code rate and predicts the BLER of the received TB. Ultimately, given this frame error probability, the successful or erroneous receiving of the TB is randomly decided via a coin toss corresponding to the BLER probability. Combined with the TB size throughput is then determined, as depicted in Figure 3.11.

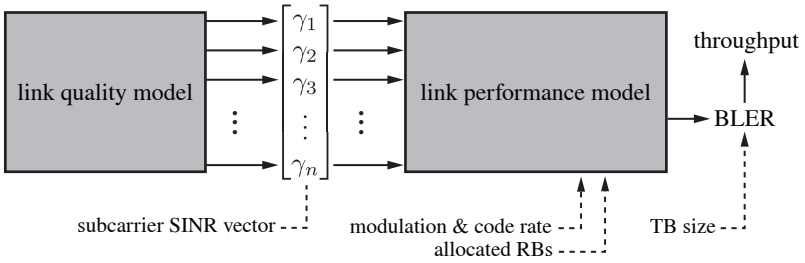

Figure 3.11: Link performance model. The output of the link quality model is combined with information regarding the allocated RBs, and the employed modulation/code rate.

The SINR-to-BLER mapping comprises an $(n+1)$-dimensional mapping of n post-equalization subcarrier SINRs values $(\gamma_1, \ldots, \gamma_n)$ and the modulation and coding employed to a single BLER value.

While theoretically possible, it is in practice unfeasibly complex to obtain a mapping table of the possible combinations of the n SINR values to a BLER value for each MCS. Additionally, the length of $\boldsymbol{\gamma}$ varies depending on the number of RBs scheduled to the UE, with a maximum value restricted by the LTE channel bandwidth (see Table 3.1).

Over time, several methods to first map the sub-carrier post-equalization SINR vector, denoted as $\boldsymbol{\gamma}$ to an effective SINR value (γ_{eff}) have been proposed [88–91]. While different names, such as Actual Value Interface (AVI) and Effective SINR Mapping (ESM) exist, both relate to the same concept of mapping $\boldsymbol{\gamma}$ to an effective SINR value γ_{eff}.

In order to compress the SINR vector $\boldsymbol{\gamma}$ into a single value γ_{eff}, Mutual Information Effective SINR Mapping (MIESM) [90, 91] is employed, as it does not require an empirical calibration step such as previous methods as long as codes that perform close to capacity are employed. The non-linear ESM averaging of MIESM is expressed as

$$\gamma_{\text{eff}} = \mathrm{I}_k^{-1}\left(\frac{1}{N}\sum_{n=1}^{N}\mathrm{I}_k\left(\gamma_n\right)\right), \tag{3.21}$$

where N is the length of the SINR vector and I_k the BICM capacity for the chosen modulation at the given value γ_n. The BICM capacity (I_k) for a modulation

encoding k bits per symbol [92] is expressed as

$$I_k(\gamma) = k - \mathbb{E}\left\{ \frac{1}{k} \sum_{i=1}^{k} \sum_{b=0}^{1} \sum_{z \in \mathcal{X}_b^i} \log \frac{\sum_{\hat{x} \in \mathcal{X}} \exp\left(- |Y - \sqrt{\gamma}(\hat{x} - z)|^2 \right)}{\sum_{\tilde{x} \in \mathcal{X}_b^i} \exp\left(- |Y - \sqrt{\gamma}(\tilde{x} - z)|^2 \right)} \right\}, \tag{3.22}$$

where $\mathcal{X}$ is the set of 2^k constellation symbols, $\mathcal{X}_b^i$ is the set of symbols for which bit i equals b and Y is complex normal with zero mean and unit variance. Figure 3.12 (left), depicts the BICM capacity curves for the 4-, 16-, and 64-QAM modulations employed in LTE.

Thus, MIESM effectively averages the subcarriers in the MI domain and then remaps the average MI value to SINR

The main limitation of this method is that all of the subcarriers in a TB need to employ the same modulation alphabet, which is fulfilled in the case of LTE transmissions [39, 45, 53].

The effective SINR (γ_{eff}) is then mapped by means of an AWGN BLER curve of the corresponding MCS to a BLER value. The AWGN BLER curves, obtained from LTE link level simulations, are shown in Figure 3.12 (right).

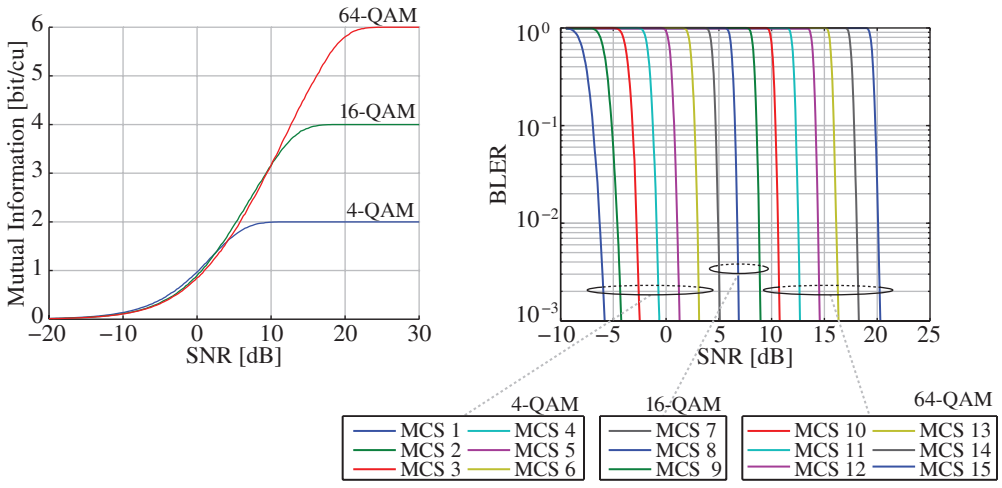

Figure 3.12: Left: BICM capacity curves for the 4-, 16-, and 64-QAM modulations employed in LTE. Right: AWGN SNR-to-BLER curves for the 15 MCSs defined in Table 2.5.

With the presented L2S interface, the link between link level simulations and the model applied at system level is reduced to simple precomputed AWGN BLER curves for each of the employed MCSs.

The AWGN-equivalent γ_{eff} represents an average SINR of the SINR vector $\boldsymbol{\gamma}$ in terms of MI, thus avoiding the need for a multi-dimensional SINR mapping, as well

problems related to the variable-length of γ due to the RB scheduling assignment or the bandwidth configuration. As a result, 15 AWGN link level simulations, one for each of the defined MCSs and each outputting an AWGN SNR-to-BLER curve, are the only computationally costly link level simulations required for the LTE L2S model. The full structure of the link performance model for the LTE L2S model is depicted in Figure 3.13.

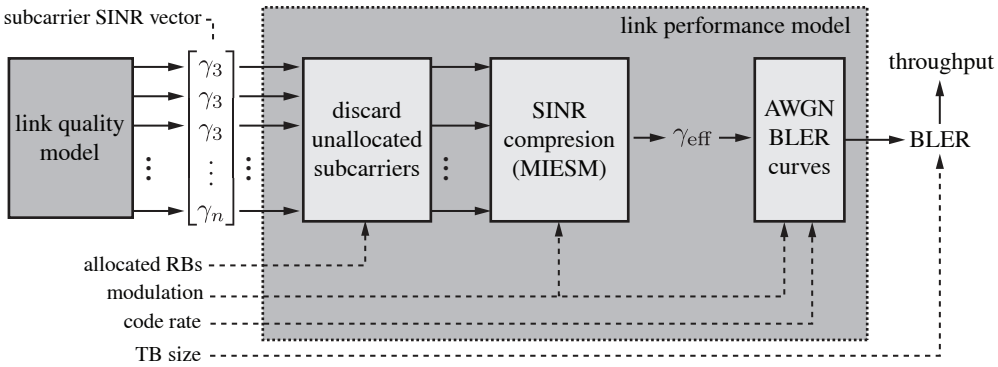

Figure 3.13: Link performance model for the LTE L2S model detailing the SINR compression step in the link performance model.

3.2. Link-to-System Model Validation

The objective of the link quality and link performance models, detailed in Sections 3.1.1 and 3.1.2, respectively, is to provide an accurate link throughput prediction which is fading-independent, and which requires of only the input of an AWGN mapping. This link-to-system structure [73] is applied to LTE MIMO transmissions employing a ZF receiver. With a negligible loss of accuracy, the more computationally-intensive MIMO precoder feedback is additionally performed offline, speeding-up simulation run-time, as detailed in Appendix A.

As accurate link abstraction models are laborious to design and implement, it is common to employ much simpler link abstraction models for system level simulation, such as capacity-based model suggested in the LTE standard [69]. Unless the focus is on link abstraction, it is often preferred to employ these much simpler capacity-based SNR-to-throughput mappings (in full or scaled and/or truncated form), such as in the cases of [93–95] (more focused on upper-layer protocols) and [96] (focused on handover).

As a throughput approximation for link abstraction purposes, [69] suggests to employ an approximation of the throughput obtained by means of AMC over an AWGN

channel by scaling and truncating the Shannon formula so that

$$C_{\text{Shannon}}(\gamma) = \begin{cases} 0, & \gamma < -10\,\text{dB} \\ 0.75\,\log_2(1+\gamma), & -10\,\text{dB} < \gamma < 17\,\text{dB} \\ \max\left(C_{\text{AWGN}}\right), & \gamma > 17\,\text{dB} \end{cases}, \tag{3.23}$$

where γ is the SNR and $\max\left(C_{\text{AWGN}}\right)$ the maximum spectral efficiency from a Single-Input Single-Output (SISO) AWGN LTE link level simulation with AMC.

Figure 3.14 depicts (from top to bottom) the difference in spectral efficiency between that of the unscaled, untruncated Shannon formula; the proposal in [69]; that obtained from single-user AWGN simulations with AMC; and that obtained on a more realistic frequency-selective ITU Pedestrian-A (5 km/h) channel [97].

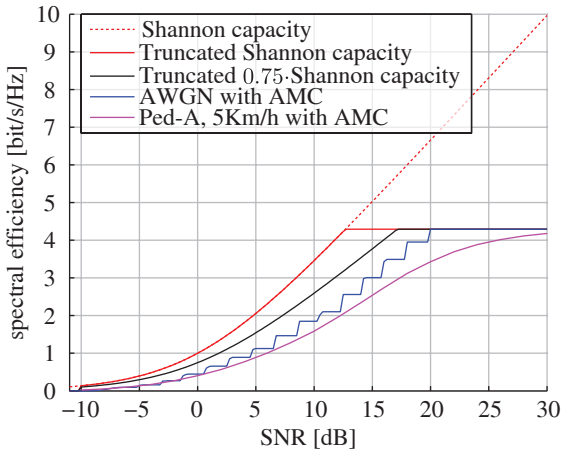

Figure 3.14: SNR-to-throughput mapping according to several assumptions and compared to Pedestrian-B 5 km/h results.

The results in Figure 3.14 depict the obvious statement that, in order to fit the Shannon capacity curve to more realistic channel conditions, ad hoc scaling and calibration of it for each specific channel characteristics are needed if significant deviations are to be avoided.

Thus, the first verification step of the link abstraction model is whether the throughput of a frequency-selective channel can be accurately modeled by means of the L2S model, when compared to link level results[6].

[6] In order to make comparisons of simulation run time meaningful, all of the simulations have been performed on the same hardware, a six-core single-CPU Intel Core i7-3930K@3.20 GHz, equipped with 32 GB of DDR3 1333 quad-channel RAM, with simulations making use of `parfor` parallel execution via the Matlab Parallel Toolbox when possible.

3.2.1. Interference-free

In the first step of verification of the L2S model, a single-cell scenario is considered. This case is equivalent to a throughput evaluation over an SNR range, and aims at reproducing a typical link level simulation. As in Section 3.2.2, results obtained with the Vienna LTE system level simulator [78], which implements the presented link abstraction model, are compared with link level results obtained with the Vienna LTE link level simulator [98].

In this scenario, we compare the throughput performance of different LTE transmission modes and antenna configurations over a range of SNRs, such as in [67, 99], performed both by means of link level simulations and system level simulations.

In LTE, the data subcarriers are recovered after a Fast Fourier Transform (FFT), discarding the adjacent guard band subcarriers, including any noise there. As the proportion of guard band subcarriers is not constant over the range of possible LTE bandwidths (see Table 2.3), employing a pre-FFT SNR would make the allocated bandwidth a parameter to take into account when comparing SNR results. Thus, the choice of employing a post-FFR SNR, denoted as $\gamma_{\text{post-FFT}}$, which directly refers to the SNR level of the data subcarriers (here denoted for a single subcarrier):

$$\gamma_{\text{post-FFT}} = \mathbb{E}\left\{ \frac{N_{\text{FFT}}}{N_{\text{tot}}} \frac{\mathbf{y}^{\text{H}}\mathbf{y}}{N_{\text{RX}}\sigma_n^2} \right\} = \frac{N_{\text{FFT}}}{N_{\text{tot}}} \frac{1}{\sigma_n^2}, \tag{3.24}$$

where N_{FFT} are the total number of LTE subcarriers (including bandguard), N_{tot} the number of data subcarriers, and σ_n^2 the mean noise power per receive antenna, and $\mathbf{y}$ the received signal, as in Equation (3.2).

In order to reproduce an SNR range with system level simulations, a single cell is placed, and a decreasing SNR value is accomplished by positioning the UE farther away from the cell center. Note that in the pathloss model, transmit power or noise spectral density values are actually irrelevant. Rather, it is the relation between the UE distance, which scales the received signal power, and the resulting SNR what is important, so as to be able to compare link and system level results with a common SNR definition.

Table 3.3 lists the employed configuration parameters, which result in the SNR distribution surrounding a single cell shown in Figure 3.15 (left). This setup consists of a single eNodeB with an omnidirectional antenna and depicts the SNR distribution, as defined in Equation (3.24), around the cell center. Being circularly-symmetric, it is thus possible to map the distance from the cell center to an SNR value, which is shown on Figure 3.15 (right).

The aforementioned scenario has been simulated at both link and system level by means of the Vienna LTE link level simulator [68, 98] and the Vienna LTE system

Table 3.3.: Simulation parameters employed for the validation of the L2S model in the single-cell, single-user scenario.

Frequency	2.14 GHz
Pathloss [dB]	$\max\left(10\log_{10}\left(\frac{4\pi\, d\, f}{c}\right)^3, 0\right)$
Bandwidth	1.4 MHz
TX power, antenna	5 W, omnidirectionally
Noise spectral density	-160 dBm/Hz
Channel model	ITU-R Pedestrian-A [97], block fading
Channel knowledge	Perfect
Feedback delay	none
Number of eNodeBs	1
Number of UEs	1

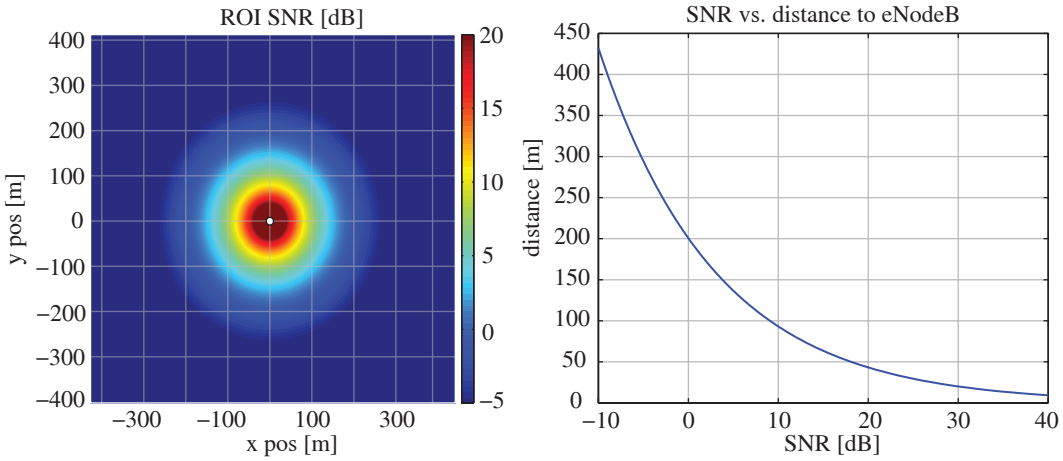

Figure 3.15: Left: SNR map over the simulated ROI (color scale limited to a [-5,20] dB SNR range). Right: Relation between the distance from the eNodeB site and the post-FFT SNR. Simulation parameters listed in Table 3.3.

level simulator [78], which implements the PHY layer abstraction models presented in Chapter 3. As performance measure, throughput has been chosen, as it is ultimately the metric of interest.

The following transmit modes defined in [39], as well as antenna configurations, have been evaluated, in all cases under a Ped-A channel at 5 km/h:

- Single transmit antenna (mode 1): 1×1 (SISO), 1×2 (SIMO).
- Transmit Diversity (mode 2): 2×2.
- Open Loop Spatial Multiplexing (mode 3): 2×2, 4×2, 4×4.
- Closed Loop Spatial Multiplexing (mode 4): 2×2, 4×2, 4×4.

For all of the listed configurations, link level and system level results are shown in Figures 3.16 and 3.17. For the SNR range between -10 and 40 dB, each plot

depicts throughput results for each of the four transmit modes considered: (i) single transmit antenna, (ii) TxD, (iii) OLSM, and (iv) CLSM. System level results (solid line) are plotted overlapped to link level ones (dashed line).

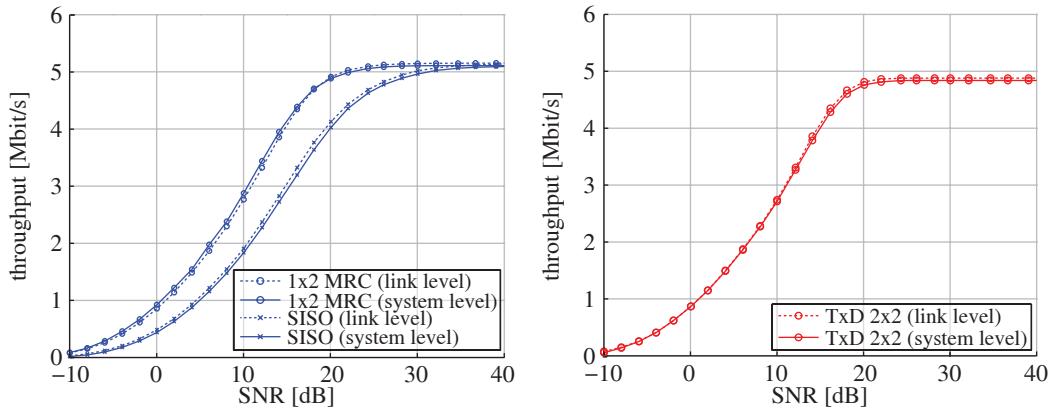

Figure 3.16: Link level and system level simulation results, single cell scenario. Left: Single antenna transmit mode (SISO and 1×2 with MRC). Right: TxD transmit mode (2×2).

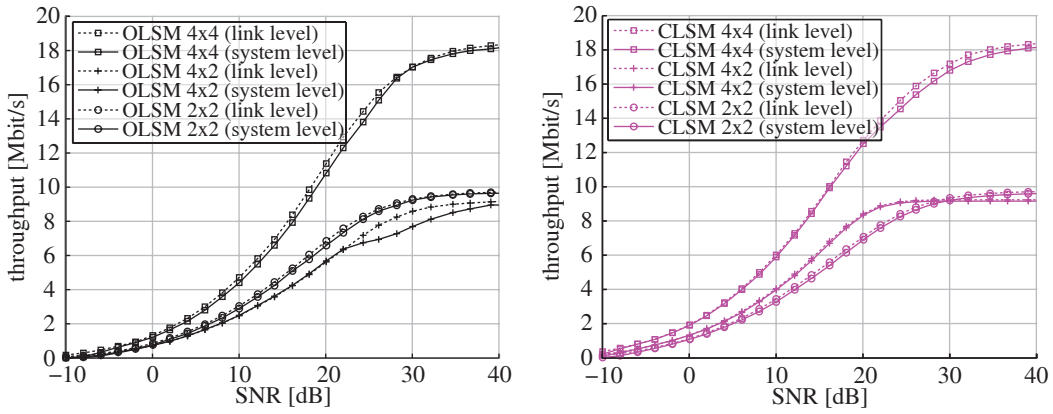

Figure 3.17: Link level and system level simulation results, single cell scenario. Left: OLSM transmit mode (2×2, 4×2, and 4×4). Right: CLSM transmit mode (2×2, 4×2, and 4×4).

As observed from the results in Figures 3.16 and 3.17, the results of the link abstraction model can be considered accurate with some deviation in the four-transmit antenna configuration of OLSM. As explained in Section 3.1.1.2, the block fading assumption is actually not valid for the OLSM case, but a reduced-complexity approximation is employed so as to still be able to calculate a single value per TTI. As expected, accuracy is highest for the two transmit antenna case, where only one precoder is employed. From the observed results, it is concluded that for the high SNR regime, the 4×2 OLSM link abstraction should not be employed, as significant deviations are present due to the inconsistency of the block fading assumption.

Of special interest is the feedback-wise more complex case of CLSM, where the optimum precoder is precalculated at trace generation and the optimum rank chosen at run time, for which the L2S model closely approximates link level results.

3.2.1.1. Complexity Evaluation

In this section, the run-time complexity of system level simulations is compared to that of link level simulations, showing a significant reduction in simulation run time when employing the L2S model. Hence, it validates the statement, much-emphasized in this thesis, that a link abstraction model allows for significantly faster simulation times compared to detailed link level simulations.

The same single-user, single-cell described above is simulated for the LTE channel bandwidths of 1.4, 3, 5, and 10 MHz (link and system level), and additionally for the 20 MHz bandwidth case for system level. As from the values, listed in Table 3.4, link level simulation run times scale linearly with the number of RBs, the link level simulation time for the 20 MHz case has been extrapolated from the existing values.

Table 3.4.: Simulation run time comparison in seconds. Marked in bold face are the system level simulation times, followed by the link level simulation times.

		1.4 MHz 6 RBs	3 MHz 15 RBs	5 MHz 25 RBs	10 MHz 50 RBs	20 MHz 100 RBs
Single TX	1×1	**28**/282	**28**/703	**28**/1 115	**28**/2 300	**30**/-
	1×2	**30**/278	**28**/666	**28**/1 089	**27**/2 248	**32**/-
TxD	2×2	**27**/614	**28**/1 542	**29**/2 552	**28**/5 086	**29**/-
OLSM	2×2	**32**/1 308	**33**/3 287	**34**/5 446	**39**/10 978	**33**/-
	4×2	**32**/1 426	**32**/3 842	**33**/6 598	**35**/15 040	**36**/-
	4×4	**33**/2 203	**37**/6 029	**36**/10 428	**40**/24 531	**44**/-
CLSM	2×2	**33**/358	**32**/901	**33**/1 509	**32**/3 399	**34**/-
	4×2	**31**/493	**35**/1 257	**34**/2 020	**33**/4 394	**34**/-
	4×4	**37**/874	**34**/2 310	**36**/3 563	**38**/7 535	**42**/-

The almost constant simulation run time of the system level simulator can be explained by the offloading of the most computationally-intensive task, which is the channel trace generation. Although a detailed complexity analysis of the system level simulator has not been performed, the shown simulation results indicate that, when simulating larger bandwidths, the complexity increase of the bandwidth-dependent part of the L2S model (in this scenario the link quality model and the CQI and, when applicable, RI feedback[7]) are almost negligible in comparison to the overall run time.

[7] In a single-user scenario, no actual scheduling is performed. However, scheduling algorithms do

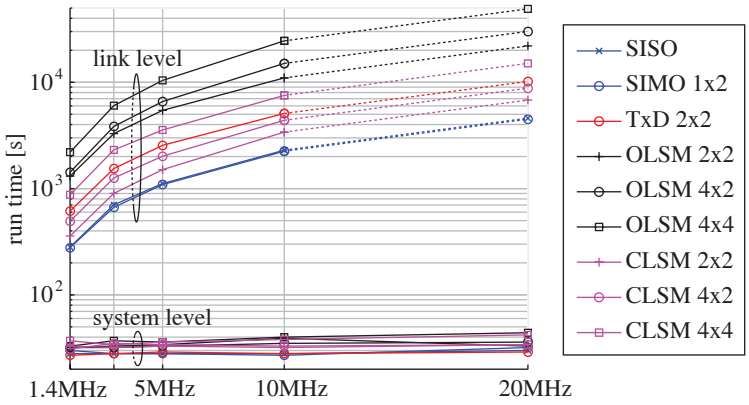

Figure 3.18: Simulation run time. Legend and colors as in Figures 3.16 and 3.17.

While for OLSM the gains are higher (up to a 1 150x speed-up, as shown in Table 3.5), significant gains can be achieved for CLSM, of high interest due to the employed more elaborate MIMO feedback and higher model accuracy. In this case, a speed-up gain of up to 359x can be obtained when considering a 20 MHz bandwidth. Such a computational complexity reduction enables performing multi-user simulations with high channel bandwidths, necessary to evaluate complex scheduling scenarios or multi-user gain with more practical simulation time durations, such as in the example in Appendix D.

Table 3.5.: Calculated system level simulator speed-up compared to link level simulation run time, 20 MHz bandwidth scenario.

	Single TX		TxD	OLSM			CLSM		
	1×1	1×2	2×2	2×2	4×2	4×4	2×2	4×2	4×4
speed-up	153x	140x	351x	665x	836x	1 150x	200x	259x	359x

3.2.2. Multi-cell

The L2S model presented in this thesis, on which the LTE system level simulator is based, enables simple simulation of dense networks. As such, it is an ideal tool for performance modeling of heterogeneous networks, where an LTE macrocell layer is coupled with a tier of smaller, low-power cells (e.g., pico-, or femto-cells). Although issues related to LTE femtocell deployment are currently already being investigated [100–102], results commonly lack accurate link abstraction modeling due to the extra overhead necessary for it.

increase in complexity with the number of PHY resources (RBs) they allocate. In multi-user simulations scenarios where scheduling algorithms are applied, simulation run time may not, depending on the complexity of the scheduling algorithm, stay constant over bandwidth.

As such, the scenario chosen for cross-comparison with link level results extends the scenario in Section 3.2.1 and depicts an interference situation inspired by a small-cell deployment. In this case, a pico- or femto-cell with low transmit power is deployed in a low-coverage zone [103], thus resulting in the situation depicted in Figure 3.19.

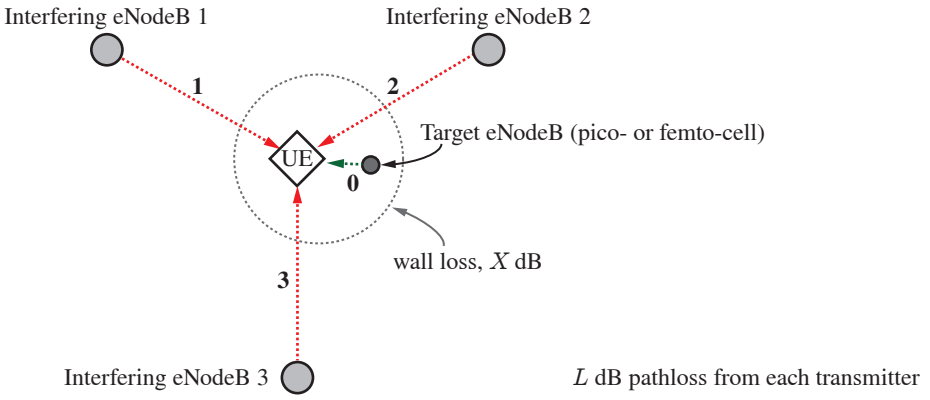

Figure 3.19: Multi-cell scenario link-and-system level simulation cross-comparison scenario. For cross-comparison, $\Delta_{P_{\mathrm{RX}}} = 15\,\mathrm{dB}$ and $\Delta_{P_{\mathrm{RX}}} = 20\,\mathrm{dB}$ have been employed.

The target UE is attached to this low-power cell which transmits with power P_{femto} with a pathloss L_{femto} to the UE. Equivalently, P_{macro} and L_{macro} characterize each of the interfering links. To characterize the different received power levels due to the difference in transmit power, pathloss, and wall loss in a femtocell deployment [104], an average receive power offset, denoted as $\Delta_{P_{\mathrm{RX}}}$ has been defined. Because of implementation limitations of the link level simulator, the same power offset for each of the interfering signals had to be chosen. Offset values of 15 dB and 20 dB have been employed, simulating a case where the same received power would be received with the addition of wall isolating the femtocell surroundings [104].

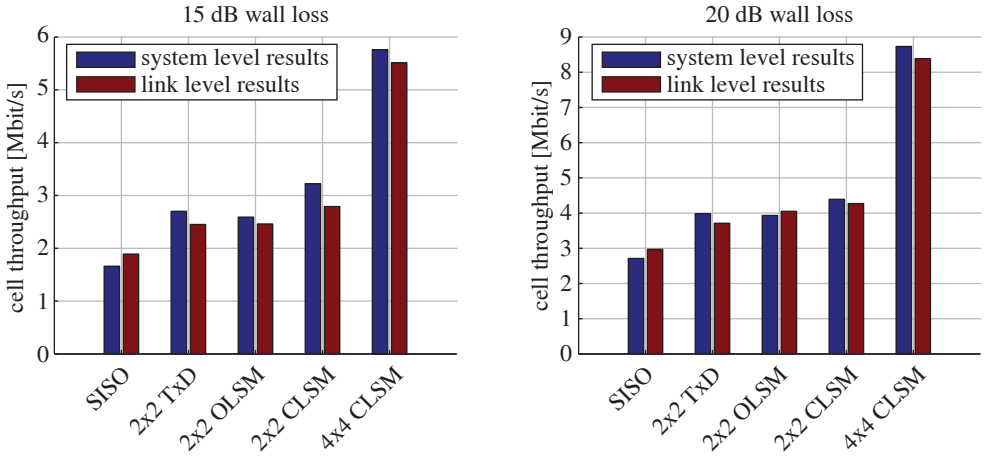

Figure 3.20: Multi-cell scenario throughput results. Left: 15 dB pathloss difference. Right: 20 dB pathloss difference. Blue: system level results, Red: link level results.

In Figure 3.19, the pathloss L dB from the attached eNodeB is shown green, while the pahtloss from the three interferers are marked red ($L + X$ dB pathloss). Thermal noise is considered negligible compared to the received interferer power and set accordingly in the link level simulator.

Figure 3.20 shows the throughput results for the described scenarios, both for system level (blue), and link level (red). With the addition of a power offset between the target eNodeB and the interferers, and the consideration of negligible thermal noise, the employed simulation parameters are analogous to those in Section 3.2.1. Relative throughput difference results compared to link level throughput results are listed in Table 3.6, for both the with 15 dB and 20 dB offset cases.

Table 3.6.: Relative throughput difference (compared to link level results).

	SISO	2×2 TxD	2×2 OLSM	2×2 CLSM	4×4 CLSM
15 dB offset	12.15%	10.20%	5.28%	15.41%	4.54%
20 dB offset	8.75%	7.28%	2.96%	2.81%	4.18%

3.2.3. Comparison with other MIMO LTE Link-to-system Model Results

Published throughput results of LTE MIMO L2S models such as those presented in this work, employed in a well-defined scenario and with a well-described set of simulation parameters are not easy to find. While some comparisons of results from different 3GPP member companies for simple 1×2 scenarios can be found in [105, 106], no analogous MIMO results could be found. Open source simulators such as [93, 95] could not be used because of their lack of detailed MIMO modeling.

Unfortunately, the only similar results found, to the author's knowledge, are those in [107], with which a throughput results comparison in shown in Figure 3.21.

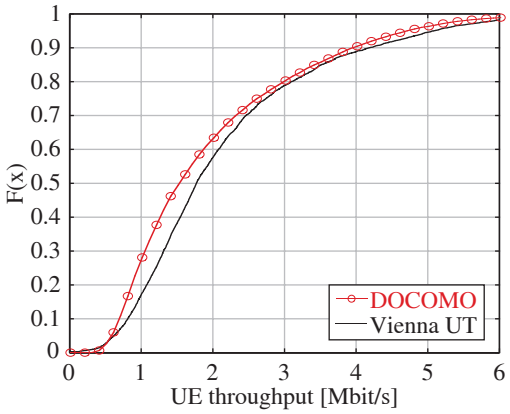

Figure 3.21: Throughput ecdf results on the scenario defined in [107]. Red line: results from [107]. Black line: results from the Vienna system level simulator.

The paper presents (among other results) LTE CLSM system level simulation results for an uncorrelated 4×2 antenna configuration in a well-defined scenario, described in Table 3.7.

Table 3.7.: Scenario parameters employed for comparison with the results in [107].

Carrier frequency	2 GHz
Channel bandwidth	10 MHz
Cell layout	Hexagonal grid, 19 sites, 3 cells/site
Antenna pattern	70 degree, 14 dBi
Inter-site distance	500 m
Transmission power	46 dBm
Pathloss	$128.1 + 37.6 \log_{10}(r)$
Penetration loss	20 dB
Shadow fading σ	8 dB
Shadow fading correlation	0.5 (inter-site), 1.0 (intra-site)
Channel model	ITU-T Typical Urban
Antenna configuration	4×2
Transmit mode	CLSM
Scheduling	Proportional Fair
UEs/cell	10

Deviations are actually expected, caused by differences in implementation of channel models, receiver models, link adaptation, and link-to-system interfaces [106]. Regrettably, an in-depth analysis of the causes of the deviations is not possible due to the closed nature of the tools employed to generate the results in [107]. However, when comparing the deviation between the two ecdf curves shown in Figure 3.21, we can state that the deviations is in the same order of magnitude as those accepted for use in LTE standardization for the Single-Input Multiple-Output (SIMO) case.

4. Extensions to the L2S Model

This chapter details extensions to include Hybrid Automatic Repeat reQuest (HARQ) and channel estimation errors, both aiming at more realistic modeling capabilities of LTE systems and extending the L2S model described in Chapter 3 beyond its basic capabilities.

These two extensions apply to different parts of the L2S model. The HARQ model applies to the link performance model, described in Section 3.1.2, while the channel estimation errors applies to the link quality model only, which is described in Section 3.1.1.

4.1. Hybrid ARQ

HARQ is part of the LTE MAC layer and provides retransmission capabilities aimed at improving link reliability. It consists of the retransmission of erroneously-received TBs and a joint decoding of the received retransmissions. It is implemented in the rate matching module, which also adjusts the rate matching target code rate, as mentioned in Section 2.2.3. The rate matching module is capable of, for a given target code rate, generating up to four versions of a TB. The different TB versions, indicated in the LTE standard by a *redundancy version index*, denoted as $\mathrm{rv}_{\mathrm{idx}}$ ($\mathrm{rv}_0, \ldots, \mathrm{rv}_3$), and when possible composed of a different subset of the original turbo-encoded bits, are combined at bit level and jointly decoded once received.

4.1.1. LTE HARQ

After turbo encoding (see Section 2.2.3), the rate-1/3-encoded bits, consisting of systematic and parity bits, are placed in a circular buffer, from which the bits for

each of the TB $\mathrm{rv}_{\mathrm{idx}}$ are extracted.

Given D original data bits, the rate matching process outputs a TB of size G bits, where $G > D$. After the rate 1/3 turbo code, the bits are placed on a circular buffer, with the systematic bits being placed consecutively and the parity bits interleaved one-to-one, as depicted in Figure 4.1.

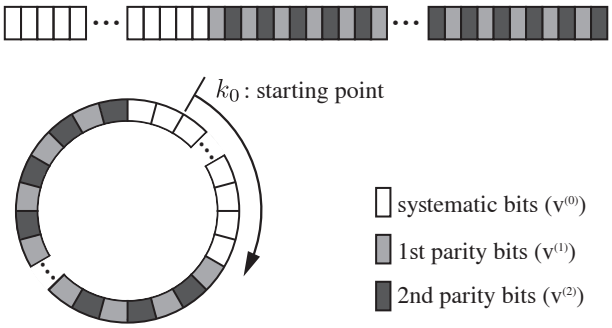

Figure 4.1: Positioning of the turbo-encoded bits (both systematic and parity) in the rate matching circular buffer. The output bits are obtained by setting a starting point k_0 and extracting G bits. The systematic bits are placed consecutively in the buffer, while the parity bits are interleaved.

In order to generate different TB versions for different values of $\mathrm{rv}_{\mathrm{idx}}$, a different starting point k_0, based on the value of $\mathrm{rv}_{\mathrm{idx}}$, is calculated for each retransmission.

Two modes of HARQ exist, which are depicted in Figure 4.2: in Chase Combining (CC) [108] (named after David Chase, its inventor), each retransmission is identical to the original transmission, while in Incremental Redundancy (IR) each retransmission consists of new redundancy bits from the channel encoder. With the aforementioned circular buffer setup, and assuming k_0 advances exactly $D/3$ positions for each retransmission, full IR is only possible if $G < \mathrm{rv}_{\mathrm{max}+1} \cdot D$.

In both cases, the received retransmissions are combined and the resulting packet is jointly decoded. LTE HARQ applies a hybrid CC/IR approach, in which a mixture of repeated and new bits are sent during the retransmissions, corresponding to the right figure in Figure 4.2.

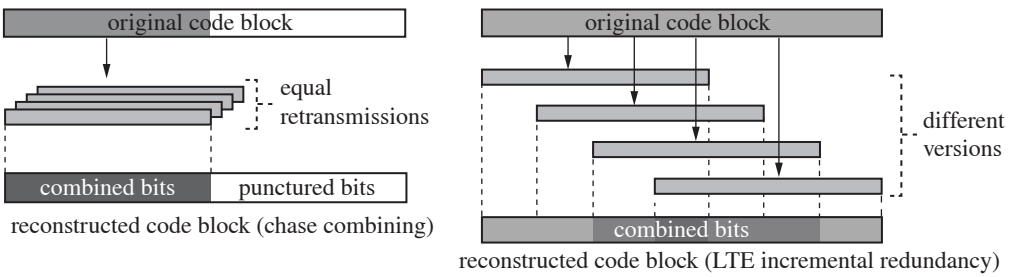

Figure 4.2: Chase combining (left) and the partial incremental redundancy (combining CC bits and IR bits) employed in LTE HARQ (right).

4.1.2. HARQ Modeling

In this section, the concepts presented in Section 3.1.2 for the calculation of the effective post-equalization SINR (γ_{eff}) are extended to the modeling of the combining gain due to the use of HARQ in constant channels. The model is based on a MI-based interpretation of HARQ combining and adapts the MIESM SINR averaging procedure to take into account the total MI of the combined TB [109].

As detailed in Section 4.1, the combined HARQ TB combines both repeated and newly-transmitted bits. This combining of new and repeated information can be expressed in terms of Accumulated Mutual Information (ACMI) [110, 111], which we denote as I_*.

In the CC case, as the same bits are retransmitted M times, it can be interpreted as an increase in the receive SNR. With every retransmission, energy is added, but no new information is sent. Thus, the CC ACMI of a set of M retransmissions sent over SNR γ, can be expressed as

$$I_*^{\text{CC}}(\gamma) = I_n\left(\sum_{m=0}^{M}\gamma\right), \tag{4.1}$$

where m denotes the m-th retransmission ($m = \{0, 1, \ldots, M\}$, with $m = 0$ corresponding to the initial transmission) and I_n denotes the BICM capacity for the employed MCS which n bits per symbol [72], shown in Equation (3.22).

For IR, if only new parity bits are sent in subsequent retransmissions, the result is an increase in the amount of information, thus increasing the ACMI such that

$$I_*^{\text{IR}}(\gamma) = \sum_{m=0}^{M} I_n(\gamma). \tag{4.2}$$

For the combined CC-IR HARQ scheme employed in LTE, we define $G_{\text{HARQ}} = (M+1)\,G$ as the total number of received bits after M retransmissions and separate into G_{CC} and G_{IR}, which represent the set of repeated and non-repeated bits, respectively, where $G_{\text{HARQ}} = G_{\text{CC}} + G_{\text{IR}}$. In this case, I_* results in a combination of Equations (4.1) and (4.2), which we denote as $I_*^{\text{LTE}}(\gamma)$:

$$I_*^{\text{LTE}}(\gamma) = \frac{G_{\text{IR}}}{n}\cdot I_n\left(\left(1+\frac{G_{\text{CC}}}{G_{\text{HARQ}}}\right)\cdot\gamma\right), \tag{4.3}$$

as G_{IR} unique bits are sent, repeated on average $\left(1+\frac{G_{\text{CC}}}{G_{\text{HARQ}}}\right)$ times.

4.1.3. Application to LTE

The LTE channel coding procedures (see Section 2.2.3) employ a turbo code of rate $r_c = 1/3$, followed by rate matching, which adjusts the output ECR (r_{eff}) to that of any of the defined MCSs (between 0.08 and 0.93, as listed in Table 2.5). The channel coding procedures for each of the (re)transmitted TBs is depicted in Figure 4.4.

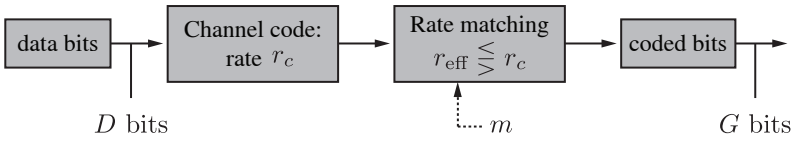

Figure 4.3: LTE rate matching procedure. The output of a turbo code of rate $r_c = 1/3$ is rate-matched in order to obtain the coded bits with the target rate r_{eff}. The retransmission index m, parametrizes exact bit subset of G.

To allow for an ACMI representation of the combined TB, the HARQ-combined TB is modeled as resulting from the combination of an inner code of rate r_m and an outer repetition code of rate $1/N_{\text{rep}}^m$, where r_m is in the range $1/3 \leq r_m \leq 1$ and the retransmission index m in the range $m = \{0, 1, 2, 3\}$. In this model, the output from the inner code represent the IR bits, while the outer repetition code represents the CC bits. The process is depicted in Figure 4.4.

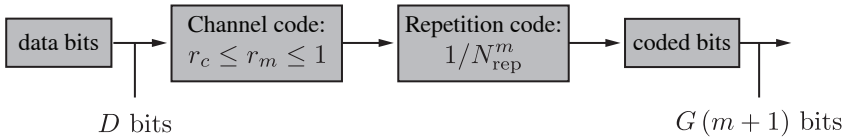

Figure 4.4: The combined TB is modeled as a combination of an inner channel code with a rate r_m between 1/3 and 1 (IR bits) and an outer repetition code of rate N_{rep}^m (CC bits).

If a capacity-approaching channel code with suitably long block length is used, it is well known that the BLER can be approximated by the MI outage probability [25, 112, 113]. In the case of a system with HARQ, equivalent expressions can be derived by using ACMI. Under this assumption, the outage probability ε is the probability $\mathbb{P}$ that $I_* < D$. Thus, for the case where the SNR γ is constant over the retransmissions, we obtain:

$$\varepsilon = \mathbb{P}\left[\frac{G_{\text{IR}}}{n} \cdot I_n\left(N_{\text{rep}}^m \cdot \gamma\right) < D\right]. \tag{4.4}$$

In order to extend the presented model for application to OFDM, MIESM is applied to compress the SINR vector $\boldsymbol{\gamma}$ into an AWGN-equivalent effective SINR value γ_{eff}, which can then be plugged into Equation (4.4).

To accomplish this, the subcarrier SINR vectors $\boldsymbol{\gamma}_{0,\ldots,M}$ of each (re)transmission are stacked into a vector $\boldsymbol{\gamma}$ of length $(M+1) \cdot N_{\mathrm{SCs}}$

$$\boldsymbol{\gamma} = \mathrm{vec}\left(\boldsymbol{\gamma}_0, \boldsymbol{\gamma}_1, \ldots \boldsymbol{\gamma}_M\right), \tag{4.5}$$

which is then compressed into an effective SNR value γ_{eff} by means of MIESM:

$$\gamma_{\mathrm{eff}}\left(\boldsymbol{\gamma}\right) = I_n^{-1}\left(\frac{1}{(M+1)\,N_{\mathrm{SCs}}} \sum_i I_n\left(\boldsymbol{\gamma}_i\right)\right), \tag{4.6}$$

where, N_{SCs} is the total number of subcarriers. Adapting Equation (4.4), the outage probability ε can be calculated as:

$$\varepsilon = \mathbb{P}\left[\frac{G_{\mathrm{IR}}}{n} \cdot I_n \underbrace{\left(N_{\mathrm{rep}}^m \cdot \gamma_{\mathrm{eff}}\left(\boldsymbol{\gamma}\right)\right)}_{\gamma_{\mathrm{AWGN}}} < D\right], \tag{4.7}$$

where γ_{AWGN} is denoted as the AWGN-equivalent SINR of the combined TB including the repetition gain.

In order to consider the non-ideal behaviour of the channel coding and the loss in performance due to the rate matching process, AWGN BLER curves are employed instead of the outage probability. Thus, ε is approximated as:

$$\varepsilon \approx \mathrm{BLER}_{\mathrm{AWGN}}\left(r_m, n, \gamma_{\mathrm{AWGN}}\right). \tag{4.8}$$

In LTE, the values for r_m cannot simply be obtained from the final code rate applied by the rate matching [45]. However, by using the implementation of the rate matcher in [98], the equivalent puncturing matrices applied to the mother code of rate $r_c = 1/3$ can be extracted and employed to obtain the outer turbo coding rate r_m and the inner repetition coding rate $1/N_{\mathrm{rep}}^m$ for each of the HARQ retransmission index and MCS value pairs.

For each MCS and retransmission index m, the obtained effective turbo code rates (r_m) and repetition rates (N_{rep}^m) are shown in Figure 4.5. The r_m code rates required for each of the modulations defined for the LTE data channel are listed in Table 4.1.

Model accuracy is evaluated by means of link level simulations with the Vienna LTE simulator [98] for both AWGN and time-correlated ITU Pedestrian-B channels [114–116].

For each of the 15 LTE MCSs, the BLER curves from the simulation and from the proposed model are compared at the 10% BLER point, which is known to lead to near-optimal performance [113] and is thus also the target BLER for link adaptation.

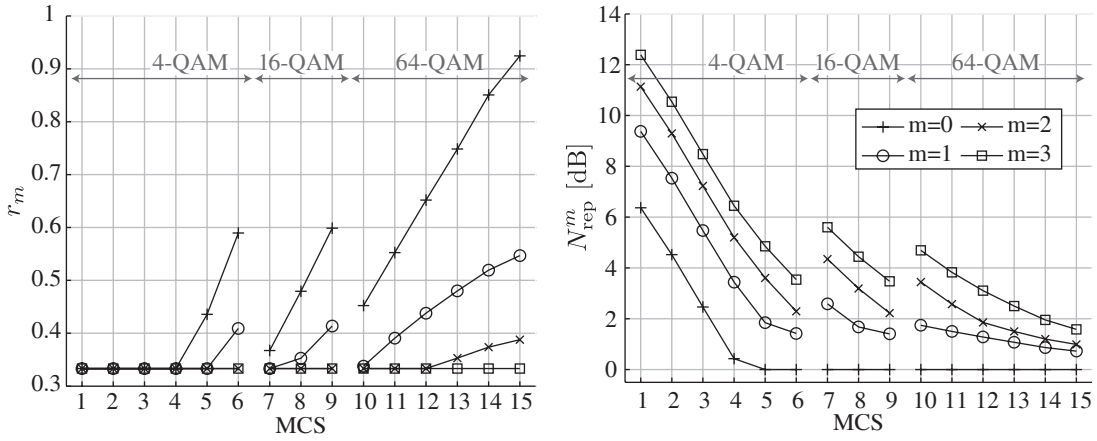

Figure 4.5: Inner (r_m) and outer (N_{rep}^m) code rates for HARQ modeling.

Table 4.1.: Turbo code code rates (r_m) for HARQ modeling.

Modulation	Total	r_m
4-QAM	4	1/1.70, 1/2.29, 1/2.44, 1/3.00
16-QAM	6	1/1.67, 1/2.09, 1/2.42, 1/2.72, 1/2.83, 1/3.00
64-QAM	16	1/1.08, 1/1.18, 1/1.34, 1/1.53, 1/1.81, 1/1.83, 1/1.93, 1/2.08, 1/2.21, 1/2.28, 1/2.56, 1/2.58, 1/2.68, 1/2.83, 1/2.96, 1/3.00
	26	

Figure 4.6 shows, for MCS 6, a BLER comparison after each retransmission and the coding/repetition gain (10% BLER points marked). It is seen that most of the coding gain is always concentrated on the first retransmissions, while for retransmission indexes higher than rv_1, almost no r_c-encoded bits remain to be transmitted. while with a repetition code, a gain of 3 dB would be obtained, due to the coding gain of the IR bits, a higher 5.7 dB gain is obtained.

As new r_c-encoded bits become depleted, r_m converges to $r_c = 1/3$, as observed on the second and third retransmissions.

The accuracy of the model is evaluated, for each MCS, in terms of the deviation of the simulated and modeled 10 % BLER points. It is evaluated for AWGN and ITU Pedestrian-B channels and is depicted in Figure 4.7. Alternatively, Table 4.2 lists the average deviation in dB obtained for each retransmission index and MCS, grouped by modulation alphabet.

Focusing on the more realistic frequency selective case, it is observed that except for the case of 64-QAM and $\text{rv}_{\text{idx}} > 2$, the predicted BLER values show an average deviation lower than 0.4 dB. However, as in the case of the precoder precalculation shown in Appendix A, what is important is an analysis of the relevance of the

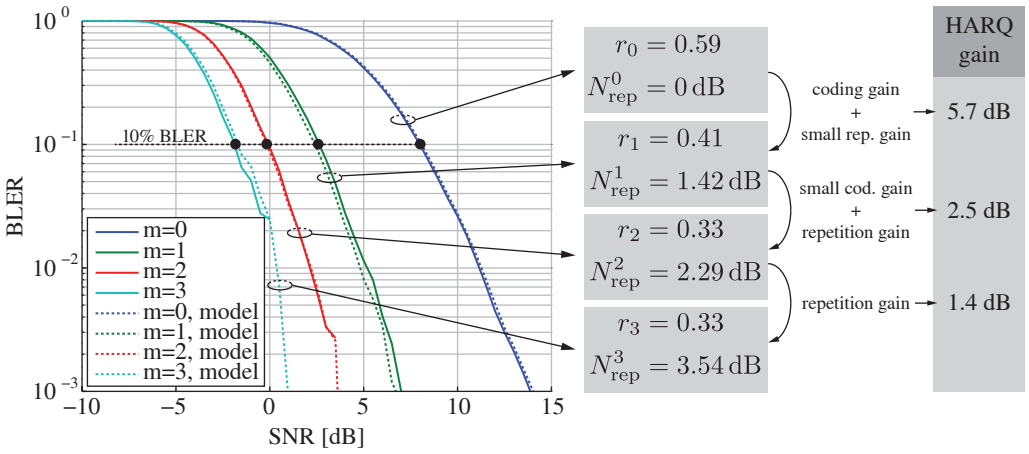

Figure 4.6: MCS 6 BLER, ITU Pedestrian-B 5 km/h. Solid line: simulation, Dashed line: model. Marked: BLER=10% points.

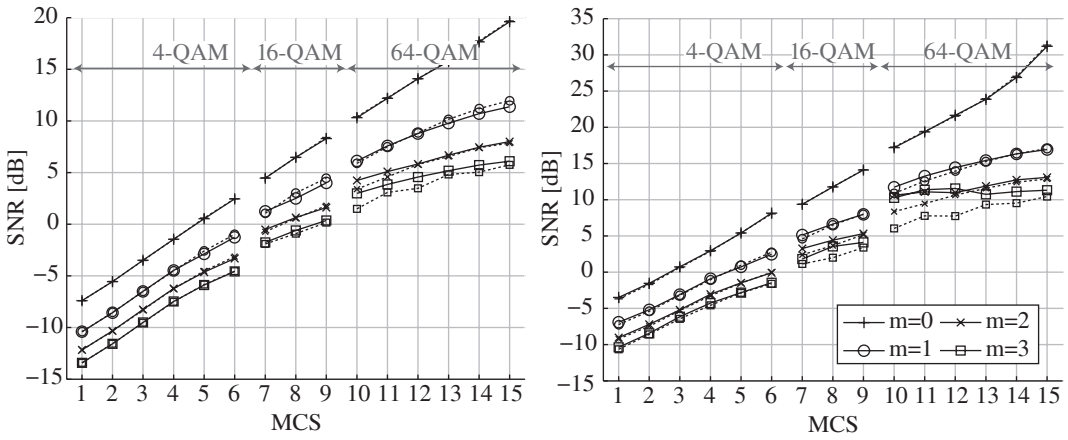

Figure 4.7: Model accuracy for the BLER=10% points, $m = \{0, 1, 2, 3\}$. Solid line: model, Dashed line: simulations results. Left: AWGN results. Right: ITU Ped-B 5 km/h results.

inaccuracies in those specific ill-conditioned cases.

An analysis of the distribution of the HARQ gain between each retransmission, measured at the BLER=10 % point and detailed in Table 4.3, shows that: (i) effectively, most of the gain occurs during the first retransmissions (ii) for higher MCSs, a higher coding gain further increases the overall HARQ gain of the first retransmission.

The existence of a second retransmission implies that the MI gain of the first retransmission was not high enough to correctly receive the TB. In the low MCS set (1-6, employing 4-QAM modulation), the first retransmission introduces a gain between 3.56 dB and 5.3 dB. However, the same retransmission number translates into an average gain between 6.38 dB and 14.28 dB.

Assuming a correctly-functioning channel quality feedback and AMC algorithm, as

Table 4.2.: Average deviation of the modeled 10% BLER points [dB].

m	AWGN				Ped-B			
	0	1	2	3	0	1	2	3
4-QAM	0.02	0.11	0.06	0.03	0.11	0.22	0.14	0.20
16-QAM	0.04	0.40	0.16	0.22	0.02	0.23	0.58	0.98
64-QAM	0.07	0.30	0.29	0.79	0.11	0.39	0.85	2.59

well as the coherence time assumptions in Section 3.1.1, the impact of the model inaccuracies at high MCS and retransmission count is significantly reduced due to the improbability of such retransmissions. This assumption is also backed by the results in [109], in which it is shown that, for a MIMO cell setup such as that shown in Figure 3.7, 64-QAM retransmissions account for less than 0.05% of the total number of TBs[1].

Table 4.3.: Minimum and maximum SNR gain due to the m-th HARQ retransmission with respect to the previous retransmission for each of the employed modulations. ITU Pedestrian-B channel (5 km/h).

	4-QAM	16-QAM	64-QAM
1st re-tx	3.56 dB - 5.3 dB	4.79 dB - 6.13 dB	6.38 dB - 14.28 dB
2nd re-tx	1.98 dB - 2.77 dB	2.19 dB - 2.85 dB	2.53 dB - 4.19 dB
3rd re-tx	1.11 dB - 1.6 dB	1.27 dB - 1.78 dB	1.68 dB - 2.89 dB

4.2. Channel Estimation Error

This section extends the ZF-receiver-based post-equalization SINR to the case of imperfect channel knowledge, adding to the model detailed in Section 3.1.1.1 [117]. Analogously to Equation (3.8), the post-equalization SINR for the i-th layer, denoted as γ_i, is expressed as

$$\gamma_i = \frac{P_{\mathrm{TX}}}{[\mathrm{MSE}]_{ii}}, \tag{4.9}$$

where P_{TX} denotes the signal sum power sent over the transmit antennas, denoted as $\sigma_{x_0}^2$ in the remaining expressions in this chapter for mathematical consistency with the transmitted symbol vector $\mathbf{x}$, MSE the $\mathbb{R}^{\nu\times\nu}$ Mean Square Error (MSE) matrix, and $[\cdot]_{ii}$ the i-th element of the matrix diagonal.

[1] In CLSM/OLSM, the level of spatial multiplexing can be adjusted, in addition to the MCS. As in SISO, varying the MCS is the only available rate-adjusting mechanism, the ratio would be higher for SISO transmissions, but nevertheless of minor impact.

The MSE is calculated based on the actual transmitted signal ($\mathbf{x}_0$) and the estimated receive symbols ($\hat{\mathbf{x}}_0$) as

$$\mathrm{MSE} = \mathbb{E}\Big\{ \left(\hat{\mathbf{x}}_0 - \mathbf{x}_0\right) \left(\hat{\mathbf{x}}_0 - \mathbf{x}_0\right)^{\mathrm{H}} \Big\}, \tag{4.10}$$

The estimated receive symbol vector $\hat{\mathbf{x}}_0$ is, as previously shown in Equation (3.5), obtained as

$$\hat{\mathbf{x}}_0 = \mathbf{G}\mathbf{y} = \mathbf{G}\left(\mathbf{H}_0\mathbf{x}_0 + \mathbf{n} + \sum_{i=1}^{N_{\mathrm{int}}} \mathbf{H}_i\mathbf{x}_i \right), \tag{4.11}$$

where the ZF receive filter $\mathbf{G}$ is calculated as

$$\mathbf{G} = \left(\hat{\mathbf{H}}_0^{\mathrm{H}} \hat{\mathbf{H}}_0 \right)^{-1} \hat{\mathbf{H}}_0^{\mathrm{H}}, \tag{4.12}$$

$$\hat{\mathbf{H}}_0 = \mathbf{H}_0 + \mathbf{E}, \tag{4.13}$$

$$e_{ij} \sim \mathcal{CN}\left(0, \sigma_e^2\right). \tag{4.14}$$

The estimated channel ($\hat{\mathbf{H}}_0$) is modeled as the actual channel plus an error matrix $\mathbf{E}$ whose entries (e_{ij}) are modeled as complex-normal with mean power σ_e^2 [118].

Applying a Taylor series expansion at $\mathbf{E} = \mathbf{0}$, i.e., assuming a small channel estimation noise variance σ_e^2 [119], the following MSE expression is obtained:

$$\begin{aligned}
\mathrm{MSE} &= \mathbb{E}\left\{ \left(\hat{\mathbf{x}}_0 - \mathbf{x}_0\right) \left(\hat{\mathbf{x}}_0 - \mathbf{x}_0\right)^{\mathrm{H}} \right\} \\
&\approx \tilde{\mathbf{H}}_{\mathbf{0}}^{-1} \mathbb{E}\Big\{ \mathbf{E}\mathbf{W}_0\mathbf{x}_0\mathbf{x}_0^{\mathrm{H}}\mathbf{W}_0^{\mathrm{H}}\mathbf{E}^{\mathrm{H}} \Big\} \left(\tilde{\mathbf{H}}_0^{-1} \right)^{\mathrm{H}} \\
&\quad + \tilde{\mathbf{H}}_{\mathbf{0}}^{-1} \mathbb{E}\Big\{ \mathbf{n}\mathbf{n}^{\mathrm{H}} \Big\} \left(\tilde{\mathbf{H}}_0^{-1} \right)^{\mathrm{H}} + \tilde{\mathbf{H}}_0^{-1} \mathbb{E}\Big\{ \mathbf{E}\mathbf{W}_0 \tilde{\mathbf{H}}_{\mathbf{0}}^{-1} \mathbf{n}\mathbf{n}^{\mathrm{H}} \left(\tilde{\mathbf{H}}_{\mathbf{0}}^{-1} \right)^{\mathrm{H}} \mathbf{W}_0^{\mathrm{H}}\mathbf{E}^{\mathrm{H}} \Big\} \left(\tilde{\mathbf{H}}_{\mathbf{0}}^{-1} \right)^{\mathrm{H}} \\
&\quad + \sum_{i=0}^{N_{\mathrm{int}}} \Bigg[\tilde{\mathbf{H}}_{\mathbf{0}}^{-1} \mathbb{E}\Big\{ \tilde{\mathbf{H}}_{\mathbf{i}} \mathbf{x}_i \mathbf{x}_i^{\mathrm{H}} \tilde{\mathbf{H}}_{\mathbf{i}}^{\mathrm{H}} \Big\} \left(\tilde{\mathbf{H}}_{\mathbf{0}}^{-1} \right)^{\mathrm{H}} \\
&\quad + \tilde{\mathbf{H}}_{\mathbf{0}}^{-1} \mathbb{E}\Big\{ \mathbf{E}\mathbf{W}_0 \tilde{\mathbf{H}}_{\mathbf{0}}^{-1} \tilde{\mathbf{H}}_{\mathbf{i}} \mathbf{x}_{\mathbf{i}} \mathbf{x}_{\mathbf{i}}^{\mathrm{H}} \tilde{\mathbf{H}}_{\mathbf{i}}^{\mathrm{H}} \left(\tilde{\mathbf{H}}_{\mathbf{0}}^{-1} \right)^{\mathrm{H}} \mathbf{W}^{\mathrm{H}}\mathbf{E}^{\mathrm{H}} \Big\} \left(\tilde{\mathbf{H}}_{\mathbf{0}}^{-1} \right)^{\mathrm{H}} \Bigg] \\
&= \left(\sigma_e^2\sigma_{x_0}^2 + \sigma_v^2 + \sigma_v^2\sigma_e^2 \mathrm{Tr}\left(\left(\mathbf{H}_0^{\mathrm{H}}\mathbf{H}_0 \right)^{-1} \right) \right) \left(\tilde{\mathbf{H}}_0^{\mathrm{H}} \tilde{\mathbf{H}}_0 \right)^{-1} \\
&\quad + \sum_{i=1}^{I} \left[\tilde{\mathbf{H}}_0^{-1} \left(\sigma_{x_i}^2 \mathbf{H}_i \mathbf{W}_i \mathbf{W}_i^{\mathrm{H}} \mathbf{H}_i^{\mathrm{H}} + \sigma_{x_i}^2 \sigma_e^2 \mathrm{Tr}\left(\mathbf{H}_i \mathbf{H}_i^{\mathrm{H}} \left(\mathbf{H}_0^{\mathrm{H}}\mathbf{H}_0 \right)^{-1} \right) \left(\tilde{\mathbf{H}}_0^{-1} \right)^{\mathrm{H}} \right) \right],
\end{aligned} \tag{4.15}$$

where $\mathbf{H}$ denotes the channel matrix, $\tilde{\mathbf{H}}$ the effective channel matrix (i.e., the precoder-and-channel-matrix combination $\mathbf{HW}$), and $\mathbf{E}$ the channel estimation error matrix. The full derivation of Equation (4.15) can be found in Appendix C.

The expression can be simplified by omitting the Tr () term [118], obtaining

$$\mathrm{MSE} = \left(\sigma_e^2\sigma_{x_0}^2 + \sigma_v^2\right)\left(\tilde{\mathbf{H}}_0^{\mathrm{H}}\tilde{\mathbf{H}}_0\right)^{-1} \tag{4.16}$$

$$+\sum_{i=1}^{N_{\mathrm{int}}}\left[\tilde{\mathbf{H}}_0^{-1}\left(\sigma_{x_i}^2\mathbf{H}_i\mathbf{W}_i\mathbf{W}_i^{\mathrm{H}}\mathbf{H}_i^{\mathrm{H}}\right)\left(\tilde{\mathbf{H}}_0^{-1}\right)^{\mathrm{H}}\right], \tag{4.17}$$

where, assuming all of the entries of $\mathbf{H}_i$ to have an average power of one, σ_{x_i} is the average receive power over all antennas for the i-th user (i.e., the transmit power divided by the pathloss).

For the purpose of model validation, a fixed value for σ_e^2 could be used. This setting would, however, not be realistic. As the quality of the channel estimation varies with the quality of the pilot symbols from which the estimation is achieved, it is therefore a function of the signal level of the pilots. Adapting from [120], we express the channel estimation error σ_e^2 as:

$$\sigma_e^2 = \frac{c_e}{\sigma_{x_0}^2}\left(\sigma_n^2 + \sum_{i=1}^{N_{\mathrm{int}}}\sigma_{x_i}^2\right), \tag{4.18}$$

where a typical value for c_e would be 0.0544 [120, 121][2].

4.2.1. Model Accuracy

The model is validated in two scenarios: (i) over a SNR range, where no interferers are present and the noise level is varied and (ii) with six interferers placed on a hexagonal grid layout with omnidirectional antennas and evaluating the results on the points corresponding to the center cell, so as to avoid border map artifacts.

In both cases, the model is validated for 2×2 and 4×4 antenna configurations employing CLSM and the standard-defined precoding codebook [39]. The model is validated for all the possible number of spatial layers for each antenna configuration, which comprise $\nu = \{1, 2\}$ for the 2×2 case and $\nu = \{1, 2, 3, 4\}$ for the 4×4 case. As the switching between number of layers RI needs to be performed at run-time, it is not in the scope of validating the accuracy of the model to show the combined performance when dynamically changing the number of employed layers rather than to evaluate whether the prediction for any possible rank choice, whichever that one may be, is accurate.

In both cases, the channel matrix is obtained from an implementation of the Winner Phase II channel model [122], and the precoding matrix chosen so as to maximize

[2] Assumes a pedestrian simulation and an LMMSE channel estimator.

the achievable capacity [54]. Since no interference coordination is assumed, each interferer is assigned a random precoder from the codebook.

As accuracy metric, the post-equalization SINR output by the model and that of a simulated transmission are compared in the capacity domain, where the capacity metric is expressed as the sum capacity over all streams and calculated as

$$C_{\text{sum}} = \sum_{i=1}^{\nu} \log_2 (1 + \gamma_{\text{i}}) \,. \tag{4.19}$$

Figure 4.8 shows the results for the no-interference scenario for the 2×2 and 4×4 antenna configuration cases respectively, with $c_e = 0.0544$ [120].

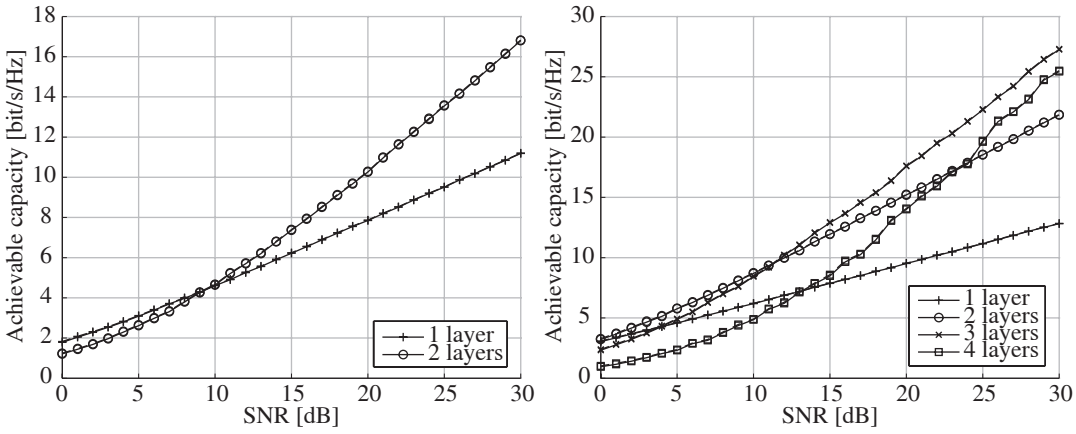

Figure 4.8: 2 × 2 (left) and 4 × 4 (right) results. Solid line: modeled achievable capacity. Dashed line (totally overlapped by the solid line): calculated achievable capacity.

This scenario, although at first glance suitable, is unable to depict the capacity deviation between the predicted and the obtained value from the simulation. As σ_e^2 is a linear function of σ_n^2, the result is the channel estimation error is effectively always 12 dB below the noise level, its influence in the MSE being thus negligible.

Table 4.4.: Simulation parameters: model validation for the interference case.

Inter-eNodeB distance	500 m
Bandwidth	15 kHz (single subcarrier)
Transmit power (P_{TX}):	17.7 dBm (43 dBm/5 MHz)
Noise density	-173 dBm/Hz
Channel model	Winner Phase II [76, 122]
Pathloss	$L = 128.1 + 37.6 \log_{10}(R)$ [69]
Transmit mode:	CLSM
Antenna type	Omnidirectional, 0 dB gain
Minimum coupling loss	70 dB [69]
Number of points in the target sector	8 658

In the next scenario, a simple hexagonal deployment of eNodeBs with omnidirectional antennas has been employed. Although not representing a more complex tri-sector cell layout such as in [69], it still validates whether the SINR model is capable of predicting the average achievable capacity in an interference-limited scenario. The simulation parameters used in this simulation set are listed in Table 4.4. As SINR averaging is handled by the link performance model, simulation results for a single-carrier setup are sufficient and reduce simulation time.

Figure 4.9 depicts for the simulated area the wideband, denoted as SINR $\Gamma(x, y)$, and resulting from the simulation parameters listed in Table 4.4. For each point (x, y) of the ROI, the wideband SINR corresponding to the closest cell SINR-wise, denoted as the i-th cell, is depicted.

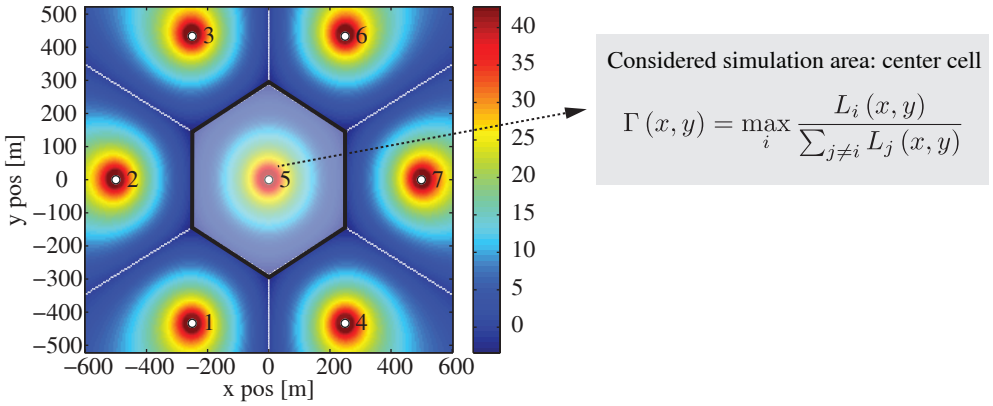

Figure 4.9: Network layout used for the multi-cell simulation. The center highlighted area shows the points taken into account for the simulation.

Figure 4.10 show the results of the accuracy of the model for the 2×2 and 4×4 antenna configuration cases, respectively.

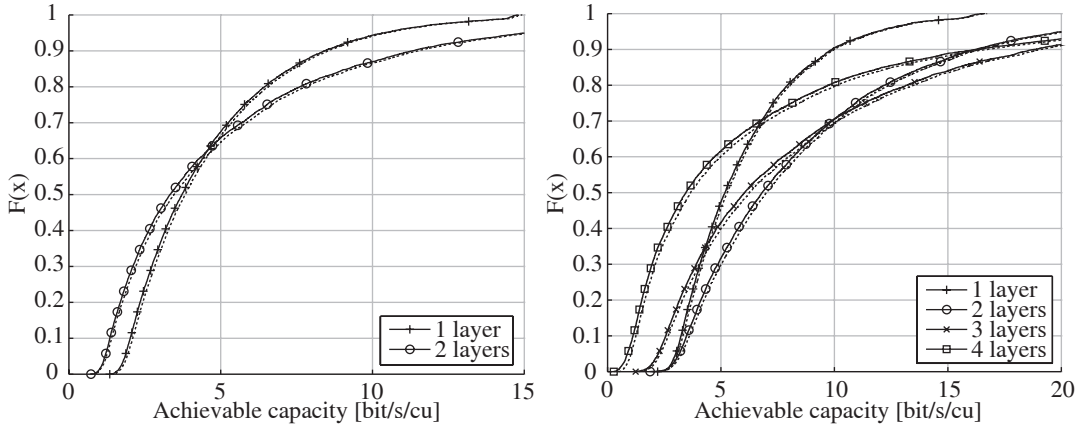

Figure 4.10: Achievable capacity results for the 2×2 (left) and 4×4 (right) antenna configurations. Solid line: modeled achievable capacity. Dashed line: calculated achievable capacity.

In this case, and as opposed to the results in Figure 4.8, σ_e^2 is is also influenced by the interfering cells, such that $\sigma_e^2 = \frac{c_e}{\sigma_{x_0}^2}\left(\sigma_n^2 + \sum_{i=1}^{N_{\text{int}}} \sigma_{x_i}^2\right)$. Thus, more realistically modeling the distribution of σ_e^2 to that of a cellular network layout.

The results depicted on Figure 4.10 show the ecdf of the achievable rate empirical over the cell area depicted in Figure 4.9. Results are shown for the 2×2 (left) and 4×4 (right) antenna configurations and for each case for all of the layer (RI) possibilities.

Since the model is based on a Taylor approximation at $\mathbf{E} = \mathbf{0}$, it is expected to be less accurate the higher σ_e^2 is, as visible in Figure 4.10, where, specially for the four-layer 4×4 case, the model is pessimistic compared to the expected result due to the application of the Taylor approximation, although still retaining a good level of accuracy.

5. Performance Evaluation of Fractional Frequency Reuse in LTE

Fractional Frequency Reuse (FFR) has been investigated as a method to combine the peak spectral efficiency of a reuse-1 scheme and the edge spectral efficiency performance of higher-order frequency reuse schemes [123] by simultaneously employing different reuse factors within a cell. Ultimately, FFR aims at improving cell edge performance when compared to a reuse-1 scheme while maintaining cell center performance. Although LTE is a reuse-1 scheme, the use of OFDMA as the PHY layer in the standard enables easy implementation of frequency partitioning schemes such as FFR.

FFR performance is typically assessed in literature [124–131] by means of three Key Performance Indicators (KPIs) derived from the throughput ecdf. These are (i) mean throughput, (ii) edge throughput, and (iii) peak throughput. Here, the terms "peak" and "edge" refer, as widely employed in literature, to the the 95% and 5% points of the UE throughput ecdf. These can be interpreted as the performance of an UE at the cell center and at cell edge, respectively.

Over the course of this chapter, an analysis of the achievable throughput improvement of applying FFR to LTE is performed and, based on the results, argued that the mean, edge, and peak throughput KPIs need to be combined with a fairness measure [57] to suitably be able to quantify the trade-off between reuse-1 and the higher-order reuse in FFR.

5.1. Principles of Fractional Frequency Reuse

FFR is based on dividing the cell into a center part, where interference is lower and reuse-1 is employed, and an outer part, where a higher frequency reuse factor is employed (typically a reuse factor of three). This accomplishes an improvement of the SINR at cell edge, while still allowing the UEs placed at the cell center to use the whole bandwidth.

In this chapter, the assumed FFR scheme is the most commonly found scheme in literature, which combines a reuse-1 center zone, denoted as the Full Reuse (FR) zone, and an outer zone employing reuse-3, denoted as the Partial Reuse (PR) zone. As shown on Figure 5.1 (from left to right): (i) the cells are divided into a center FR and an edge PR zone. In the PR zones, three frequency bands are cyclically allocated (reuse-3), while in the FR zones, the same frequency is reused. (ii) A fraction β_{FR} of the total bandwidth is allocated to the frequency band employed in the FR zones. The remaining bandwidth (a fraction of $1-\beta_{\mathrm{FR}}$ of the total) is equally allocated to each of the three PR bands. i.e., $(1-\beta_{\mathrm{FR}})/3$ to be assigned to each PR zone.

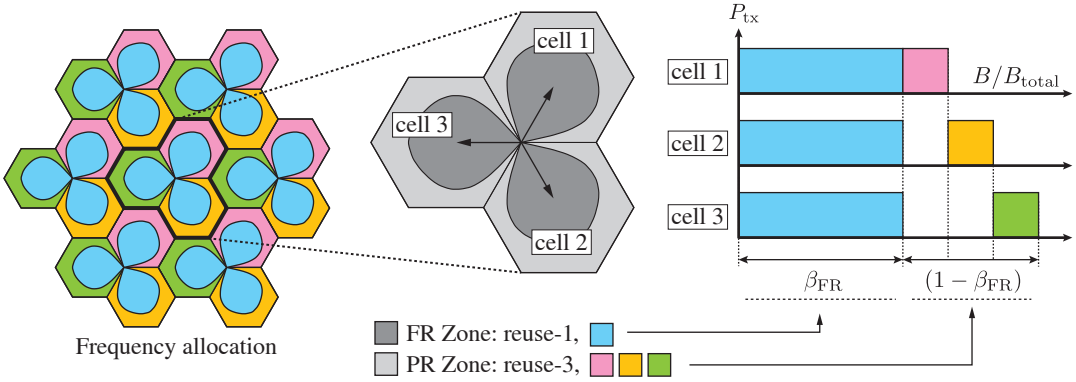

Figure 5.1: Principles of FFR. Left: frequency allocation over the cells. Middle: separation of the cell into a Full Reuse (FR) and a PR zone, employing reuse-1 and reuse-3, respectively. Right: bandwidth allocation of the frequency bands employed.

Thus, two parameters configure the allocation of the PHY resources to the FR/PR zones: (i) the distribution of the bandwidth, and (ii) the cell area allocated to each zone. The first parameter is defined by the bandwidth partitioning factor β_{FR}, as shown in Figure 5.1. For the division of the cell area among the FR and PR zones, some prior work has proposed a distance-based metric [132]. However, such a metric is only meaningful for a circularly-symmetric case, and not applicable for the more realistic sectorized case. Thus, in this case, the employed metric for dividing the cell into the FR and PR zones is that of an SINR threshold, denoted as Γ_{thr}, which is further explained in Section 5.2.

This work assumes a hexagonal grid of sites with three cells per site, with a constant number of UEs per cell and a full-buffer traffic model assumption. This results in a cell layout such as that in the example in Figure 5.1, where each cell contains a center area employing reuse-1 and an outer area employing reuse-3.

5.2. Previous Work

While capacity is commonly employed to determine the switching point between the FR and PR zones (simplified into a distance metric for circularly symmetric cases and a SINR threshold for sectorized cases), such a capacity-based approach does not take into account the presence of multiple UEs and is thus incomplete [133].

With the premise that a UE should be assigned to the FR or PR zone so as to maximize its throughput, and that the PHY resources are shared among all UEs in a cell, capacity density (analogous to UE throughput through the assumption of a uniform UE density over the cell area) was initially employed to evaluate the potential benefits of FFR.

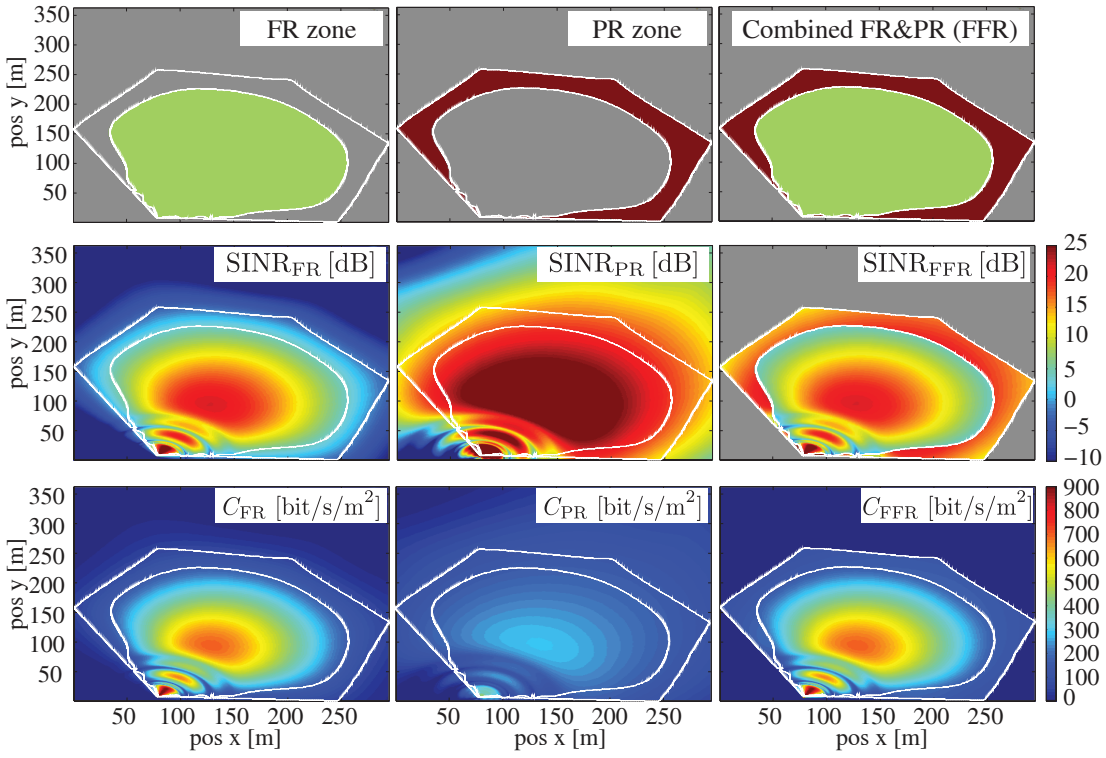

Figure 5.2: Capacity density-based FFR results for $\beta_{FR} = 0.75$ and $\Gamma_{thr} = 3.20\,dB$. The cell area combines a reuse-1 zone (marked green) with a reuse-3 area (marked red). The FR and PR areas of the cell are depicted in terms of SINR (center row) and capacity density (bottom row). Column-wise, the spatial distribution is shown for the FR zone (left), the PR zone (middle), and combined (right). FR and PR zone boundaries are marked with dashed lines.

Figure 5.2 shows example results for the FFR configuration employing $\beta_{\mathrm{FR}} = 0.75$ and $\Gamma_{\mathrm{thr}} = 3.20\,\mathrm{dB}$ FFR configuration. As presented in [133], this configuration was found to maximize capacity density and resulted in an improvement compared to the reuse-1 case of: 8.68 % in terms of average performance, 61.81 % in edge capacity density, and 5.21 % in peak capacity density. As the focus of this thesis is on L2S modeling, the details on the previous work regarding the optimization of capacity density have been excluded from this chapter. However, the obtained results, which employ a β_{FR}-dependent SINR threshold, are shown in Figure 5.3.

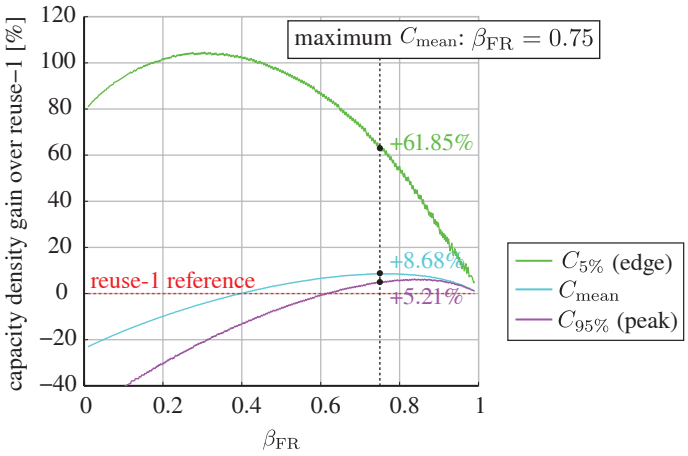

Figure 5.3: FFR mean, edge, and peak capacity density gains relative to reuse-1 [133].

As seen in Figure 5.3, FFR can potentially be employed to simultaneously boost mean, edge, and peak throughput. However, results were based on capacity calculations, and not actual throughput. Furthermore, a homogeneous distribution of PHY resources was assumed, which may not be the case in a more realistic network, where typically proportional fair scheduling would be employed. In the remaining of this chapter, LTE FFR performance is analyzed in terms of throughput by means of LTE system level simulations, concluding that when combined with scheduling, FFR provides no tangible additional gains in terms of optimum performance.

5.3. System Model

Performance has been evaluated for a 4×4 MIMO antenna configuration employing CLSM. In order to be able to evaluate the complete space of FFR configurations, an exhaustive search over all possible FFR configurations has been performed. The configuration parameters taken into consideration are as follows:

- Bandwidth partitioning β_{FR}: values from reuse-1 ($\beta_{\mathrm{FR}} = 1$) to practically reuse-3 ($\beta_{\mathrm{FR}} = 0.01$). As the frequency partitioning in LTE is based on RBs, the β_{FR} frequency allocation is constrained to allocate an integer and zero-modulo-

three number of RBs to the FR zone and PR zone. Thus, the obtaining stepping $\beta_{\mathrm{FR}} = 0.01, 0.04, \ldots, 1$ (100 RBs cannot be equally distributed to three PR zones).

- FR-PR SINR threshold: the SINR threshold, denoted as Γ_{thr}, specifies the wideband SINR point at which the switching between FR and PR is performed. A set ranging from the cell center (22.5 dB) to cell edge (-2 dB) has been taken into account. The wideband SINR Γ is defined, as in Equation (3.16), as

$$\Gamma = \frac{G_{\mathrm{antenna}}\, L_{\mathrm{macro},0}\, P_{\mathrm{tx}_0}}{\sigma_n^2 + \sum_{l=1}^{N_{\mathrm{int}}} L_{\mathrm{macro},l}\, P_{\mathrm{tx}_l}}.$$

- Scheduling: independent zone scheduling is applied. For each zone, the UEsare independently scheduled. Two configurations having been analyzed, as listed in Table 5.1: (i) round robin and (ii) proportional fair scheduling [134], in both cases applied to both the FR and PR zones.

The full list of simulation parameters is detailed in Table 5.1.

Table 5.1.: Simulation parameters employed for the LTE FFR simulations.

Inter-eNodeB distance	500 m [83]
Number of eNodeBs	57 (two rings, 19 sites)
UEs per eNodeB	30
Considered UEs	Center 7 sites (21 cells): 630 UEs
Pathloss model	Urban area[69], 70 dB MCL
Shadow fading	none
Minimum coupling loss	70 dB [69]
Antennas ($N_{\mathrm{TX}} \times N_{\mathrm{RX}}$)	4×4
Antenna radiation pattern	KATHREIN 742 212
Antenna downtilt	8°, electrical
TX power	40 W
MIMO mode	CLSM [39]
Feedback	AMC: CQI, MIMO: PMI and RI
Feedback delay	3 ms
Channel model	Winner Phase II [76, 122]
UE speed	5 km/h
Total bandwidth	20 MHz (100 RBs)
Receiver modeling	Zero Forcing [78]
Noise spectral density N_0	-174 dBm/Hz
SINR threshold Γ_{thr} range	-2:0.25:22.5 (99 values)
Bandwidth ratio β_{FR} range	0.01:0.03:1 (34 values)
Total number of simulations	3 366
Simulation length	50 subframes (TTIs)
Traffic model	Full buffer
Scheduling algorithm	Round Robin and Proportional fair [134]

Combining the number of β_{FR} values and Γ_{thr} values taken into consideration, 3 366 FFR simulations are required to evaluate throughput performance for each scheduler configuration. An example UE and eNodeB distribution from one of the 3 366 simulated ones in shown in Figure 5.4. The figure corresponds to the FFR configuration $\beta_{\mathrm{FR}} = 0.7$, $\Gamma_{\mathrm{thr}} = 12.75\,\mathrm{dB}$. In blue are the UEs the results of which are taken into account (center cells, grey-marked). In order to reduce simulation time and avoid border-map artifacts, UEs not attached to the center cells, marked pale-red, are skipped. Marked as blue dots, are the FR UEs, while crosses mark the PR UEs. As shown in Figure 5.2, the FR zone extends in the direction the antennas of the eNodeB radiate (marked with a line), extending in a petal-shape from each site.

The same set of channel realizations have been employed by all simulations, so as to avoid a necessary averaging over channel realizations if independent ones would have been taken into account. While employing the same channel realizations for each simulation will not yield statistically significant throughput results, the relative difference between FFR and reuse-1 will still be valid, which can equally answer the question of the usefulness of FFR applied to LTE.

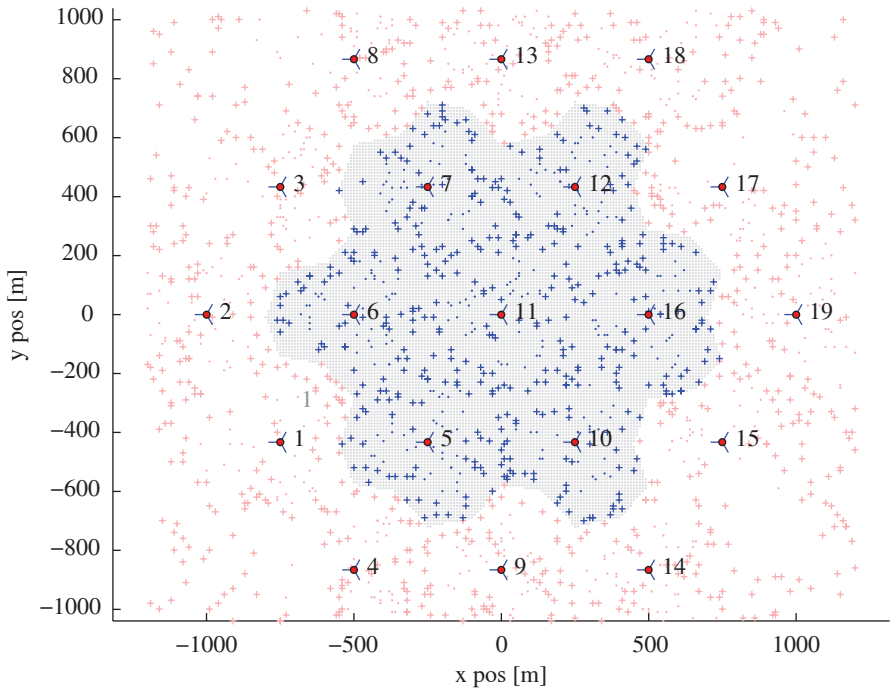

Figure 5.4: Network layout and UE distribution for one of the 3 366 LTE system level simulations employed in one FFR performance evaluation batch. $\beta_{\mathrm{FR}} = 0.7$, $\Gamma_{\mathrm{thr}} = 12.75\,\mathrm{dB}$. Marked grey are the cells taken into acocunt for the results. Outside of this area, UEs are not simulated (red UEs). In blue are the UEs in the considered cells (dots represent FR UEs, crosses PR UEs).

5.4. Round Robin Simulation Results and Fairness Metric

The UE throughput results for the round robin scheduling case, in which the PHY resources are equally distributed among the 30 UEs in the cell, are shown in Figure 5.5. Every colored dot in each of the figures represents the average UE throughput (from left to right: mean, edge and peak throughput) obtained from an LTE system level simulation with β_{FR} and Γ_{thr} corresponding to the values in the x- and y-axis, respectively.

In the upper row, mean, edge, and peak UE throughput in Mbit/s is depicted, while the lower row exhibits throughput gains (%) respective to the reuse-1 case. Additionally in the lower row, the area corresponding to an improvement of average and edge throughput are highlighted. As previous treatments of FFR focused on an optimization of the average and edge throughput, this aims at visualizing a similar throughput region of interest.

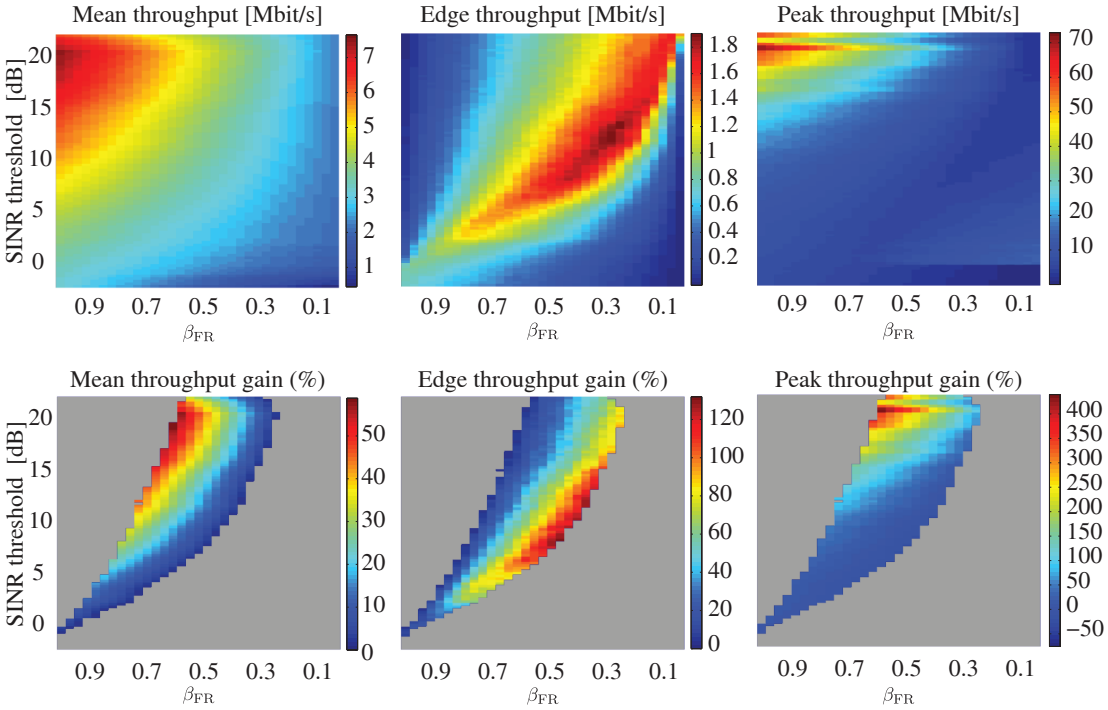

Figure 5.5: LTE FFR throughput results with round robin scheduling. Mean/edge/peak throughput (Mbit/s) over the simulated β_{FR} and Γ_{thr} set (top row) and throughput gain relative to the reuse-1 case (%) for the area where mean and edge throughput gain is positive (bottom row).

Just taking into account these metrics, results indicate the existence of FFR configurations that improve average, edge, and peak throughput, and thus offer an apparent overall performance increase. However, more careful examination of such cases show that these performance metrics do not properly reflect the throughput distribution.

Serving as an exemplifying point, the FFR configuration with frequency allocation $\beta_{\mathrm{FR}} = 0.31$ and SINR threshold $\Gamma_{\mathrm{thr}} = 18\,\mathrm{dB}$ yields seemingly all-improving UE throughput results. For this case, the following UE throughputs are observed: mean UE throughput of 3.66 Mbit/s (+11.15 % compared to reuse-1), edge throughput of 1.28 Mbit/s (+73.04 %), and peak throughput of 12.91 Mbit/s (+75.28 %). Do note that this point does not correspond to the optimum point shown on Figure 5.3, but is rather an exemplifying FFR point. A more exhaustive examination of the simulation results offers a complete view of the distribution of the UE throughput.

In Figure 5.6, the UE throughput distribution, shown both as an ecdf (left) and a scatterplot over the FR wideband SINR are shown (reuse-1 is considered for the calculation of Γ, hence the term "FR SINR"). In the right plot, the boundary separating the PR (left, low SINR range) and FR (high SINR range) UEs at $\Gamma = 18\,\mathrm{dB}$ is marked.

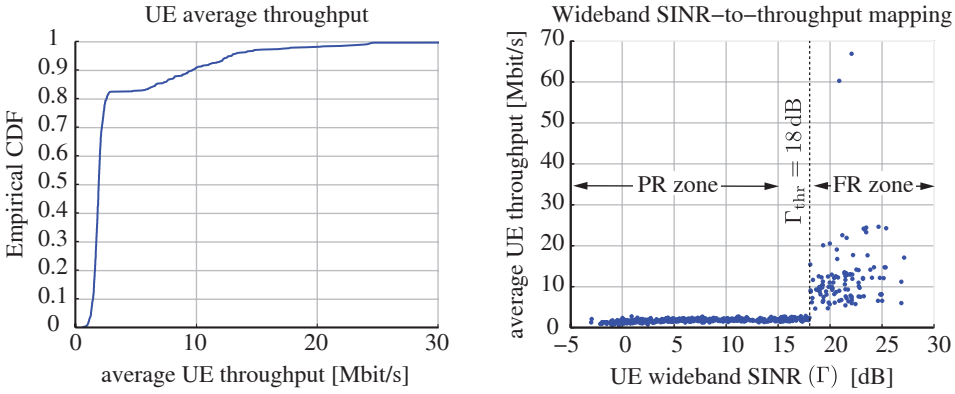

Figure 5.6: UE throughput distribution for the $\beta_{\mathrm{FR}} = 0.31$ $\Gamma_{\mathrm{thr}} = 18\,\mathrm{dB}$ FFR point. Left: UE throughput ecdf. Right: UE throughput over wideband SINR (Γ).

The ecdf shows that 80 % of the UEs experience low throughput, which albeit low, is still higher than the reuse-1 edge throughput. This translates into an edge throughput increase, which combined with a small group of UEs close to the cell center that obtain most of the throughput (peak throughput gain) that pushes the average throughput up, results in a gain in mean, edge, and peak throughput. However, an equally valid assertion is that the majority of UEs experience a performance degradation, despite what the throughput metrics may indicate, which obviously does not sound as desirable as the first assertion of overall gain.

As shown, the typical metrics to evaluate FFR performance can lead to results which, albeit seemingly good, are undesirable. By combining the previously-mentioned throughput metrics with a fairness metric, a better-suited performance evaluation of FFR performance is proposed [135].

Fairness, as first introduced in [57], rates how equally a resource (in this case through-

put) is distributed over N users. It is defined as

$$J(\mathbf{x}) = \frac{\left(\sum_{i=1}^{N} x_i\right)^2}{N \sum_{i=1}^{N} x_i^2}, \tag{5.1}$$

where $\mathbf{x}$ is a vector of length N containing the resources obtained by each of the N users. Applied to the results shown in Figure 5.6, fairness can be interpreted as either the steepness of the throughput ecdf or alternatively the flatness of the SINR-to-throughput mapping.

Figure 5.7 depicts, employing the same visualization as in Figure 5.5, the obtained fairness for all of the simulated β_{FR} and Γ_{thr} FFR value pairs, as well as the UE throughput ecdf associated the following three points of interest in the plot: (i) reuse-1, (ii) reuse-3 (its closest FFR approximation, where $\beta_{\mathrm{FR}} = 0.01$), and (iii) $\beta_{\mathrm{FR}} = 0.34, \Gamma_{\mathrm{thr}} = 10\,\mathrm{dB}$, where a high fairness gain relative to reuse-1 is achieved.

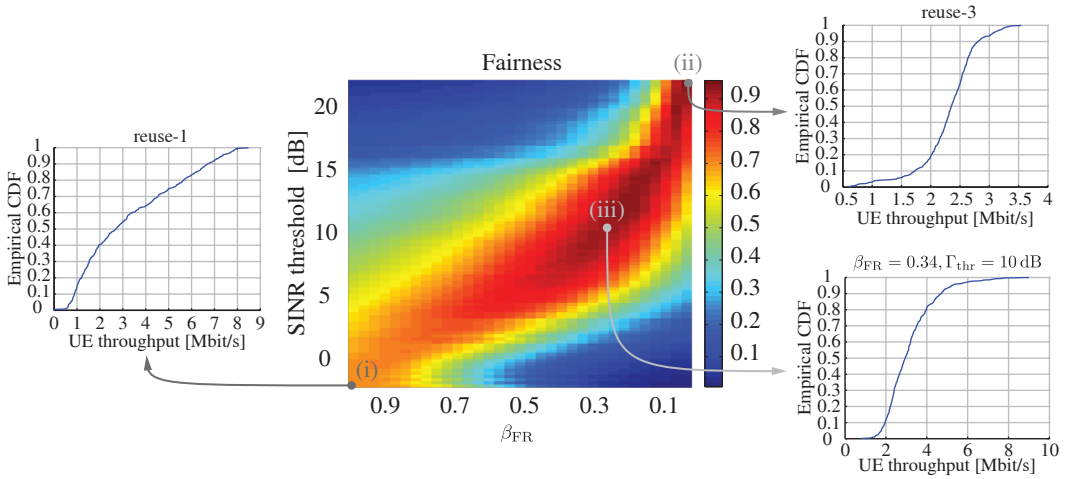

Figure 5.7: FFR fairness results employing round robin scheduling. The associated UE throughput ecdf is shown for the (i) reuse-1 case, (ii) reuse3 case, and (iii) $\beta_{\mathrm{FR}} = 0.34, \Gamma_{\mathrm{thr}} = 10\,\mathrm{dB}$ case.

Ideally, an operator of an LTE network would find it desirable to obtain a fairness gain (or at least not lose any fairness so as to avoid starvation of some UEs), while maintaining or ideally improving average throughput. Thus, ensuring that cell throughput (i) is not reduced and (ii) is shared optimally among UEs.

With this constraint, a fairness increase while maintaining average throughput implies a throughput gain for the UEs with poor channel conditions, and vice versa. For the case depicted in Figure 5.6, a degradation in fairness from 0.69 (reuse-1 fairness) to 0.32 was observed, which indicates that the observed throughput gain is due to a more biased throughput distribution.

If just the area where $J_{\mathrm{FFR}} > J_{\mathrm{reuse1}}$ is taken into account, the mean, edge, and

peak UE throughput results shown in Figure 5.8 are obtained.

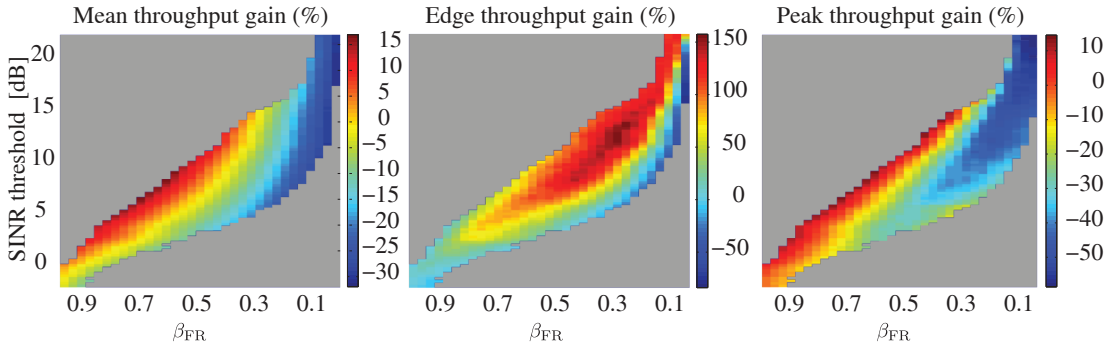

Figure 5.8: From left to right: Mean, edge, and peak throughput gain (%). Depicted is only the area where fairness is improved compared to the reuse-1 case.

Constraining fairness ensures that the plotted points have a throughput distribution that is at least as fair as the one of reuse-1. Overall, the results show that in order to improve edge throughput, one has to sacrifice from the peak UEs and, less but also to some extent, average throughput.

Out of the fairness-enhancing set, our interest lies in showing how optimal the trade-off between mean throughput and fairness can be: i.e., maximizing the fairness gain while minimizing mean throughput loss. Thus, we are interested in finding the points where: (i) fairness is maximum relative to mean throughput loss, and (ii) the maximum achievable fairness is obtained without incurring in mean throughput loss. Figure 5.9 depicts this trade-off between fairness and mean throughput gain/loss.

Considering the FFR points depicted in Figure 5.8 (i.e., FFR configurations in which fairness is improved with respect to the reuse-1 case), a set of points with the following components is obtained: (i) β_{FR}, (ii) Γ_{thr}, (iii) J_{FFR}, (iv) mean throughput, (v) edge throughput, and (vi) peak throughput.

Plotting the relation between fairness and mean throughput yields the plot in Figure 5.9. Only the FFR combinations improving fairness are considered, thus the lowest (y-axis-wise) point with a 0% mean throughput gain corresponds to the reuse-1 case. The envelope of scatterplot points corresponds to the FFR configurations in which the trade-off between mean throughput and fairness is optimum (marked red), with the following three significant performance points highlighted: (i) optimum trade-off between fairness and mean throughput, (ii) no mean throughput loss, but increased fairness, and (iii) no fairness loss, but increased mean throughput.

Additionally, edge and peak throughput performance are also evaluated over mean throughput performance gain, which is shown in Figure 5.10. There, the red points mark the same FFR configurations marked in Figure 5.9, i.e., the optimum trade-off FFR configurations between mean average throughput and fairness. Combining the

results shown in Figures 5.8 and 5.9, the following conclusions are drawn:

- Without losing any mean throughput or fairness with respect to the reuse-1 case, it is possible to obtain obtain an additional 15% average throughput, 50% edge throughput, and 10% peak throughput.
- Constrained to not losing any mean throughput, fairness can be improved to 0.85, which doubles edge throughput at the cost of a 20 % loss of peak throughput.
- It is possible to maximally increase fairness up to 0.93 by sacrificing 15% mean, and 45% peak throughput, as well as a being able to set fairness to a variety of points in-between.

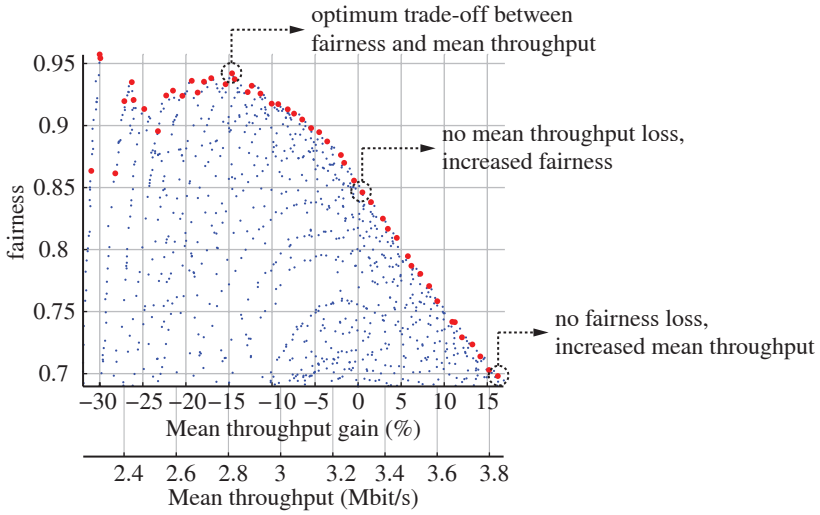

Figure 5.9: Trade-off between fairness and mean throughput for round robin scheduling. Red: optimum fairness-to-mean-throughput trade-off envelope.

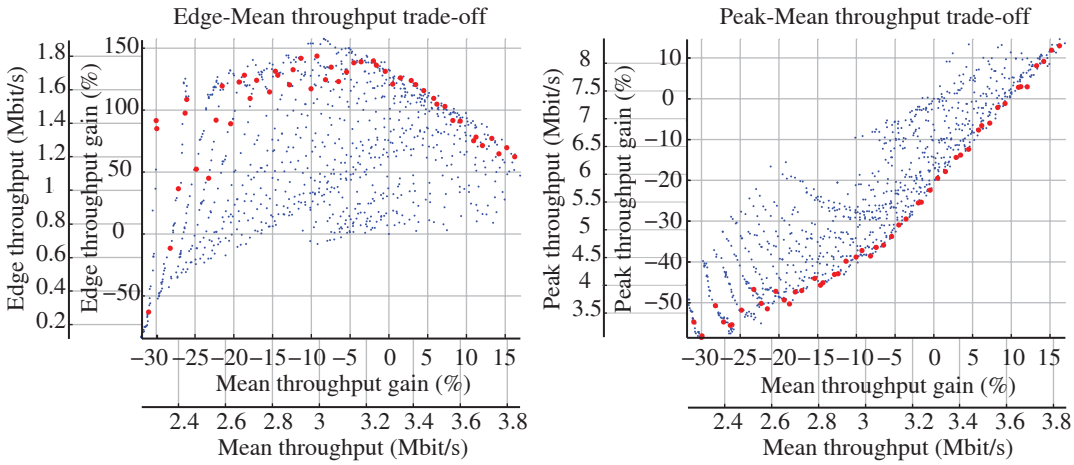

Figure 5.10: Left: Trade-off between edge throughput and mean throughput (round robin scheduling). Left: Trade-off between peak throughput and mean throughput. Marked red: optimum fairness-to-mean-throughput trade-off.

5.5. Proportional Fair Simulation Results

It has been shown in Section 5.4 that a gain in throughput, as well as fairness, is possible by means of applying FFR on top of round robin scheduling, compared to the case in which no FFR is applied. However, in practice, scheduling algorithms more elaborate than round robin are employed. A compromise between throughput and fairness, while still maximally exploiting multi-user diversity is desired. Thus, proportional fair scheduling [136] or more complex fairness-adjusting scheduling mechanisms [137] are routinely used instead. In order to analyze its impact in a more realistic setting, the performance of FFR when combined with Proportional Fair (PF) scheduling is analyzed in this section.

Figure 5.11 shows fairness results for FFR with PF scheduling applied to the FR and PR zones. The main difference that can be observed compared to the round robin results is that the achievable fairness values are much closer to those of the reuse-1 case, which is equivalent to the FFR configuraiton with $\beta_{\mathrm{FR}} = 1$ and a minimum Γ_{thr} SINR threshold point. In fact, there is basically no possibility of increasing fairness relative to the reuse-1 case without losing mean throughput.

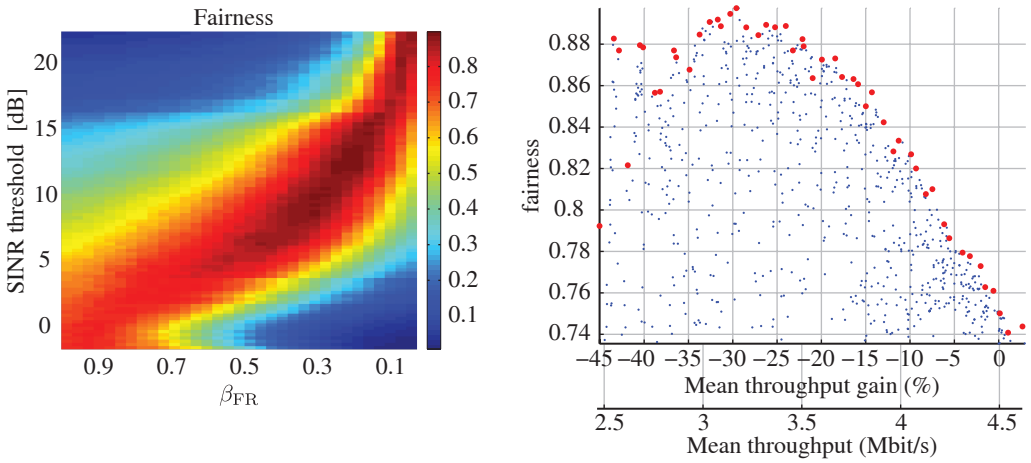

Figure 5.11: Fairness results for FFR with proportional fair scheduling. Left: fairness results over β_{FR} and Γ_{thr}. Right: Trade-off between fairness and mean UE throughput.

The same can be observed from the distribution of the optimum fairness-to-mean-throughput trade-off points (marked red) in Figure 5.12. Although showing a similar shape, the results for edge throughput (left) and peak throughput (right), do not exhibit gains such as those in the round robin case. As PF scheduling is already pareto-optimal [137], FFR cannot extract further gains from MU diversity. Although this results show that FFR cannot, in practice, be employed to simultaneously increase throughput and fairness, it can still, be employed as a simple method for variably controlling the trade-off between increased fairness and decreased cell throughput.

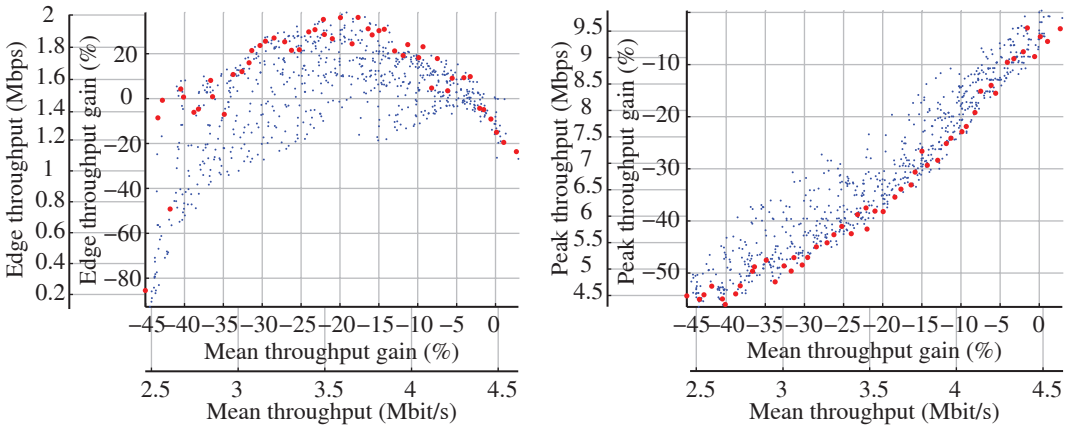

Figure 5.12: Left: Trade-off between edge throughput and mean throughput (PF scheduling). Left: Trade-off between peak throughput and mean throughput. Marked red: optimum fairness-to-mean-throughput trade-off.

5.6. Side-to-side Comparison and Multi-User Gain Results

As seen from the results shown in Figure 5.13, which combines the results from Sections 5.4 and 5.5, FFR can increase the throughput without decreasing fairness only in the case of round robin scheduling, although the gain vanishes if it is employed on top of proportional fair scheduling. However, tweaking the FFR parameters does allow for a flexible trade-off between fairness and throughput. Two operating points of interest for network deployments have been evaluated: (i) maximum mean throughput without fairness loss, and (ii) maximum achievable fairness while maintaining an optimum mean-throughput-to-fairness trade-off, which are marked in Figures 5.13 and 5.14 as (i) and (ii), respectively.

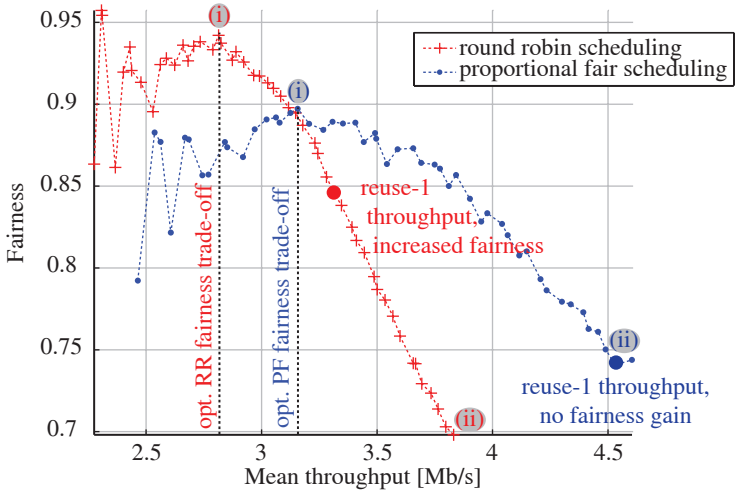

Figure 5.13: Trade-off between fairness and mean UE throughput for round robin and proportional fair scheduling. Performance points of interest additionally marked.

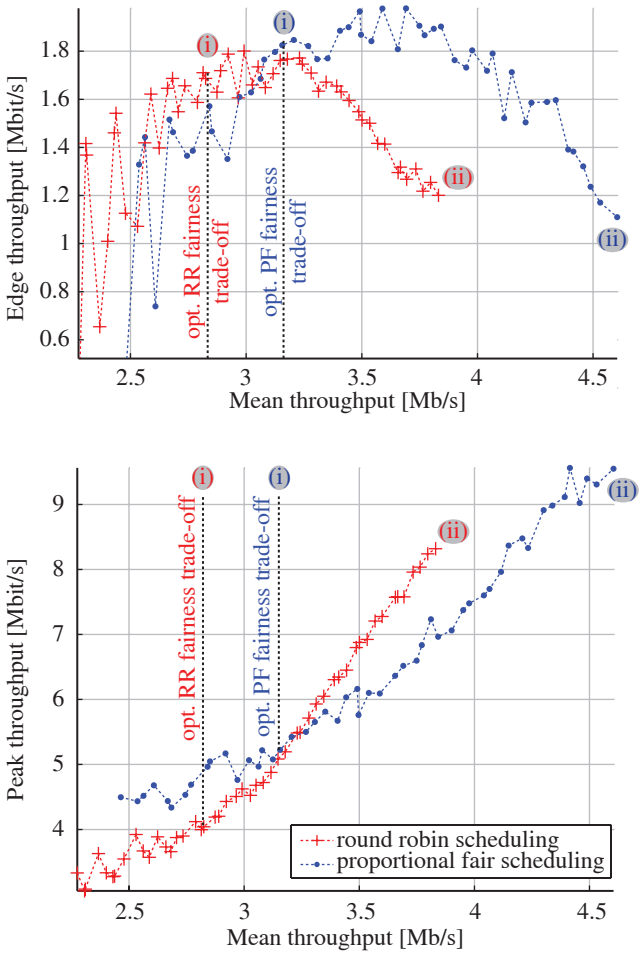

Figure 5.14: Edge (top) and peak (bottom) UE throughput vs. mean UE throughput: round robin and proportional fair scheduling.

In Figure 5.14, analogous plots are shown for the relationship of the mean UE throughput vs. edge and peak UE throughput, respectively. As expected from the relationship imposed between mean, edge, and peak throughput by the fairness constraint, the same effects observed in the results shown in Figure 5.13 are observed in Figure 5.14.

The most desirable situation would be that of a "free" gain also for the proportional fair scheduler, where the throughput accomplished in target (i) is higher than that of the reuse-1 case or when in (ii), higher fairness values can be achieved without decreasing throughput. However, as seen from the results in Figures 5.13 and 5.14, this is *not* possible.

While 30 UEs per cell can be considered a big enough number to be considered analogous to a continuous distribution, it is also necessary to evaluate the performance of FFR in less loaded situations. To this effect, for the optimum trade-off points listed as (i) (maximum fairness) and (ii) (maximum throughput without fair-

ness loss), throughput and fairness performance has been evaluated over a range of number UEs/cell values. Small confidence intervals are ensured by averaging over enough independent different channel realization sets and UE positions such that each plotted point is obtained from averaging at least 500 UE throughput points.

The results, shown in Figure 5.15, depict on addition the MU-gain analysis results from Appendix D, so as to compare the FFR MU gain results to those of different reuse-1 scheduling strategies. Results indicate that, in order for a static FFR scheme such as the one assumed in this chapter to work, at least 5 UEs per cell are necessary. With less, throughput results do not converge to the FFR result. While for the round robin case, fairness can be consistently increased at no throughput cost, it is also clear that the same behavior does not hold for PFs. At the optimum trade-off point, both cases do offer similar results. While the achievable fairness is slightly lower for PF than round robin (the PF scheduling algorithm pushes aways from extreme results), throughput is slightly better for PF, as demonstrated in Figure 5.13. Best CQI scheduler results are shown as comparison to the maximum achievable multi-user gain, which of course comes also at the expense of fairness.

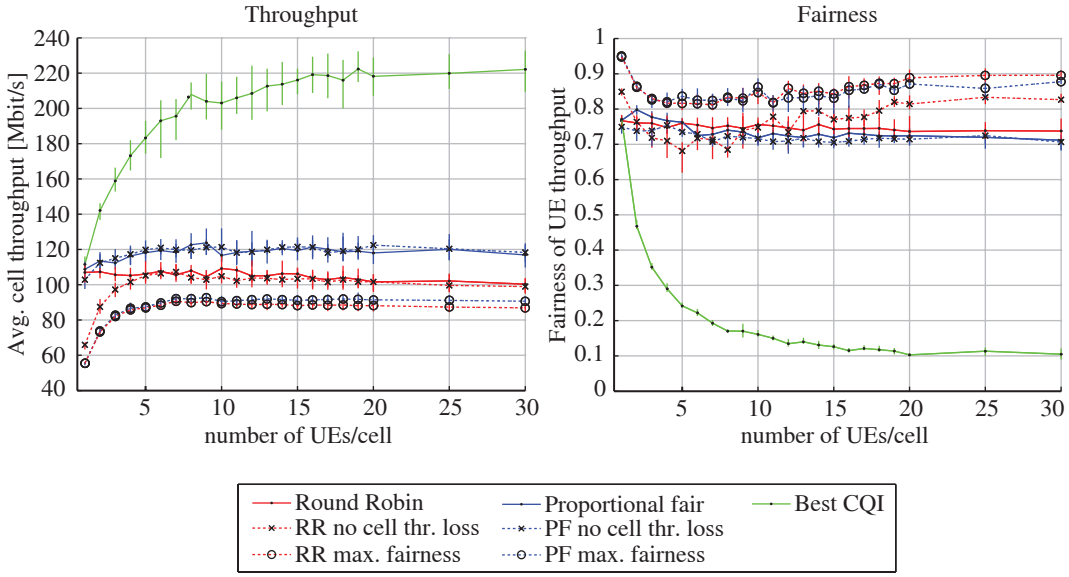

Figure 5.15: Performance over number of UEs per cell for the following schedulers: round robin, proportional fair, best CQI, FFR-enabled round robin, and FFR-enabled proportional fair. The performance of the the FFR-enabled schedulers is evaluated for the FFR configurations were (i) the optimum trade-off between fairness and mean throughput is achieved and (ii) for the case where no mean throughput loss occurs compared to the reuse-1 case. Left: cell throughput. Right: UE throughput fairness. Vertical lines: 95 % confidence intervals.

The conclusion of this chapter is that, taking into account that PF scheduling is anyway used, due to its increased throughput at the same fairness level compared to round robin scheduling, the usefulness of FFR is limited to allowing a flexible fairness

allocation in highly loaded networks. In a less loaded scenario, this could, however, only be accomplished with more complex dynamic coordinated FFR schemes. For loads lower than 5 UEs per cell, FFR is outright unsuited, as results show always severe throughput degradation compared to simple scheduling[1].

[1] Fairness is evaluated network-wide, and not cell-wise. Thus, fairness results for the 1 UE/cell case are not one.

6. Summary and Outlook

6.1. Summary

In this thesis, an accurate, low-complexity link-to-system model for 3GPP LTE Release 8 is presented. The model is based on a ZF linear receiver and separates the link abstraction procedures into a link quality model and a link performance model. The link quality model outputs a per-subcarrier post-equalization SINR, which the link performance model compresses via MIESM to an AWGN-equivalent SINR value and is then mapped to BLER by means of link-level-generated curves.

Based one the presented L2S model, a complete LTE system level simulation has been built, which also integrates the network layout (pathloss, shadow fading, eNodeB and UE placement), as well as a Winner Phase II channel model and appropriate MIMO feedback. This allows for performance evaluation of different scheduling algorithms and interference coordination schemes such as FFR.

In Chapter 3, the post-equalization SINR for each of the LTE transmit modes is derived and combined with all of the parameters characterizing an LTE network deployment. An extended correlation matrix for generation of spatially-correlated shadow fading generation is also applied. As for the same correlation distance, a smaller pixel resolution in the pathloss maps requires of more neighbors for the spatial correlation computation, the applied extended correlation matrix increases the accuracy of the shadow fading maps in cases where more resolution is needed. For configurations of up to 4×4, the accuracy of the model is validated against link level simulations, confirming the accuracy of the L2S model in single- and multi-cell simulation scenarios.

Employing the maximum LTE channel bandwidth of 20 MHz, significant gains in simulation run-time are introduced by employing the presented link abstraction

model. A run-time comparison has been carried out for a single-cell, single-user scenario, comparing link and system level simulator run times. The estimated simulation run-time speed-ups for each of the implemented mode and antenna configuration are shown in Table 6.1 and range between 140x and 1 150x overall compared to link level results. For the most complex case of CLSM, simulation run time gain has been estimated at 359x.

Table 6.1.: System level simulator speed-up compared to link level simulation run time, 20 MHz bandwidth scenario.

	Single TX		TxD	OLSM			CLSM		
	1×1	1×2	2×2	2×2	4×2	4×4	2×2	4×2	4×4
speed-up	153x	140x	351x	665x	836x	1 150x	200x	259x	359x

In Chapter 4, two enhancements to the L2S model are proposed. In the first part, the link performance model is extended to include HARQ in the BLER calculation. The joint processing of a received HARQ retransmission is modeled as a combination of an inner channel code and an outer repetition code, the rates of which are derived from link level results. The model is based on the structure of the LTE rate matcher, as well as a mutual information-based combining of the post-equalization SINRs of each of the retransmissions to estimate the BLER of the combined data packet.

Additionally, the link quality model is extended to take into account imperfect channel information into the calculation of the post-equalization SINR of the data symbol positions. The model is also based on the ZF receiver and characterizes the total channel estimation error as a linear function of the sum received interference power and the noise level.

In Chapter 5, the performance of FFR applied to LTE is evaluated. On a network layout consisting of a hexagonal cell layout, all possible FFR configurations are tested combined with (i) round robin scheduling and (ii) proportional fair scheduling. In order to avoid skewed throughput distributions, a fairness metric is introduced, which adds the constrain of no fairness loss with respect to the reuse-1 case.

Simulation results show that, while with the round robin scheduler an overall increase in throughput and fairness is possible, with proportional fair scheduling, the gain is limited to the flexibility of exploiting a fairness-throughput trade-off, without the possibility of a gain in both.

In this static scenario, it is shown that FFR cannot properly function if less than 5 UEs/cell are present, thus reducing its practical applicability to highly-loaded scenarios unless combined with dynamic allocation.

6.2. Outlook

With LTE, as in the case of UMTS, enhancements to the standard began as soon as the first release (Release 8) was specified. Releases 10 and 11, termed LTE-Advanced, are already following a clear standardization path, with research proposals for Beyond-LTE (LTE-B) already trying to address future issues.

The currently-implemented model is already adequate for single user MIMO and correctly scales for higher number of cells, which is expected as more dense cell deployments of small-cell sizes (pico-, femto-) are adopted to increase network throughput [138]. Minor enhancements to the model will allow it to evaluate energy efficiency and latency issues, already hot topics of discussion for LTE-A/B [139, 140], as well as Carrier Aggregation (CA), which can bring the usable bandwidth to up to 100 MHz [83, 141].

However, improvements in the PHY will provide new modeling challenges, as MU-MIMO and interference-coordination schemes such as Interference Alignment (IA) or Cooperative Multi-Point (CoMP) need to be included into the L2S model as well.

As the number of small cells becomes higher, cellular networks will, up to a certain point, stop being planned and will rely more on self-organizing spectrum allocation to avoid interference, for which an extra modeling layer of inter-cell coordination and communication could be designed. Additionally, new models may also be needed to include the effect of Machine-to-Machine (M2M) communications where up to 1000+ machines/cell may be sporadically communicating.

In prior standards, it remained the duty of the physical layer to provide a link with an ever-increasing spectral efficiency. Currently, the importance of MAC and inter-cell coordination schemes in order to exploit multi-user gain and spatial reuse (smaller cells) has steadily increased. With it grows also the importance of accurate and low-complexity models such those presented in this thesis. Future link abstraction models will continue to allow performance evaluation of ever-more-complex network deployments with an ever-increasing degree of self-organization, interference coordination and, as a result, increased performance.

A. SNR-independence of the CLSM Precoder Choice

This appendix justifies the assumption in Section 3.1.1.3 that the optimum precoder matrix choice can be performed independent of the SNR without any relevant loss of accuracy.

Noting as $\tilde{\mathbf{H}}$ the effective channel matrix, which is expressed as the channel matrix $\mathbf{H}$ multiplied by the precoder $\mathbf{W}$, the post-equalization SINR (γ) for the k-th transmitted symbol (k-th layer) is expressed as

$$\gamma_{\mathrm{ZF},k} = \frac{1}{\left[\rho \left(\tilde{\mathbf{H}}^{\mathrm{H}}\tilde{\mathbf{H}}\right)^{-1}\right]_{kk}}, \tag{A.1}$$

where ρ denotes the $\mathrm{E_b/N_0}$ divided by the number of receive antennas N_{RX}, and $[\cdot]_{kk}$ is the k-th diagonal element of the MSE matrix.

The total spectral efficiency, denoted as C is the sum over the K layers, which is expressed as

$$C = \sum_{k=1}^{K} \log_2\left(1+\gamma_k\right). \tag{A.2}$$

Via a Singular Value Decomposition (SVD) of $\mathbf{H}$, we can express the effective channel matrix product ($\tilde{\mathbf{H}}^{\mathrm{H}}\tilde{\mathbf{H}}$) as

$$\mathbf{W}^{\mathrm{H}}\mathbf{H}^{\mathrm{H}}\mathbf{H}\mathbf{W} = \mathbf{W}^{\mathrm{H}}\mathbf{V}\mathbf{\Lambda}\mathbf{U}^{\mathrm{H}}\mathbf{U}\mathbf{\Lambda}\mathbf{V}^{\mathrm{H}}\mathbf{W} = \underbrace{\left(\mathbf{W}^{\mathrm{H}}\mathbf{V}\right)}_{\mathbf{P}}\mathbf{\Lambda}^2\underbrace{\left(\mathbf{W}^{\mathrm{H}}\mathbf{V}\right)^{\mathrm{H}}}_{\mathbf{P}^{\mathrm{H}}}, \tag{A.3}$$

where Λ^2 contains the eigenvalues of $\mathbf{H}$

$$\mathbf{\Lambda}^2 = \begin{bmatrix} \lambda_1^2 & 0 & \dots & 0 \\ 0 & \lambda_2^2 & \dots & 0 \\ \vdots & \vdots & \ddots & \vdots \\ 0 & 0 & \dots & \lambda_K^2 \end{bmatrix}, \tag{A.4}$$

and $\mathbf{P}$ depends on the precoder. Thus,

$$\gamma_{\mathrm{ZF},k} = \frac{1}{\left[\rho \left(\mathbf{P}\mathbf{\Lambda}\mathbf{P}^{\mathrm{H}}\right)^{-1}\right]_{kk}}, \tag{A.5}$$

For the full-rank case, where $\mathbf{H}$ and $\mathbf{W}$ are square, $\mathbf{P}$ is unitary, and the per-layer post-equalization SINR can be expressed as

$$\gamma_{\mathrm{ZF},k} = \frac{1}{\rho \left[\mathbf{P}\mathbf{\Lambda}^{-2}\mathbf{P}^{\mathrm{H}}\right]_{kk}} = \frac{1}{\rho \sum_{i=1}^{K} \frac{|p_{k,i}|^2}{\lambda_i^2}}, \tag{A.6}$$

thus simplifying the matrix inverse, where $p_{k,i} \triangleq [\mathbf{P}]_{k,i}$. The spectral efficiency given a precoder $\mathbf{W}$ can then be written as

$$C = \log_2 \prod_{k=1}^{K} \left(1 + \frac{1}{\rho \sum_{i=1}^{K} \frac{|p_{k,i}|^2}{\lambda_i^2}} \right). \tag{A.7}$$

The optimum precoder choice employs an approximation for the high-SNR regime $(1 + \gamma_k \approx \gamma_k)$[1]. The rationale for applying the high-SNR regime approximation on the full SNR range and assuming independence of the noise value stems from the limited precoder choice. For the two-transmit antenna case, the codebook size is limited to four precoders, while for the four transmit antenna case, there are sixteen possible choices. Given such a small precoder codebook size, we argue that a good precoder choice would very probably remain good regardless of the noise level, which we show in the simulation results in the next section.

[1] For the non-full-rank cases, it will not be possible to write $\left[\left(\mathbf{P}\mathbf{\Lambda}^2\mathbf{P}^{\mathrm{H}}\right)^{-1}\right]_{kk}$ in such a compact form, thus the matrix product must be computed.

A.1. Simulation Results

Figure A.1 depicts, for a 4×4 antenna configuration, the overall spectral efficiency for all the combinations of precoder index (16 choices) and rank (4 choices). The employed channel matrix $\mathbf{H}$ is shown below, and has been purposely chosen to depict a case where relative precoder performance changes over SNR.

$$\mathbf{H}_{4\text{x}4} = \begin{bmatrix} -0.808 + 0.128i & 0.921 - 1.557i & 0.072 + 0.372i & -0.606 - 0.226i \\ -0.442 + 0.896i & -0.420 - 0.548i & 0.846 + 1.077i & -0.120 + 0.578i \\ -0.827 - 0.178i & 0.309 - 0.985i & 0.085 + 1.272i & -0.136 + 0.347i \\ 0.278 - 0.145i & -0.357 - 0.273i & -0.733 - 0.083i & -0.612 + 0.541i \end{bmatrix} \tag{A.8}$$

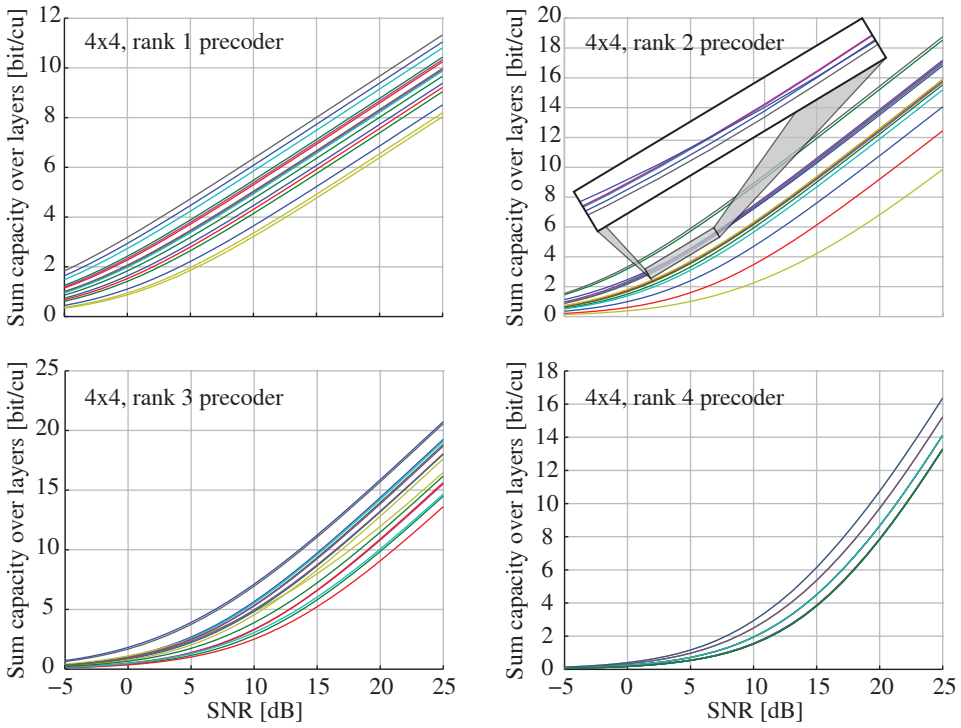

Figure A.1: Sum spectral efficiency for the channel matrix $\mathbf{H}$ shown in Equation (A.8) for the 16 precoders defined for the four-transmit-antenna configuration defined by the LTE standard [39]. Zommed (top-right): crossing in the mutual-information-wise precoder performance.

In the high-SNR regime, the precedence in terms of performance between any two given precoders is independent of the SNR. However, at low SNR, crossings may appear, such as for the rank 2 case at 5 dB SNR.

The effect of applying the high-SNR approximation on the whole SNR range has

been quantified by simulation for the 4×4, 4×2, and 2×2 antenna configurations. For a set of 100 000 uncorrelated independent channel realizations, the sum spectral efficiency over all layers for each precoder is calculated and the deviation between the high-SNR approximation and the optimum choice calculated.

Figure A.2 shows the results of the 4×4 antenna configuration. The left plot depicts, for each SNR point, the failure ratio of the high-SNR approximation, which as expected, decreases with SNR. Although for the higher ranks the probability of choosing a wrong precoder may seem high, it is not significant whether the precoder choice was correct, rather than how inaccurate is the throughput result of the high-SNR approximation relative to the optimum choice.

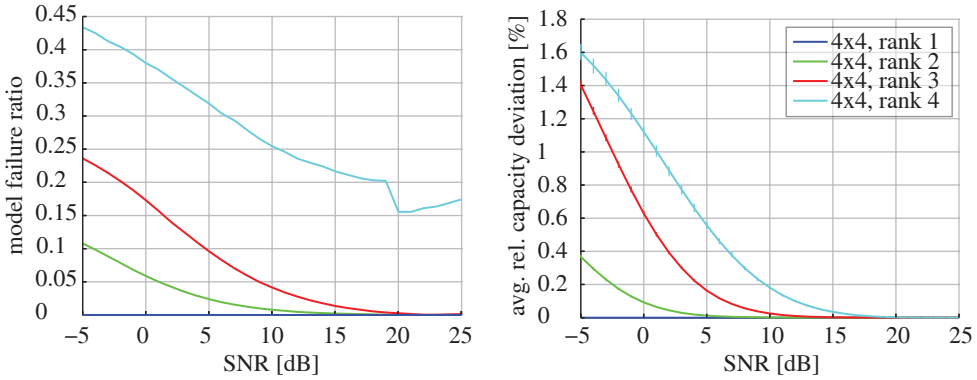

Figure A.2: 4×4 antenna configuration: High-SNR CLSM precoder choice accuracy results for each possible rank choice. Left: model failure rate. Right: deviation in terms of capacity (% the optimum choice).

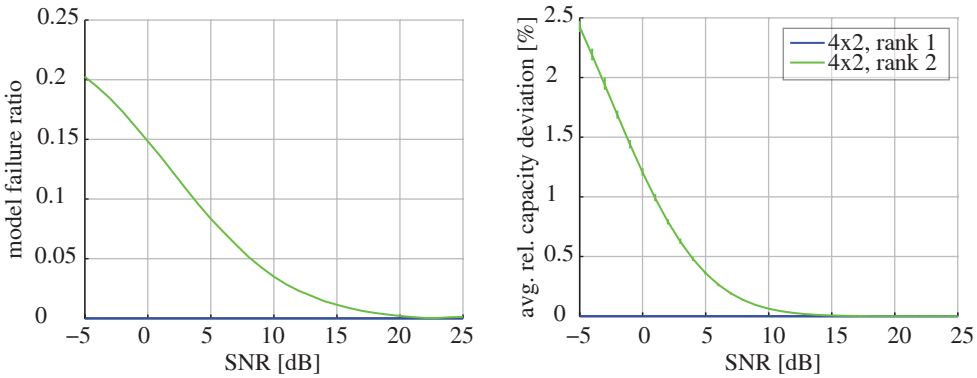

Figure A.3: 4×2 antenna configuration: High-SNR CLSM precoder choice accuracy results for each possible rank choice. Left: model failure rate. Right: deviation in terms of capacity (% the optimum choice).

The right plot in Figure A.2 depicts the average relative capacity deviation that results from this error. Results for the 4×2 antenna configuration are provided in Figure A.3, and show results similar to those found for the 4×4 case. For the 2×2 case, due to the smaller codebook size, the model was found to have a failure rate

of zero. The 95% confidence intervals are shown as vertical bars on the curves.

The high-SNR approximation is shown to be always accurate for the rank-one transmission, with the ratio of a wrong optimum precoder choice growing with the number of layers. For the four-layer case, a suboptimal precoder was chosen in average between 40% to 20% of the cases in the -5 dB-25 dB SNR range are observed, which albeit seemingly big, maps to an error between 1.6% to 0.6% in terms of sum spectral efficiency. For the 4×2 case, the worst-case deviation ranges from 2.3% to 0.4%.

Further decreasing the impact of the deviation is the fact that at low SNR, a high-rank precoder will very probably not be used. Figure A.4 depicts the average sum spectral efficiency for the optimum precoder choice over SNR for the 4×2 and 4×4 antenna configurations for the low-SNR range of -5 dB to 5 dB SNR.

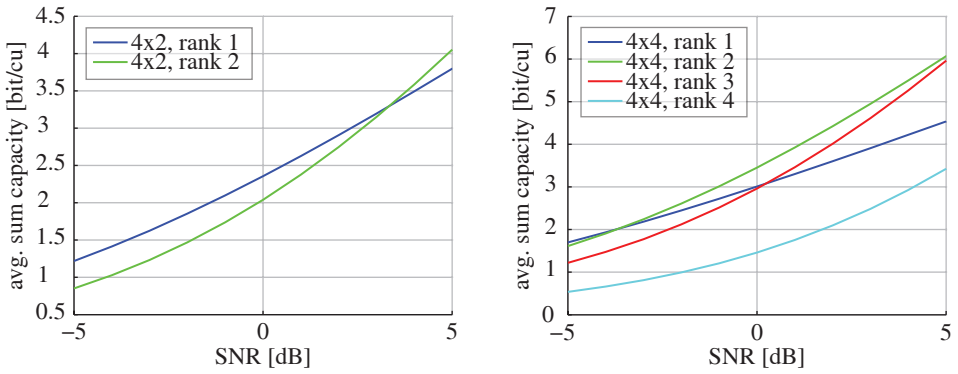

Figure A.4: Sum-capacity over SNR with an optimum precoder choice for each possible rank choice. Left: 4×2 antenna configuration. Right: 4×4 antenna configuration

As the UE feedback algorithm is to choose the PMI and RI combination maximizing the sum capacity, a low RI value is to be chosen at low SNR with high probability, which is exactly where the model is most precise.

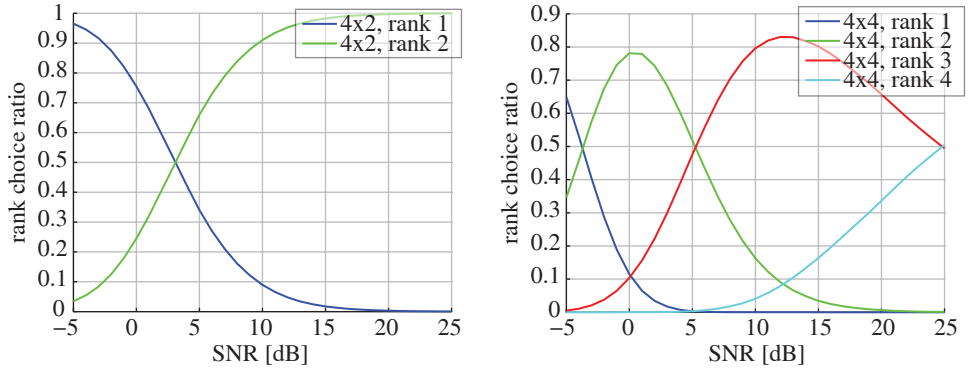

Figure A.5: Rank of the optimum precoder choice over SNR.

This effect is shown in Figure A.5, where for each channel realization, the rank distribution of the optimum PMI-RI combination is shown. For the 4 × 4 case, a

rank of four will not be employed in the low-SNR regime, while a rank of three will only be employed in the SNR range where the deviation is already low. The same applies for the 4×2 case, thus confirming that a high-rank precoder choice on a low SNR range, which suffers of model inaccuracy, is a negligible source of error..

Hence the conclusion that the optimum precoder can be chosen independently of the SNR (i.e., precalculated offline) with no impact in the output of the L2S model.

Accepting this negligible deviation in the L2S model allows for a drastic simplification in runtime complexity, making it possible to substitute complex-valued matrix multiplications and inverses with scalar products of precomputed fading parameters, as shown in Section 3.1.1.3.

B. Correlation Matrices for Shadow Fading Generation

This appendix details the correlation matrix employed for the generation of the shadow fading traces, which is explained in Section 3.1.1.5. The LTE L2S model presented in Chapter 3 extends the model in [87] to twelve neighbors, employing the correlation matrix detailed below.

The distance matrix (in pixels) between the current pixel, denoted as s_n, and its 12 neighbors $s_{n-1} \dots s_{n-12}$, is depicted in Figure 3.8:

$$\mathbf{X}_s = \begin{bmatrix} 0 & \sqrt{2} & 1 & \sqrt{5} & \sqrt{5} & 1 & 2 & \sqrt{8} & \sqrt{2} & \sqrt{10} & \sqrt{5} & \sqrt{13} & 1 \\ \sqrt{2} & 0 & 1 & 1 & 1 & \sqrt{5} & \sqrt{2} & \sqrt{2} & 2 & 2 & \sqrt{5} & \sqrt{5} & 1 \\ 1 & 1 & 0 & 2 & \sqrt{2} & \sqrt{2} & 1 & \sqrt{5} & 1 & 3 & \sqrt{2} & \sqrt{10} & \sqrt{2} \\ \sqrt{5} & 1 & 2 & 0 & \sqrt{2} & \sqrt{10} & \sqrt{5} & 1 & 3 & 1 & \sqrt{10} & \sqrt{2} & \sqrt{2} \\ \sqrt{5} & 1 & \sqrt{2} & \sqrt{2} & 0 & \sqrt{8} & 1 & 1 & \sqrt{5} & \sqrt{5} & 2 & 2 & 2 \\ 1 & \sqrt{5} & \sqrt{2} & \sqrt{10} & \sqrt{8} & 0 & \sqrt{5} & \sqrt{13} & 1 & \sqrt{17} & 2 & \sqrt{20} & 2 \\ 2 & \sqrt{2} & 1 & \sqrt{5} & 1 & \sqrt{5} & 0 & 2 & \sqrt{2} & \sqrt{10} & 1 & 3 & \sqrt{5} \\ \sqrt{8} & \sqrt{2} & \sqrt{5} & 1 & 1 & \sqrt{13} & 2 & 0 & \sqrt{10} & \sqrt{2} & 3 & 1 & \sqrt{5} \\ \sqrt{2} & 2 & 1 & 3 & \sqrt{5} & 1 & \sqrt{2} & \sqrt{10} & 0 & 4 & 1 & \sqrt{17} & \sqrt{5} \\ \sqrt{10} & 2 & 3 & 1 & \sqrt{5} & \sqrt{17} & \sqrt{10} & \sqrt{2} & 4 & 0 & \sqrt{17} & 1 & \sqrt{5} \\ \sqrt{5} & \sqrt{5} & \sqrt{2} & \sqrt{10} & 2 & 2 & 1 & 3 & 1 & \sqrt{17} & 0 & 4 & \sqrt{8} \\ \sqrt{13} & \sqrt{5} & \sqrt{10} & \sqrt{2} & 2 & \sqrt{20} & 3 & 1 & \sqrt{17} & 1 & 4 & 0 & \sqrt{8} \\ 1 & 1 & \sqrt{2} & \sqrt{2} & 2 & 2 & \sqrt{5} & \sqrt{5} & \sqrt{5} & \sqrt{5} & \sqrt{8} & \sqrt{8} & 0 \end{bmatrix}. \tag{B.1}$$

Assuming $\alpha = 1/20$, as stated in Section 3.1.1.5, and a pixel resolution d of 5 m, the

correlation matrix $\mathbf{R}_s$ can be expressed element-wise as

$$[\mathbf{R}_s]_{i,j} = \exp\left(-\alpha \cdot [\mathbf{X}_s]_{i,j} \cdot d\right), \tag{B.2}$$

resulting in a correlation matrix $\mathbf{R}_s$

$$\mathbf{R}_s = \begin{bmatrix}
1 & 0.7 & 0.78 & 0.57 & 0.57 & 0.78 & 0.61 & 0.49 & 0.7 & 0.45 & 0.57 & 0.41 & 0.78 \\
0.7 & 1 & 0.78 & 0.78 & 0.78 & 0.57 & 0.7 & 0.7 & 0.61 & 0.61 & 0.57 & 0.57 & 0.78 \\
0.78 & 0.78 & 1 & 0.61 & 0.7 & 0.7 & 0.78 & 0.57 & 0.78 & 0.47 & 0.7 & 0.45 & 0.7 \\
0.57 & 0.78 & 0.61 & 1 & 0.7 & 0.45 & 0.57 & 0.78 & 0.47 & 0.78 & 0.45 & 0.7 & 0.7 \\
0.57 & 0.78 & 0.7 & 0.7 & 1 & 0.49 & 0.78 & 0.78 & 0.57 & 0.57 & 0.61 & 0.61 & 0.61 \\
0.78 & 0.57 & 0.7 & 0.45 & 0.49 & 1 & 0.57 & 0.41 & 0.78 & 0.36 & 0.61 & 0.33 & 0.61 \\
0.61 & 0.7 & 0.78 & 0.57 & 0.78 & 0.57 & 1 & 0.61 & 0.7 & 0.45 & 0.78 & 0.47 & 0.57 \\
0.49 & 0.7 & 0.57 & 0.78 & 0.78 & 0.41 & 0.61 & 1 & 0.45 & 0.7 & 0.47 & 0.78 & 0.57 \\
0.7 & 0.61 & 0.78 & 0.47 & 0.57 & 0.78 & 0.7 & 0.45 & 1 & 0.37 & 0.78 & 0.36 & 0.57 \\
0.45 & 0.61 & 0.47 & 0.78 & 0.57 & 0.36 & 0.45 & 0.7 & 0.37 & 1 & 0.36 & 0.78 & 0.57 \\
0.57 & 0.57 & 0.7 & 0.45 & 0.61 & 0.61 & 0.78 & 0.47 & 0.78 & 0.36 & 1 & 0.37 & 0.49 \\
0.41 & 0.57 & 0.45 & 0.7 & 0.61 & 0.33 & 0.47 & 0.78 & 0.36 & 0.78 & 0.37 & 1 & 0.49 \\
0.78 & 0.78 & 0.7 & 0.7 & 0.61 & 0.61 & 0.57 & 0.57 & 0.57 & 0.57 & 0.49 & 0.49 & 1
\end{bmatrix}, \tag{B.3}$$

where $\mathbf{L}_s\mathbf{L}_s^{\mathrm{H}} = \mathbf{R}_s$, and $\tilde{\mathbf{L}}_s$ can be obtained by removing the last row and column of $\mathbf{L}_s$.

C. Taylor Expansion of the ZF MSE with Imperfect Channel Knowledge

This appendix details the derivation of the MSE expression in Equation (4.15), as well as a more detailed view of the channel estimation model employed in Section 4.2. It refers to the work in [117] and extends the solutions found in [118, 119, 142, 143] for the case of additional interferers.

The estimated channel matrix, denoted as $\hat{\mathbf{H}}$, is expressed as the sum of the channel matrix $\mathbf{H}$ and an error matrix $\mathbf{E}$:

$$\hat{\mathbf{H}} = \mathbf{H} + \mathbf{E}, \tag{C.1}$$

where the error matrix $\mathbf{E}$ is composed of complex-gaussian elements e_{ij}, i.e.,

$$e_{ij} \sim \mathcal{CN}\left(0, \sigma_e^2\right). \tag{C.2}$$

Taking into account the precoder matrix $\mathbf{W}$, the effective channel matrix $\tilde{\mathbf{H}}$ and the estimated effective channel matrix $\hat{\tilde{\mathbf{H}}}$ are expressed as

$$\tilde{\mathbf{H}} = \mathbf{H}\mathbf{W}, \qquad \hat{\tilde{\mathbf{H}}} = (\mathbf{H} + \mathbf{E})\,\mathbf{W} = \underbrace{\mathbf{H}\mathbf{W}}_{\tilde{\mathbf{H}}} + \underbrace{\mathbf{E}\mathbf{W}}_{\tilde{\mathbf{E}}}. \tag{C.3}$$

As the precoder does not change the overall transmit power when splitting it over the ν layers,

$$\mathbf{W}^{\mathrm{H}}\mathbf{W} = \frac{\mathbf{I}_\nu}{\nu}. \tag{C.4}$$

Additionally, as each non-zero element of $\mathbf{W}$ has a power equally distributed over all the non-zero elements of $\mathbf{W}$, each element of $\mathbf{W}$ has an average power of $\frac{1}{\nu N_{\mathrm{TX}}}$,

$$\tilde{\mathbf{E}} = \mathbf{E}\mathbf{W}, \qquad \tilde{e}_{i,j} \sim \mathcal{CN}\left(0, \sigma_e^2 \sqrt{\frac{N_{\mathrm{tx}}}{\nu}}\right), \qquad \hat{\tilde{\mathbf{H}}} = \tilde{\mathbf{H}} + \tilde{\mathbf{E}}. \tag{C.5}$$

The following notation is employed for the model parameters:

σ_x^2 = Average power allocated for transmission over all transmit antennas.
σ_v^2 = Average received noise power per antenna.
σ_e^2 = Average power of the elements of $\mathbf{E} \sim \mathcal{CN}\left(0, \sigma_e^2\right)$.
σ_s^2 = Average power of the transmitted symbols on each layer.
ν = Number of spatial layers being employed. i.e., ν symbols are being transmitted.
$\mathbf{H}$ = Channel matrix $\in \mathbb{N}^{\mathrm{rx} \times N_{\mathrm{tx}}}$.
$\mathbf{W}$ = Precoding matrix $\in \mathbb{R}^{N_{\mathrm{tx}} \times \nu}$.
$\tilde{\mathbf{H}}$ = Effective channel matrix.
$\tilde{\mathbf{H}} = \mathbf{H}\mathbf{W} \in \mathbb{C}^{N_{\mathrm{rx}} \times \nu}$.

Denoting as $\mathbf{H}_0$ the channel between the transmitter and receiver and as $\mathbf{H}_i$ the channel for each of the I interferers, where $i = 1, 2, \ldots, I$, the receiver filter $\mathbf{G}_{\mathrm{ZF}}$ is expressed as

$$\mathbf{G}_{\mathrm{ZF}} = \left(\hat{\tilde{\mathbf{H}}}_0^{\mathrm{H}} \hat{\tilde{\mathbf{H}}}_0\right)^{-1} \hat{\tilde{\mathbf{H}}}_0^{\mathrm{H}} = \left(\left(\tilde{\mathbf{H}}_0 + \tilde{\mathbf{E}}\right)^{\mathrm{H}} \left(\tilde{\mathbf{H}}_0 + \tilde{\mathbf{E}}\right)\right)^{-1} \left(\tilde{\mathbf{H}}_0 + \tilde{\mathbf{E}}\right)^{\mathrm{H}}, \tag{C.6}$$

while the difference between the receive symbol vector $\hat{\mathbf{s}}_{\mathrm{ZF}} = \mathbf{G}_{\mathrm{ZF}} \left(\tilde{\mathbf{H}}_0 \mathbf{s}_0 + \mathbf{v} + \sum_{i=1}^{I} \tilde{\mathbf{H}}_i \mathbf{s}_i\right)$ and the transmitted symbol vector $\mathbf{s}$ is

$$\hat{\mathbf{s}}_{\mathrm{ZF}} - \mathbf{s} = \mathbf{G}_{\mathrm{ZF}} \left(-\mathbf{E}\mathbf{W}\mathbf{s}_0 + \mathbf{v} + \sum_{i=1}^{I} \tilde{\mathbf{H}}_i \mathbf{s}_i\right) \tag{C.7}$$

$$\begin{aligned} &= -\underbrace{\left(\left(\left(\mathbf{H}_0 + \mathbf{E}\right)\mathbf{W}\right)^{\mathrm{H}} \left(\mathbf{H}_0 + \mathbf{E}\right)\mathbf{W}\right)^{-1} \left(\left(\mathbf{H}_0 + \mathbf{E}\right)\mathbf{W}\right)^{\mathrm{H}} \mathbf{E}\mathbf{W}}_{\mathbf{D}} \mathbf{s}_0 \\ &\quad + \underbrace{\left(\left(\left(\mathbf{H}_0 + \mathbf{E}\right)\mathbf{W}\right)^{\mathrm{H}} \left(\mathbf{H}_0 + \mathbf{E}\right)\mathbf{W}\right)^{-1} \left(\left(\mathbf{H}_0 + \mathbf{E}\right)\mathbf{W}\right)^{\mathrm{H}}}_{\mathbf{N}} \mathbf{v} \\ &\quad + \sum_{i=0}^{I} \underbrace{\left(\left(\left(\mathbf{H}_0 + \mathbf{E}\right)\mathbf{W}\right)^{\mathrm{H}} \left(\mathbf{H}_0 + \mathbf{E}\right)\mathbf{W}\right)^{-1} \left(\left(\mathbf{H}_0 + \mathbf{E}\right)\mathbf{W}\right)^{\mathrm{H}} \tilde{\mathbf{H}}_i}_{\mathbf{I}_i = \mathbf{N}\tilde{\mathbf{H}}_i} \mathbf{s}_i, \end{aligned} \tag{C.8}$$

where we separate the expression into a signal part ($\mathbf{D}$), a noise part ($\mathbf{N}$), and an interference part ($\mathbf{I}_i$).

Applying a Taylor series expansion at $\mathbf{E} = 0$, we obtain

$$\begin{aligned}
\hat{\mathbf{s}}_{\mathrm{ZF}} - \mathbf{s} \approx -\Bigg[& \sum_{n_r,n_t} \frac{\partial \mathbf{D}}{\partial \Re\left\{[\mathbf{E}]_{n_r,n_t}\right\}}\bigg|_{\mathbf{E}=0} \Re\left\{[\mathbf{E}]_{n_r,n_t}\right\} \\
& + \sum_{n_r,n_t} \frac{\partial \mathbf{D}}{\partial \Im\left\{[\mathbf{E}]_{n_r,n_t}\right\}}\bigg|_{\mathbf{E}=0} \Im\left\{[\mathbf{E}]_{n_r,n_t}\right\} \Bigg] \mathbf{s}_0 \\
& + \Bigg[\left(\tilde{\mathbf{H}}_0^{\mathrm{H}}\tilde{\mathbf{H}}_0\right)^{-1}\tilde{\mathbf{H}}_0^{\mathrm{H}} + \sum_{n_r,n_t} \frac{\partial \mathbf{N}}{\partial \Re\left\{[\mathbf{E}]_{n_r,n_t}\right\}}\bigg|_{\mathbf{E}=0} \Re\left\{[\mathbf{E}]_{n_r,n_t}\right\} \\
& + \sum_{n_r,n_t} \frac{\partial \mathbf{N}}{\partial \Im\left\{[\mathbf{E}]_{n_r,n_t}\right\}}\bigg|_{\mathbf{E}=0} \Im\left\{[\mathbf{E}]_{n_r,n_t}\right\} \Bigg] \mathbf{v} \\
& + \sum_{i=0}^{I} \Bigg[\left(\tilde{\mathbf{H}}_0^{\mathrm{H}}\tilde{\mathbf{H}}_0\right)^{-1}\tilde{\mathbf{H}}_0^{\mathrm{H}}\tilde{\mathbf{H}}_i + \sum_{n_r,n_t} \frac{\partial \mathbf{I}_i}{\partial \Re\left\{[\mathbf{E}]_{n_r,n_t}\right\}}\bigg|_{\mathbf{E}=0} \Re\left\{[\mathbf{E}]_{n_r,n_t}\right\} \\
& + \sum_{n_r,n_t} \frac{\partial \mathbf{I}_i}{\partial \Im\left\{[\mathbf{E}]_{n_r,n_t}\right\}}\bigg|_{\mathbf{E}=0} \Im\left\{[\mathbf{E}]_{n_r,n_t}\right\} \Bigg] \mathbf{s}_i. \qquad \text{(C.9)}
\end{aligned}$$

Extending the aforementioned solutions for the Taylor expansion in [118, 119, 142, 143] to include interferers:

$$\begin{aligned}
\hat{\mathbf{s}}_{\mathrm{ZF}} - \mathbf{s} \approx & -\left(\tilde{\mathbf{H}}_0^{\mathrm{H}}\tilde{\mathbf{H}}_0\right)^{-1}\tilde{\mathbf{H}}_0^{\mathrm{H}}\tilde{\mathbf{E}}\mathbf{s}_0 + \left(\tilde{\mathbf{H}}_0^{\mathrm{H}}\tilde{\mathbf{H}}_0\right)^{-1}\left(\tilde{\mathbf{H}}_0^{\mathrm{H}} + \tilde{\mathbf{E}}^{\mathrm{H}}\right)\mathbf{v} \\
& - \left(\tilde{\mathbf{H}}_0^{\mathrm{H}}\tilde{\mathbf{H}}_0\right)^{-1}\left(\tilde{\mathbf{H}}_0^{\mathrm{H}}\tilde{\mathbf{E}} + \tilde{\mathbf{E}}^{\mathrm{H}}\tilde{\mathbf{H}}_0\right)\left(\tilde{\mathbf{H}}_0^{\mathrm{H}}\tilde{\mathbf{H}}_0\right)^{-1}\tilde{\mathbf{H}}_0^{\mathrm{H}}\mathbf{v} \\
& + \sum_{i=1}^{I}\Bigg[\left(\tilde{\mathbf{H}}_0^{\mathrm{H}}\tilde{\mathbf{H}}_0\right)^{-1}\left(\tilde{\mathbf{H}}_0^{\mathrm{H}} + \tilde{\mathbf{E}}^{\mathrm{H}}\right)\tilde{\mathbf{H}}_i\mathbf{s}_i \\
& - \left(\tilde{\mathbf{H}}_0^{\mathrm{H}}\tilde{\mathbf{H}}_0\right)^{-1}\left(\tilde{\mathbf{H}}_0^{\mathrm{H}}\tilde{\mathbf{E}} + \tilde{\mathbf{E}}^{\mathrm{H}}\tilde{\mathbf{H}}_0\right)\left(\tilde{\mathbf{H}}_0^{\mathrm{H}}\tilde{\mathbf{H}}_0\right)^{-1}\tilde{\mathbf{H}}_0^{\mathrm{H}}\tilde{\mathbf{H}}_i\mathbf{s}_i\Bigg], \qquad \text{(C.10)}
\end{aligned}$$

which expressed in shorter form,

$$\hat{\mathbf{s}}_{\mathrm{ZF}} - \mathbf{s} = -\tilde{\mathbf{H}}_0^{-1}\tilde{\mathbf{E}}\mathbf{s}_0 + \tilde{\mathbf{H}}_0^{-1}\mathbf{v} - \tilde{\mathbf{H}}_0^{-1}\tilde{\mathbf{E}}\tilde{\mathbf{H}}_0^{-1}\mathbf{v} + \sum_{i=1}^{I}\left[\tilde{\mathbf{H}}_0^{-1}\tilde{\mathbf{H}}_i\mathbf{s}_i - \tilde{\mathbf{H}}_0^{-1}\tilde{\mathbf{E}}\tilde{\mathbf{H}}_0^{-1}\tilde{\mathbf{H}}_i\mathbf{s}_i\right]. \qquad \text{(C.11)}$$

With the reasonable assumption that $\mathbf{s}_i$, $\mathbf{s}$, and $\mathbf{E}$ are statistically independent, the

MSE can be expressed as

$$\begin{aligned}\mathbf{MSE}_{\mathrm{ZF}} &= \mathbb{E}\Big\{(\tilde{\mathbf{s}}-\mathbf{s})(\tilde{\mathbf{s}}-\mathbf{s})^{\mathrm{H}}\Big\} \\ &\approx \tilde{\mathbf{H}}_0^{-1}\mathbb{E}\Big\{\tilde{\mathbf{E}}\mathbf{s}_0\mathbf{s}_0^{\mathrm{H}}\tilde{\mathbf{E}}^{\mathrm{H}}\Big\}\left(\tilde{\mathbf{H}}_0^{-1}\right)^{\mathrm{H}} \\ &\quad + \tilde{\mathbf{H}}_0^{-1}\mathbb{E}\{\mathbf{v}\mathbf{v}^{\mathrm{H}}\}\left(\tilde{\mathbf{H}}_0^{-1}\right)^{\mathrm{H}} + \tilde{\mathbf{H}}_0^{-1}\mathbb{E}\Big\{\tilde{\mathbf{E}}\tilde{\mathbf{H}}_0^{-1}\mathbf{v}\mathbf{v}^{\mathrm{H}}\left(\tilde{\mathbf{H}}_0^{-1}\right)^{\mathrm{H}}\tilde{\mathbf{E}}^{\mathrm{H}}\Big\}\left(\tilde{\mathbf{H}}_0^{-1}\right)^{\mathrm{H}} \\ &\quad + \sum_{i=0}^{I}\Bigg[\tilde{\mathbf{H}}_0^{-1}\mathbb{E}\Big\{\tilde{\mathbf{H}}_i\mathbf{s}_i\mathbf{s}_i^{\mathrm{H}}\tilde{\mathbf{H}}_i^{\mathrm{H}}\Big\}\left(\tilde{\mathbf{H}}_0^{-1}\right)^{\mathrm{H}} + \\ &\quad + \tilde{\mathbf{H}}_0^{-1}\mathbb{E}\Big\{\tilde{\mathbf{E}}\tilde{\mathbf{H}}_0^{-1}\tilde{\mathbf{H}}_i\mathbf{s}_i\mathbf{s}_i^{\mathrm{H}}\tilde{\mathbf{H}}_i^{\mathrm{H}}\left(\tilde{\mathbf{H}}_0^{-1}\right)^{\mathrm{H}}\tilde{\mathbf{E}}^{\mathrm{H}}\Big\}\left(\tilde{\mathbf{H}}_0^{-1}\right)^{\mathrm{H}}\Bigg] \end{aligned} \tag{C.12}$$

Applying

$$\mathbb{E}\{\mathbf{E}\mathbf{E}^{\mathrm{H}}\} = \sigma_e^2\,\mathrm{N_{tx}}\,\mathbf{I}_{\mathrm{N_{rx}}}, \tag{C.13}$$

and applying from [118]

$$\mathbb{E}\{\mathbf{E}\mathbf{A}\mathbf{E}^{\mathrm{H}}\} = \mathrm{Tr}\,(\mathbf{A})\,\sigma_e^2\,\mathbf{I}_{\mathrm{N_{rx}}}, \tag{C.14}$$

the MSE in Equation (C.11) can be expressed as

$$\begin{aligned}\mathbf{MSE}_{\mathrm{ZF}} &= \left(\sigma_e^2\sigma_{x_0}^2 + \sigma_v^2 + \sigma_v^2\sigma_e^2\mathrm{Tr}\left(\left(\mathbf{H}_0\mathbf{H}_0^{\mathrm{H}}\right)^{-1}\right)\right)\left(\tilde{\mathbf{H}}_0^{\mathrm{H}}\tilde{\mathbf{H}}_0\right)^{-1} \\ &\quad + \sum_{i=1}^{I}\left[\tilde{\mathbf{H}}_0^{-1}\left(\frac{\sigma_{x_i}^2}{\mathrm{N_{tx}}_i}\mathbf{H}_i\mathbf{H}_i^{\mathrm{H}} + \frac{\sigma_{x_i}^2}{\mathrm{N_{tx}}_i}\sigma_e^2\mathrm{Tr}\left(\mathbf{H}_i\mathbf{H}_i^{\mathrm{H}}\left(\mathbf{H}_0\mathbf{H}_0^{\mathrm{H}}\right)^{-1}\right)\left(\tilde{\mathbf{H}}_0^{-1}\right)^{\mathrm{H}}\right)\right],\end{aligned} \tag{C.15}$$

as shown in Section 4.2.

D. Evaluation of Multi-User Gain

Section 3.2.1.1 states that the reduction in simulation run time due to the application of a L2S model enables the analysis of more complex MU scenarios. One such scenario is the evaluation of the MU gain of different scheduling strategies to schedule the UEs in a cell [144]. Without an in-depth analysis such as in Chapter 5, this appendix presents such an example of MU performance evaluation.

Beginning with the SISO case, as an upper performance limit, the best CQI scheduler is employed, which assigns each RB to the UE with the highest reported channel quality. As a lower performance threshold, the round robin scheduler is employed. In round robin, each UE is assigned the same number of RBs, regardless of the reported channel conditions. Next to these, an implementation of proportional fair scheduling for OFDM [134] is compared. Results over UEs/cell are shown in Figure D.1.

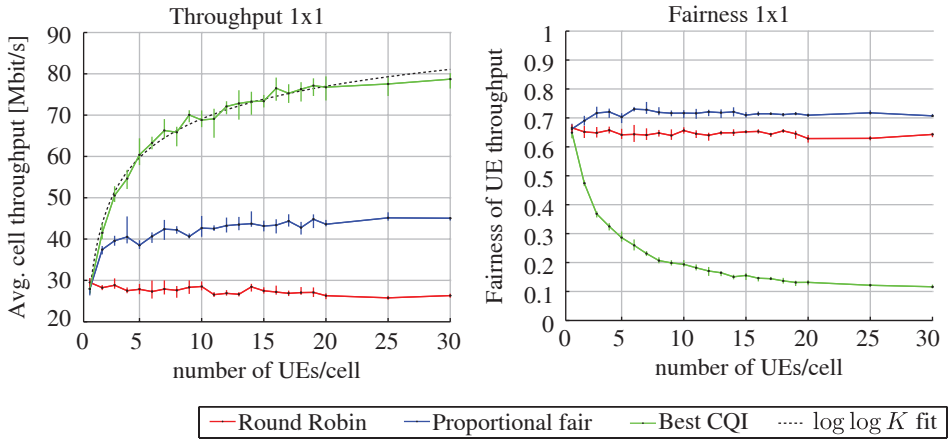

Figure D.1: 1×1 Single transmit antenna transmit mode multi-user gain. Left: throughput results. Right: fairness results. Vertical lines mark the 95% confidence intervals.

Similar to the analysis in [63], this simulation extends the MIMO scenario described in Table 5.1 (but without the addition of FFR). For these results, we compare the throughput results with a $\log\log$ fit. The reasoning for this fit is based on adapting the assumption that, for N_{TX} transmit antennas at the eNodeB and N_{RX} receive antennas at each of the K UEs, cell capacity grown with $N_{\mathrm{TX}} \log\log(K N_{\mathrm{RX}})$ [77, 145, 146] to this cellular scenario in which each UE does not experience the same SNR[1].

A metric $a \log\log(K\, b)$ is adopted to quantify the maximum achievable MU gain in this scenario for different antenna configurations. Denoting as $\log\log(K\, b_{1\times1})$ the MU gain for the 1×1 case and accordingly normalizing, 2×2 and 4×4 CLSM configurations, shown in Figures D.2 and D.3 are compared to the SISO case. We term a as the *multiplexing gain*, while b is denoted as the *multi-user gain flattening*, as it depicts the reduction in the capacity of the scheduler to correctly extract multi-user gain.

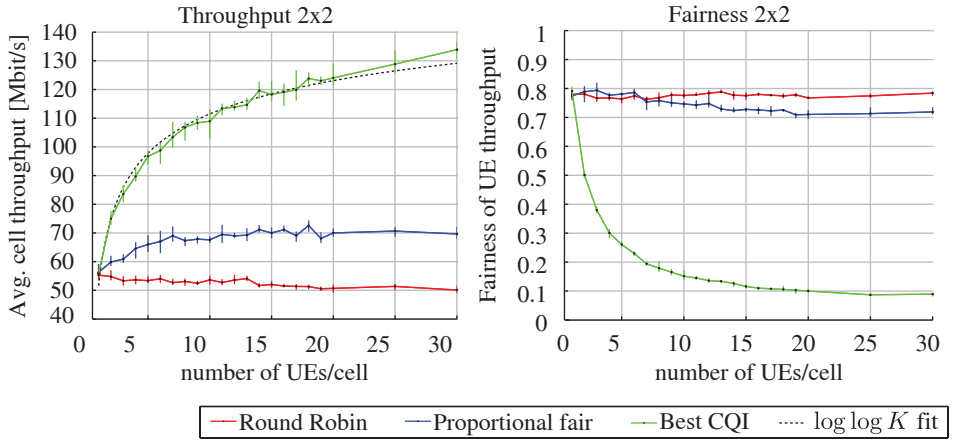

Figure D.2: 2×2 CLSM transmit mode multi-user gain results. Left: throughput results. Right: fairness results. Vertical lines mark the 95% confidence intervals.

The values obtained from a $\log\log$ MSE-minimizing fit are shown in Table D.1 for the SISO and 2×2 CLSM and 4×4 CLSM cases.

Table D.1.: $\log\log$ fit results for the 1×1, 2×2, and 4×4 antenna configurations.

	1×1	2×2 CLSM	4×4 CLSM
Multiplexing gain a	-	1.55	2.67
MU-gain flattening b	5.6	7.07	10.33

While the potential throughput of 4×4 is double that of 2×2, such gains are not

[1] The original expression is derived for MU-gain derived from the channel distribution, rather than that of the channel *and* the cell pathloss/layout.

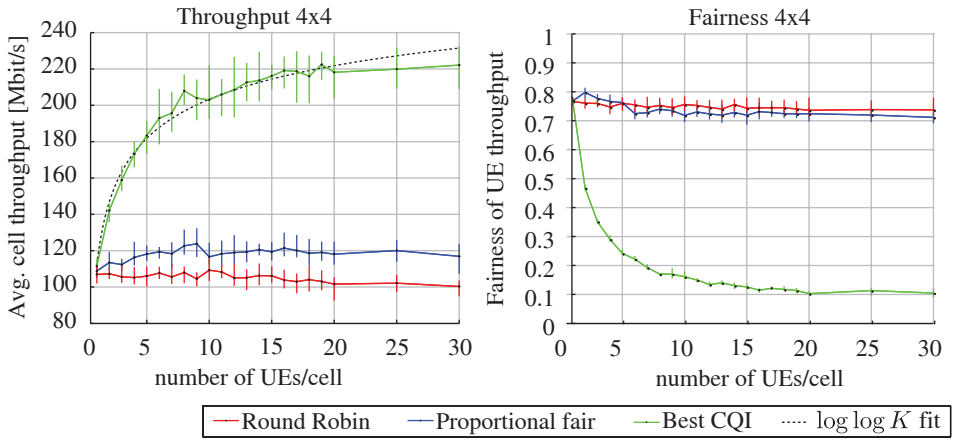

Figure D.3: 4×4 CLSM transmit mode multi-user gain results. Left: throughput results. Right: fairness results. Vertical lines mark the 95% confidence intervals.

achievable unless unrealistically high SNRs are present, even in the case of uncorrelated channels, as previously shown on Figure 3.17.

An analysis such as the one conducted here also quantifies the reduction in multi-user gain seen between the round robin and proportional fair schedulers when switching from a 2×2 to a 4×4 antenna configuration due to the higher suboptimality (due to the higher number of degrees of freedom), of the PMI and RI feedback in 4×4 MIMO.

The results of practically-employed schedulers, such as round robin and proportional fair can in this manner be compared to the upper threshold of the best CQI scheduler, which is not used due to it starving the majority of UEs in a cell.

Alternately, and similarly to the evaluation in Chapter 5, throughput and fairness (see Section 5.4) results can be evaluated together. As observed from Figures D.1 to D.3, proportional fair scheduling consistently converges to the same fairness value of roughly 0.7, with a decrease in multi-user gain for higher antenna counts, while the varying fairness results of round robin hint at it operating at different points of the fairness-throughput trade-off shown in Section 5.6.

Abbreviations and Acronyms

3GPP	3rd Generation Partnership Project
ACMI	Accumulated Mutual Information
AMC	Adaptive Modulation and Coding
ARQ	Automatic Repeat reQuest
AVI	Actual Value Interface
AWGN	Additive White Gaussian Noise
BICM	Bit-Interleaved Coded Modulation
BLER	Block Error Ratio
BSC	Base Station Controller
CA	Carrier Aggregation
CAPEX	CAPital EXpenditure
CB	Code Block
CC	Chase Combining
CDD	Cyclic Delay Diversity
cdf	Cumulative Density Function
CDMA	Code-Division Multiple Access
CLSM	Closed Loop Spatial Multiplexing
CP	Cyclic Prefix
C-Plane	Control Plane
CQI	Channel Quality Indicator

CRC	Cyclic Redundancy Check
CSI	Channel State Information
CoMP	Cooperative Multi-Point
DAS	Distributed Antenna Systems
DHCP	Dynamic Host Configuration Protocol
DL	Downlink
DLSCH	Downlink Shared Channel
ecdf	empirical cdf
ECR	Effective Code Rate
EDGE	Enhanced Data Rates for GSM Evolution
EESM	Exponential Effective SINR Mapping
eNodeB	Evolved Node B
EPC	Evolved Packet Core
ESM	Effective SINR Mapping
E-UTRAN	Evolved UMTS Terrestrial Radio Access Network
FDD	Frequency Division Duplex
FDMA	Frequency Division Multiple Access
FFR	Fractional Frequency Reuse
FFT	Fast Fourier Transform
FR	Full Reuse
GERAN	GSM EDGE Radio Access Network
GPRS	General Packet Radio Service
GSM	Global System for Mobile communications
HARQ	Hybrid Automatic Repeat reQuest
HSDPA	High-Speed Downlink Packet Access
HSPA	High-Speed Packet Access
HSS	Home Subscriber Server
IA	Interference Alignment
IR	Incremental Redundancy
IP	Internet Protocol
ISI	Inter-Symbol Interference

KPI	Key Performance Indicator
LLR	Log-Likelihood Ratio
L2S	Link-to-System
LTE	Long Term Evolution
M2M	Machine-to-Machine
MAC	Medium Access Control
MCL	Minimum Coupling Loss
MCS	Modulation and Coding Scheme
MI	Mutual Information
MIESM	Mutual Information Effective SINR Mapping
MIMO	Multiple-Input Multiple-Output
MME	Mobility Management Entity
MRC	Maximum Ratio Combining
MSE	Mean Square Error
MU	Multi-User
NAS	Non-Access Stratum
OFDM	Orthogonal Frequency-Division Multiplexing
OFDMA	Orthogonal Frequency-Division Multiple Access
OLSM	Open Loop Spatial Multiplexing
OPEX	OPerational EXpenditure
PCRF	Policy and Charging Rules Function
PDCP	Packet Data Convergence Protocol
pdf	probability density function
PDN	Packet Data Network
P-GW	PDN Gateway
PHY	Physical
PF	Proportional Fair
PMI	Precoding Matrix Indicator
PR	Partial Reuse
QAM	Quadrature Amplitude Modulation
QoS	Quality of Service

RAN	Radio Access Network
RB	Resource Block
RE	Resource Element
RI	Rank Indicator
RLC	Radio Link Control
RNC	Radio Network Controller
ROHC	RObust Header Compression
ROI	Region Of Interest
RRC	Radio Resource Control
RRM	Radio Resource Management
SAE	System Architecture Evolution
SC	SubCarrier
SC-FDMA	Single-carrier FDMA
SGSN	Serving-General packet radio service Support Node
S-GW	Serving Gateway
SIMO	Single-Input Multiple-Output
SINR	Signal to Interference and Noise Ratio
SISO	Single-Input Single-Output
SM	Spatial Multiplexing
SNR	Signal to Noise Ratio
STBC	Space-Time Block Code
SU	Single-User
SU-MIMO	Single User MIMO
SVD	Singular Value Decomposition
TB	Transport Block
TDD	Time Division Duplex
TTI	Transmission Time Interval
TxD	Transmit Diversity
UE	User Equipment
UL	Uplink
UMTS	Universal Mobile Telecommunications System

U-Plane	User Plane
UTRAN	UMTS Terrestrial Radio Access Network
W-CDMA	Wideband Code Division Multiple Access
ZF	Zero Forcing

Bibliography

[1] "**Cisco visual networking index: Global mobile data traffic forecast update, 2011-2016**," Cisco, Tech. Rep., 2012.

[2] "**Ericsson mobility report**," Ericsson, Tech. Rep., Nov. 2012.

[3] "**CTIA semi-annual wireless industry survey**," CTIA, Tech. Rep., 2012.

[4] "**The impact of latency on application performance**," Nokia Siemens networks, Tech. Rep., 2009.

[5] G. Foschini, "**Layered space-time architecture for wireless communication in a fading environment when using multi-element antennas**," *Bell labs technical journal*, vol. 1, no. 2, pp. 41–59, 1996.

[6] S. Weinstein and P. Ebert, "**Data transmission by frequency-division multiplexing using the discrete Fourier transform**," *IEEE Transactions on Communication Technology*, vol. 19, no. 5, pp. 628–634, 1971.

[7] Technical Specification Group Radio Access Network, "**Physical layer - general description**," 3GPP, Tech. Rep. TS 25.201, Dec. 2009.

[8] "**Vienna LTE link and system level simulator download site**."
http://www.nt.tuwien.ac.at/ltesimulator/

[9] A. Gurtov, M. Passoja, O. Aalto, and M. Raitola, "**Multi-layer protocol tracing in a GPRS network**," in *IEEE 56th Vehicular Technology Conference (VTC2002-Fall)*, Québec City, Canada, Sept. 2002.

[10] H. Holma and J. Reunanen, "**3GPP release 5 HSDPA measurements**," in *IEEE 17th International Symposium on Personal, Indoor and Mobile Radio Communications (PIMRC2006)*, Helsinki, Finland, Sept. 2006.

[11] S. Sesia, I. Toufik, and M. Baker, **LTE, The UMTS Long Term Evolution: From Theory to Practice**. John Wiley & Sons, Sept. 2011.

[12] Technical Specification Group Radio Access Network, "**E-UTRA; LTE physical layer – general description**," 3GPP, Tech. Rep. TS 36.201, Mar. 2009.

[13] H. Holma and A. Toskala, **WCDMA for UMTS: HSPA Evolution and LTE**. Wiley, Nov. 2007.

[14] Ericsson, "**Mobile broadband, busting the myth of the scissor effect**," White paper, Feb. 2010.

[15] Technical Specification Group Radio Access Network, "**Requirements for evolved UTRA (E-UTRA) and evolved UTRAN (E-UTRAN)**," 3rd Generation Partnership Project (3GPP), Tech. Rep. TR 25.913, Dec. 2009.

[16] H. Holma, A. Toskala, K. Ranta-Aho, and J. Pirskanen, "**High-speed packet access evolution in 3GPP release 7**," *IEEE Communications Magazine*, vol. 45, no. 12, pp. 29–35, 2007.

[17] J. C. Ikuno, **UMTS Long-Term Evolution**. in *Evaluation of HSDPA and LTE: From Testbed*

Measurements to System Level Performance, S. Caban, C. Mehlführer, M. Rupp, and M. Wrulich, Eds. John Wiley & Sons, Ltd, 2012.

[18] E. Dahlman, S. Parkvall, J. Skold, and P. Beming, **3G Evolution: HSDPA and LTE for Mobile Broadband**. Academic Press, July 2007.

[19] H. Yin and S. Alamouti, "**OFDMA: A broadband wireless access technology**," in *IEEE 2006 Sarnoff Symposium*, Mar. 2006.

[20] H. Myung, J. Lim, and D. Goodman, "**Single carrier FDMA for uplink wireless transmission**," *IEEE Vehicular Technology Magazine*, vol. 1, no. 3, pp. 30–38, 2006.

[21] E. Dahlman, H. Ekstrom, A. Furuskar, Y. Jading, J. Karlsson, M. Lundevall, and S. Parkvall, "**The 3G Long-Term Evolution - radio interface concepts and performance evaluation**," in *63rd IEEE Vehicular Technology Conference 2006 (VTC2006-Spring)*, Melbourne, Australia, May 2006.

[22] H. Ekstrom, A. Furuskar, J. Karlsson, M. Meyer, S. Parkvall, J. Torsner, and M. Wahlqvist, "**Technical solutions for the 3G Long-Term Evolution**," *IEEE Communications Magazine*, vol. 44, no. 3, pp. 38–45, Mar. 2006.

[23] M. Tanno, Y. Kishiyama, N. Miki, K. Higuchi, and M. Sawahashi, "**Evolved UTRA - physical layer overview**," in *IEEE 8th Workshop on Signal Processing Advances in Wireless Communications 2007 (SPAWC2007)*, Helsinki, Finland, June 2007.

[24] J. J. Sánchez, D. Morales-Jiménez, G. Gómez, and J. T. Enbrambasaguas, "**Physical layer performance of Long Term Evolution cellular technology**," in *16th Mobile and Wireless Communications Summit (IST2007)*, Budapest, Hungary, July 2007.

[25] D. Tse and P. Viswanath, **Fundamentals of Wireless Communication**. Cambridge University Press, June 2005.

[26] C. Mehlführer and M. Rupp, "**A robust MMSE equalizer for MIMO enhanced HSDPA**," in *Conference Record of the 40th Asilomar Conference on Signals, Systems and Computers (Asilomar2006)*, Pacific Grove, California, October 2006.

[27] T. Tang and R. Heath, "**Opportunistic feedback for downlink multiuser diversity**," *IEEE Communications Letters*, vol. 9, no. 10, pp. 948–950, Oct. 2005.

[28] A. Gyasi-Agyei, "**Multiuser diversity based opportunistic scheduling for wireless data networks**," *IEEE Communications Letters*, vol. 9, no. 7, pp. 670–672, July 2005.

[29] Technical Specification Group Radio Access Network, "**E-UTRA; user equipment (UE) radio access capabilities**," 3GPP, Tech. Rep. TS 36.306, Mar. 2010.

[30] Ericsson, "**SAE - the core network for LTE**," Apr. 2008.

[31] Technical Specification Group Services and System Aspects, "**General packet radio service (GPRS) enhancements for evolved universal terrestrial radio access network (E-UTRAN) access**," 3GPP, Tech. Rep. TS 23.401, Mar. 2010.

[32] Technical Specification Group Services and System Aspects, "**Architecture enhancements for non-3GPP accesses**," 3GPP, Tech. Rep. TS 23.402, Mar. 2010.

[33] Ericsson, "**LTE-an introduction. 284 23-3124 Uen Rev B**," White paper, June 2009.

[34] K. Sandlund, G. Pelletier, and L.-E. Jonsson, "**The RObust Header Compression (ROHC) framework**," Internet Engineering Task Force (IETF), Tech. Rep. RFC 5795, Mar. 2010.

[35] Technical Specification Group Radio Access Network, "**Evolved universal terrestrial radio access (E-UTRA) and evolved universal terrestrial radio access network (E-UTRAN); overall**

description; stage 2," 3GPP, Tech. Rep. TS 36.300, Mar. 2009.

[36] Technical Specification Group Core Network and Terminals, "**Non-access-stratum (NAS) protocol for evolved packet system (EPS)**," 3GPP, Tech. Rep. TS 23.301, Mar. 2012.

[37] P. Lescuyer and T. Lucidarme, **Evolved Packet System (EPS)**. John Wiley & Sons, Inc., 2008.

[38] S. Blake, D. Black, M. Carlson, E. Davies, Z. Wang, and W. Weiss, "**An architecture for differentiated service**," IETF, Tech. Rep. RFC 2475, Dec. 1998.

[39] Technical Specification Group Radio Access Network, "**E-UTRA; physical channels and modulation**," 3GPP, Tech. Rep. TS 36.211, May 2009.

[40] Technical Specification Group Radio Access Network, "**Evolved universal terrestrial radio access (E-UTRA); base station (BS) radio transmission and reception**," 3GPP, Tech. Rep. TS 36.104, Mar. 2009.

[41] S. Alamouti, "**A simple transmit diversity technique for wireless communications**," *IEEE Journal on Selected Areas in Communications*, vol. 16, no. 8, pp. 1451–1458, Oct. 1998.

[42] M. Bossert, A. Hübner, F. Schühlein, H. Haas, and E. Costa, "**On cyclic delay diversity in OFDM based transmission schemes**," in *7th International OFDM Workshop (InOWo2002)*, Hamburg, Germany, Aug. 2002.

[43] A. Dammann and S. Plass, "**Cyclic delay diversity: Effective channel properties and applications**," in *IEEE International Conference on Communications (ICC 2007)*, Glasgow, Scotland, 2007.

[44] E. Telatar, "**Capacity of multi-antenna gaussian channels**," *European Transactions on Telecommunications*, vol. 10, no. 6, pp. 585–595, 1999.

[45] Technical Specification Group Radio Access Network, "**E-UTRA; multiplexing and channel coding**," 3GPP, Tech. Rep. TS 36.212, Mar. 2009.

[46] J. C. Ikuno, S. Schwarz, and M. Šimko, "**LTE rate matching performance with code block balancing**," in *17th European Wireless Conference (EW2011)*, Vienna, Austria, Apr. 2011.

[47] C. Berrou, A. Glavieux, and P. Thitimajshima, "**Near shannon limit error-correcting coding and decoding: Turbo-codes**," in *IEEE International Conference on Communications (ICC93)*, Geneva, Switzerland, May 1993.

[48] Technical Specification Group Radio Access Network, "**Multiplexing and channel coding (FDD)**," 3GPP, Tech. Rep. TS 25.212, Mar. 2010.

[49] J. Hagenauer, "**Rate-compatible punctured convolutional codes (RCPC codes) and their applications**," *IEEE Transactions on Communications*, vol. 36, no. 4, pp. 389–400, Apr. 1988.

[50] I. Sohn and S. C. Bang, "**Performance studies of rate matching for WCDMA mobile receiver**," in *IEEE 52nd Vehicular Technology Conference (VTC 2000-Fall)*, Boston, Massachusetts, Sept. 2000.

[51] S. Schwarz, M. Wrulich, and M. Rupp, "**Mutual information based calculation of the precoding matrix indicator for 3GPP UMTS/LTE**," in *14th ITG Workshop on Smart Antennas (WSA2010)*, Bremen, Germany, Feb. 2010.

[52] D. Love and R. Heath, "**Limited feedback precoding for spatial multiplexing systems using linear receivers**," in *IEEE Military Communications Conference (MILCOM2003)*, Monterrey, California, Oct. 2003.

[53] Technical Specification Group Radio Access Network, "**E-UTRA; physical layer procedures**," 3GPP, Tech. Rep. TS 36.213, Mar. 2009.

[54] S. Schwarz, C. Mehlführer, and M. Rupp, "**Calculation of the spatial preprocessing and link adaption feedback for 3GPP UMTS/LTE**," in *IEEE 6th Conference on Wireless Advanced (WiAD2010)*, London, United Kingdom, June 2010.

[55] Technical Specification Group Radio Access Network, "**E-UTRA; medium access control (MAC) protocol specification**," 3GPP, Tech. Rep. TS 36.321, June 2010.

[56] R. Kwan, C. Leung, and J. Zhang, "**Multiuser scheduling on the downlink of an LTE cellular system**," *Research Letters in Communications*, vol. 2008, Jan. 2008.

[57] R. K. Jain, D.-M. W. Chiu, and W. R. Hawe, "**A Quantitative Measure Of Fairness And Discrimination For Resource Allocation In Shared Computer Systems**," Digital Equipment Corporation, Tech. Rep., Sept. 1984.

[58] P. Viswanath, D. Tse, and R. Laroia, "**Opportunistic beamforming using dumb antennas**," *IEEE Transactions on Information Theory*, vol. 48, no. 6, pp. 1277–1294, June 2002.

[59] S. Schwarz, C. Mehlführer, and M. Rupp, "**Low complexity approximate maximum throughput scheduling for LTE**," in *Conference Record of the 44th Asilomar Conference on Signals, Systems and Computers (Asilomar2010)*, Pacific Grove, California, Nov. 2010.

[60] C. Shuping, L. Huibinu, Z. Dong, and K. Asimakis, "**Generalized scheduler providing multimedia services over HSDPA**," in *IEEE International Conference on Multimedia and Expo (ICME2007)*, Beijing, China, July 2007.

[61] D. Skoutas, D. Komnakos, D. Vouyioukas, and A. Rouskas, "**Enhanced dedicated channel scheduling optimization in WCDMA**," in *14th European Wireless Conference (EW2008)*, Prague, Czech Republic, June 2008.

[62] M. Laner, P. Svoboda, and M. Rupp, "**Measurement aided model design for WCDMA link error statistics**," in *IEEE International Conference on Communications (ICC2011)*, Kyoto, Japan, June 2011.

[63] R. Pupala, L. Greenstein, and D. Daut, "**System-level impact of multi-user diversity in SISO and MIMO-based cellular systems**," *Journal of Communications*, vol. 6, no. 4, pp. 274–284, 2011.

[64] I. Medvedev, B. Bjerke, R. Walton, J. Ketchum, M. Wallace, and S. Howard, "**A comparison of MIMO receiver structures for 802.11n WLAN-performance and complexity**," in *IEEE 17th International Symposium on Personal, Indoor and Mobile Radio Communications (PIMRC2006)*, Sept. 2006.

[65] A. Paulraj, D. Gore, R. Nabar, and H. Bolcskei, "**An overview of MIMO communications-a key to gigabit wireless**," *Proceedings of the IEEE*, vol. 92, no. 2, pp. 198–218, Feb. 2004.

[66] D. Gesbert, M. Shafi, D. shan Shiu, P. Smith, and A. Naguib, "**From theory to practice: an overview of MIMO space-time coded wireless systems**," *IEEE Journal on Selected Areas in Communications*, vol. 21, no. 3, pp. 281–302, Apr. 2003.

[67] S. Schwarz, M. Simko, and M. Rupp, "**On performance bounds for MIMO OFDM based wireless communication systems**," in *IEEE Signal Processing Advances in Wireless Communications (SPAWC2011)*, San Francisco, California, June 2011.

[68] C. Mehlführer, J. C. Ikuno, M. Šimko, S. Schwarz, M. Wrulich, and M. Rupp, "**The Vienna LTE simulators - enabling reproducibility in wireless communications research**," *EURASIP Journal on Advances in Signal Processing*, vol. 2011, no. 1, pp. 1–14, 2011.

[69] Technical Specification Group Radio Access Network, "**E-UTRA; LTE RF system scenarios**," 3GPP, Tech. Rep. TR 36.942, Dec. 2008.

[70] R. Ghaffar and R. Knopp, "**Low complexity metrics for BICM SISO and MIMO systems**," in *IEEE 71st Vehicular Technology Conference (VTC2010-Spring)*, Taipei, Taiwan, May 2010.

[71] E. Zehavi, "**8-PSK trellis codes for a rayleigh channel**," *IEEE Transactions on Communications*, vol. 40, no. 5, pp. 873–884, 1992.

[72] G. Caire, G. Taricco, and E. Biglieri, "**Bit-interleaved coded modulation**," *IEEE Transactions on Information Theory*, vol. 44, no. 3, pp. 927–946, 1998.

[73] K. Brueninghaus, D. Astely, T. Salzer, S. Visuri, A. Alexiou, S. Karger, and G. Seraji, "**Link performance models for system level simulations of broadband radio access systems**," in *IEEE 16th International Symposium on Personal, Indoor and Mobile Radio Communications (PIMRC2005)*, Berlin, Germany, Sept. 2005.

[74] M. Wrulich, S. Eder, I. Viering, and M. Rupp, "**Efficient link-to-system level model for MIMO HSDPA**," in *20008 IEEE GLOBECOM Workshops*, New Orleans, Louisiana, 2008.

[75] C. Mehlführer, S. Caban, M. Wrulich, and M. Rupp, "**Joint throughput optimized CQI and precoding weight calculation for MIMO HSDPA**," in *42nd Asilomar Conference on Signals, Systems and Computers (Asilomar2008)*, Pacific Grove, California, 2008.

[76] Members of WINNER, "**Assessment of advanced beamforming and MIMO technologies**," WINNER, Tech. Rep. IST-2003-507581, 2005.

[77] R. Heath Jr, M. Airy, and A. Paulraj, "**Multiuser diversity for MIMO wireless systems with linear receivers**," in *35th Asilomar Conference on Signals, Systems and Computers (Asilomar2001)*, vol. 2, Pacific Grove, California, 2001.

[78] J. C. Ikuno, M. Wrulich, and M. Rupp, "**System level simulation of LTE networks**," in *71st Vehicular Technology Conference (VTC2010-Spring)*, Taipei, Taiwan, May 2010.

[79] L. Thiele, T. Wirth, K. Börner, M. Olbrich, V. Jungnickel, J. Rumold, and S. Fritze, "**Modeling of 3D field patterns of downtilted antennas and their impact on cellular systems**," in *13th ITG International ITG Workshop on Smart Antennas (WSA2009)*, Berlin, Germany, Feb. 2009.

[80] N. Jaldén, P. Zetterberg, B. Ottersten, A. Hong, and R. Thoma, "**Correlation properties of large scale fading based on indoor measurements**," in *IEEE Wireless Communications and Networking Conference, (WCNC2007)*, Hong Kong, China, Mar. 2007.

[81] Technical Specification Group Radio Access Network, "**RF system scenarios**," 3GPP, Tech. Rep. TR 25.942, Dec. 2008.

[82] Technical Specification Group Radio Access Network, "**Physical layer aspects for E-UTRA**," 3GPP, Tech. Rep. TR 25.814, 2006.

[83] Technical Specification Group Radio Access Network, "**E-UTRA; further advancements for E-UTRA physical layer aspects**," 3GPP, Tech. Rep. TR 36.814, Mar. 2010.

[84] M. Gudmundson, "**Correlation model for shadow fading in mobile radio systems**," *Electronics letters*, vol. 27, no. 23, pp. 2145–2146, 1991.

[85] D. Giancristofaro, "**Correlation model for shadow fading in mobile radio channels**," *Electronics Letters*, vol. 32, no. 11, pp. 958–959, 1996.

[86] R. Vijayan and J. Holtzman, "**The dynamic behavior of handoff algorithms**," in *1st International Conference on Universal Personal Communications (ICUPC1992)*, Dallas, Texas,

Sept. 1992.

[87] H. Claussen, "**Efficient modelling of channel maps with correlated shadow fading in mobile radio systems**," in *IEEE 16th International Symposium on Personal, Indoor and Mobile Radio Communications (PIMRC2005)*, Berlin, Germany, Sept. 2005.

[88] M. Moisio and A. Oborina, "**Comparison of effective SINR mapping with traditional AVI approach for modeling packet error rate in multi–state channel**," *Next Generation Teletraffic and Wired/Wireless Advanced Networking*, pp. 461–473, 2006.

[89] Y. Blankenship, P. Sartori, B. Classon, V. Desai, and K. Baum, "**Link error prediction methods for multicarrier systems**," in *IEEE 60th Vehicular Technology Conference (VTC2004-Fall)*, Los Angeles, California, Sept. 2004.

[90] L. Wan, S. Tsai, and M. Almgren, "**A fading-insensitive performance metric for a unified link quality model**," in *IEEE Wireless Communications and Networking Conference (WCNC 2006)*, Las Vegas, Nevada, Apr. 2006.

[91] E. Tuomaala and H. Wang, "**Effective SINR approach of link to system mapping in OFDM/multi-carrier mobile network**," in *2nd International Conference on Mobile Technology, Applications and Systems (MC07)*, Boston, Massachusetts, Nov. 2005.

[92] G. Caire, G. Taricco, and E. Biglieri, "**Capacity of bit-interleaved channels**," *Electronics Letters*, vol. 32, no. 12, pp. 1060–1061, 1996.

[93] G. Piro, L. Grieco, G. Boggia, F. Capozzi, and P. Camarda, "**Simulating LTE cellular systems: An open-source framework**," *IEEE Transactions on Vehicular Technology*, vol. 60, no. 2, pp. 498–513, 2011.

[94] G. Piro, N. Baldo, and M. Miozzo, "**An LTE module for the ns-3 network simulator**," in *4th International ICST Conference on Simulation Tools and Techniques (SIMUTools2011)*, 2011.

[95] D. Bültmann, M. Muehleisen, K. Klagges, and M. Schinnenburg, "**openwns - open wireless network simulator**," in *15th European Wireless Conference (EW2009)*, Aalborg, Denmark, May 2009.

[96] D. Rose, T. Jansen, and T. Kurner, "**Modeling of femto cells-simulation of interference and handovers in LTE networks**," in *IEEE 71st Vehicular Technology Conference (VTC2011-Spring)*, Budapest, Hungary, May 2011.

[97] Members of ITU, "**Recommendation ITU-R M.1225: Guidelines for evaluation of radio transmission technologies for IMT-2000**," International Telecommunication Union (ITU), Tech. Rep., Feb. 1997.

[98] C. Mehlführer, M. Wrulich, J. C. Ikuno, D. Bosanska, and M. Rupp, "**Simulating the Long Term Evolution physical layer**," in *European Signal Processing Conference (EUSIPCO2009)*, Glasgow, Scotland, Aug. 2009.

[99] P. Mogensen, W. Na, I. Kovács, F. Frederiksen, A. Pokhariyal, K. Pedersen, T. Kolding, K. Hugl, and M. Kuusela, "**LTE capacity compared to the Shannon bound**," in *IEEE 65th Vehicular Technology Conference (VTC2007-Spring)*, Dublin, Ireland, Apr. 2007.

[100] A. Golaup, M. Mustapha, and L. Patanapongpibul, "**Femtocell access control strategy in UMTS and LTE**," *IEEE Communications Magazine*, vol. 47, no. 9, pp. 117–123, 2009.

[101] H. Zhang, X. Wen, B. Wang, W. Zheng, and Y. Sun, "**A novel handover mechanism between femtocell and macrocell for LTE based networks**," in *Second International Conference on Communication Software and Networks (ICCSN2010)*, 2010.

[102] P. Kulkarni, W. Chin, and T. Farnham, "**Radio resource management considerations for LTE**

femto cells," *ACM SIGCOMM Computer Communication Review*, vol. 40, no. 1, pp. 26–30, 2010.

[103] V. Chandrasekhar, J. Andrews, and A. Gatherer, "**Femtocell networks: a survey**," *IEEE Communications Magazine*, vol. 46, no. 9, pp. 59–67, 2008.

[104] M. Taranetz, J. C. Ikuno, and M. Rupp, "**Sensitivity of OFDMA-Based macrocellular LTE networks to femtocell deployment density and isolation**," in *IEEE International Conference on Communications - Wireless Communications Symposium (ICC2013 WCS)*, Budapest, Hungary, June 2013.

[105] Ericsson, "**Outcome of adhoc discussion on refined simulation assumptions for calibration**," 3GPP TSG RAN WG1, Tech. Rep. R1-092270, May 2009.

[106] Ericsson, "**Email discussion summary on calibration step 1c**," 3GPP TSG RAN WG1, Tech. Rep. R1-092742, June 2009.

[107] K. Kusume, G. Dietl, T. Abe, H. Taoka, and S. Nagata, "**System level performance of downlink MU-MIMO transmission for 3GPP LTE-advanced**," in *IEEE 71st Vehicular Technology Conference (VTC2010-Spring)*, Taipei, Taiwan, May.

[108] D. Chase, "**Code combining–a maximum-likelihood decoding approach for combining an arbitrary number of noisy packets**," *IEEE Transactions on Communications*, vol. 33, no. 5, pp. 385–393, May 1985.

[109] J. C. Ikuno, C. Mehlführer, and M.Rupp, "**A novel LEP model for OFDM systems with HARQ**," in *IEEE International Conference on Communications (ICC2011)*, Kyoto, Japan, June 2011.

[110] J.-F. Cheng, "**On the coding gain of incremental redundancy over chase combining**," in *Global Telecommunications Conference (GLOBECOM2003)*, San Francisco, California, Dec. 2003.

[111] J.-F. Cheng, "**Coding performance of hybrid ARQ schemes**," *IEEE Transactions on Communications Communications*, vol. 54, no. 6, pp. 1017–1029, Mar. 2006.

[112] N. Prasad and M. K. Varanasi, "**Outage theorems for MIMO block fading channels**," *IEEE Transactions on Information Theory*, vol. 52, no. 12, pp. 5284–5296, 2006.

[113] P. Wu and N. Jindal, "**Performance of hybrid-ARQ in block-fading channels: A fixed outage probability analysis**," *IEEE Transactions on Communications*, vol. 58, no. 4, pp. 1129–1141, Apr. 2010.

[114] Y. R. Zheng and C. Xiao, "**Simulation models with correct statistical properties for rayleigh fading channels**," *IEEE Transactions on Communications*, vol. 51, no. 6, pp. 920–928, June 2003.

[115] T. Zemen and C. Mecklenbräuker, "**Time-variant channel estimation using discrete prolate spheroidal sequences**," *IEEE Transactions on Signal Processing*, vol. 53, no. 9, pp. 3597–3607, Sept. 2005.

[116] M. Šimko, C. Mehlführer, T. Zemen, and M. Rupp, "**Inter-Carrier Interference Estimation in MIMO OFDM Systems with Arbitrary Pilot Structure**," in *IEEE 73rd Vehicular Technology Conference (VTC2011-Spring)*, Budapest, Hungary, May 2011.

[117] J. C. Ikuno, S. Pendl, M. Simko, and M. Rupp, "**Accurate SINR estimation model for system level simulation of LTE networks**," in *IEEE International conference on Communications 2011 (ICC2012)*, Ottawa, Canada, June 2012.

[118] C. Wang, E. K. S. Au, R. D. Murch, W. H. Mow, R. S. Cheng, and V. K. N. Lau, "**On**

the performance of the MIMO zero-forcing receiver in the presence of channel estimation error," *IEEE Transactions on Wireless Communications*, vol. 6, no. 3, pp. 805–810, 2007.

[119] T. Weber, A. Sklavos, and M. Meurer, "**Imperfect channel-state information in MIMO transmission**," *IEEE Transactions on Communications*, vol. 54, no. 3, pp. 543–552, 2006.

[120] M. Šimko, S. Pendl, S. Schwarz, Q. Wang, J. C. Ikuno, and M. Rupp, "**Optimal pilot symbol power allocation in LTE**," in *IEEE 74th Vehicular Technology Conference (VTC2011-Fall)*, San Francisco, California, Sept. 2011.

[121] M. Simko, C. Mehlführer, T. Zemen, and M. Rupp, "**Inter-carrier interference estimation in MIMO OFDM systems with arbitrary pilot structure**," in *IEEE 73rd Vehicular Technology Conference (VTC2011-Spring)*, Budapest, Hungary, May 2011.

[122] L. Hentilä, P. Kyösti, M. Käske, M. Narandzic, and M. Alatossava, "**MATLAB implementation of the WINNER phase II channel model ver1.1**," Dec. 2007.
http://www.ist-winner.org/phase_2_model.html

[123] G. Boudreau, J. Panicker, N. Guo, R. Chang, N. Wang, and S. Vrzic, "**Interference coordination and cancellation for 4G networks**," *IEEE Communications Magazine*, vol. 47, no. 4, pp. 74–81, Apr. 2009.

[124] T. Novlan, J. Andrews, I. Sohn, R. Ganti, and A. Ghosh, "**Comparison of fractional frequency reuse approaches in the OFDMA cellular downlink**," in *Proceedings of the 2010 IEEE Global Telecommunications Conference (GLOBECOM2010)*, Baltimore, Maryland, Dec. 2010.

[125] M. Assaad, "**Optimal fractional frequency reuse (FFR) in multicellular OFDMA system**," in *IEEE 68th Vehicular Technology Conference (VTC2008-Fall)*, Calgary, Canada, Sept. 2008.

[126] M. Rahman and H. Yanikomeroglu, "**Enhancing cell-edge performance: a downlink dynamic interference avoidance scheme with inter-cell coordination**," *IEEE Transactions of Wireless Communications*, vol. 9, no. 4, pp. 1414–1425, Apr. 2010.

[127] A. Najjar, N. Hamdi, and A. Bouallegue, "**Efficient frequency reuse scheme for multi-cell OFDMA systems**," in *IEEE Symposium on Computers and Communications (ISCC2009)*, Sousse, Tunisia, July 2009.

[128] V. Jungnickel, M. Schellmann, L. Thiele, T. Wirth, T. Haustein, O. Koch, W. Zirwas, and E. Schulz, "**Interference-aware scheduling in the multiuser MIMO-OFDM downlink**," *IEEE Communications Magazine*, vol. 47, no. 6, pp. 56–66, June 2009.

[129] Z. Xie and B. Walke, "**Frequency reuse techniques for attaining both coverage and high spectral efficiency in ofdma cellular systems**," in *IEEE Wireless Communications and Networking Conference (WCNC2010)*, Sydney, Australia, Apr. 2010.

[130] A. Simonsson, "**Frequency reuse and intercell interference co-ordination in E-UTRA**," in *IEEE 65th Vehicular Technology Conference (VTC2007-Spring)*, Dublin, Ireland, Apr. 2007.

[131] L. Chen and D. Yuan, "**Generalized frequency reuse schemes for OFDMA networks: Optimization and comparison**," in *IEEE 71st Vehicular Technology Conference (VTC2010-Spring)*, Taipei, Taiwan, May 2010.

[132] B. Krasniqi, M. Wrulich, and C. Mecklenbräuker, "**Network-load dependent partial frequency reuse for lte**," in *9th International Symposium on Communications and Information Technology (ISCIT2009)*, Incheon, Korea, Sept. 2009.

[133] M. Taranetz and J. C. Ikuno, "**Capacity density optimization by fractional frequency partitioning**," in *45th Annual Asilomar Conference on Signals, Systems, and Computers (ASILOMAR2011)*, Pacific Grove, California, Nov. 2011.

[134] Z. Sun, C. Yin, and G. Yue, "**Reduced-complexity proportional fair scheduling for OFDMA systems**," in *2006 International Conference on Communications, Circuits and Systems (ICCCAS2006)*, Guilin, China, June 2006.

[135] J. C. Ikuno, M. Taranetz, and M. Rupp, "**A fairness-based performance evaluation of fractional frequency reuse in LTE**," in *17th International ITG Workshop on Smart Antennas (WSA2013)*, Stuttgart, Germany, Mar. 2013.

[136] A. Jalali, R. Padovani, and R. Pankaj, "**Data throughput of CDMA-HDR a high efficiency-high data rate personal communication wireless system**," in *IEEE 51st Vehicular Technology (VTC2000-Spring*, Tokyo, Japan, 2000.

[137] S. Schwarz, C. Mehlführer, and M. Rupp, "**Throughput maximizing multiuser scheduling with adjustable fairness**," in *IEEE International Conference on Communications (ICC2011)*, Kyoto, Japan, June 2011.

[138] M. Taranetz and M. Rupp, "**Performance of femtocell access point deployments in user hotspot scenarios**," in *Australasian Telecommunication Networks and Applications Conference (ATNAC2012)*, Nov. 2012.

[139] F. Richter, A. Fehske, and G. Fettweis, "**Energy efficiency aspects of base station deployment strategies for cellular networks**," in *IEEE 70th Vehicular Technology Conference Fall (VTC2009-Fall)*, Anchorage, Alaska, Sept. 2009.

[140] L. Correia, D. Zeller, O. Blume, D. Ferling, Y. Jading, I. Godor, G. Auer, and L. Van Der Perre, "**Challenges and enabling technologies for energy aware mobile radio networks**," *IEEE Communications Magazine*, vol. 48, no. 11, pp. 66–72, 2010.

[141] Technical Specification Group Radio Access Network, "**E-UTRA; carrier aggregation; base station (BS) radio transmission and reception**," 3GPP, Tech. Rep. TR 36.808, July 2012.

[142] T. Weber, A. Sklavos, and M. Meurer, "**Channel knowledge: A crucial prerequisite for MIMO transmission?**" in *COST 273 TD(03)083, Paris, France*, May 2003.

[143] X. Jin, H. Jiang, J. Hu, Y. Yuan, C. Zhao, and J. Shi, "**Maximum data rate power allocation for MIMO spatial multiplexing systems with imperfect CSI**," in *IEEE 69rd Vehicular Technology Conference (VTC2009-Spring)*, Apr. 2009.

[144] S. Schwarz, J. Colom Ikuno, M. Šimko, M. Taranetz, Q. Wang, and M. Rupp, "**Pushing the Limits of LTE: A Survey on Research Enhancing the Standard**," *arXiv e-prints*, Dec. 2012.

[145] M. Sharif and B. Hassibi, "**A comparison of time-sharing, DPC, and beamforming for MIMO broadcast channels with many users**," *Communications, IEEE Transactions on*, vol. 55, no. 1, pp. 11–15, 2007.

[146] M. Kountouris, "**The cardinal role of scheduling in downlink multiuser MIMO systems**," May 2007.